LUND UNIVERSITY

Engineered Nanoparticles Generation, Characterization and Applications

Messing, Maria

2011

Engineered Nanoparticles

Generation, Characterization,

and Applications

Doctoral Thesis

Maria Messing

Principal Supervisor:
Prof. Knut Deppert

Faculty Opponent:
Prof. Einar Kruis
University of Duisburg-Essen

LUND UNIVERSITY

Division of Solid State Physics
Department of Physics
Lund, Sweden 2011

för min familj

Abstract

It is predicted that novel nanometer-sized structures incorporating nanoparticles will have a considerable impact on our lives during the coming decades. Engineered nanoparticles are already found in a number of commercially available products. However, many applications of these nanoparticles have only reached the stage of promising ideas or research demonstrations. The number of nanoparticle-based products on the market is therefore expected to increase considerably during the coming decades.

For engineered nanoparticles to be useful in different commercial applications, it is important that their generation can be controlled. This means a stable generation process resulting in reproducible, high-quality nanoparticles with properties tailored for specific applications. In order to develop such production methods, thorough characterization of the particles generated is essential. In addition, since the impact of nanoparticles on human health and the environment has not been fully explored, the entire lifecycle of engineered nanoparticles must be thoroughly investigated. Engineered nanoparticles should not cause any harm to human health or the environment, during manufacturing or use of the product, or during disposal of the product after use.

This thesis describes the manufacture of engineered nanoparticles, mainly by inert gas evaporation using a spark discharge generator and an evaporation/condensation furnace. Considerable effort has been put into investigating how different generation parameters affect particle production, so that the particle properties can be controlled and tailored to meet specific applications. To achieve this, the as-generated nanoparticles have been systematically characterized by various methods; transmission electron microscopy being the key characterization tool. The nanoparticles generated were then used in three different areas of application: as seed particles for so-called nanowires which may be useful in future devices, as model catalyst systems to provide deeper knowledge about the atomic-scale mechanisms involved in catalysis, and finally for research in the area of nano safety to learn how nanoparticles should be handled in a safe and sustainable manner.

Preface

My nanotechnology adventures began in the fall of 2003, when I embarked on the Master of Science in Engineering Nanoscience program at Lund University. On the very first day, the director of the program, Professor Knut Deppert, gave us a welcome talk that I still remember. He told us that the aim of the program was to prepare us for nanotechnology-related research, and that it was his hope that the majority of us would go on to a PhD after completing the program. Most of us laughed a little at this since few of us had envisaged a future in academic research.

After 3½ years' of study, it was time for me to do my Master's thesis project, and Knut invited me to do my project with him at the Division of Solid State Physics. He had bought a new nanoparticle generator that needed to be adapted and integrated into the existing nanoparticle production setup. Six months later I came out of the lab with my Master's thesis and a deepened interest in nanoparticles. My Master's project had raised new questions, providing a number of ideas for future projects, so undertaking a PhD was the obvious way to go, as was my choice of supervisor.

I have worked on the generation, characterization and application of a number of different types of nanoparticles during my entire PhD that started in the fall of 2007. The applications of the engineered nanoparticles have varied over time. During the first and second years of my studies, my research focused mainly on investigating the effect of seed particles on nanowire growth. Gold was the main particle material used, but other metals were also studied. During spring 2008 I started collaborating with Dr. Rasmus Westerström at the Division of Synchrotron Radiation Research (Lund University), who introduced me to the world of catalysis and surface science. Our "two-man" project has since evolved, and now involves several other researchers, many interesting measurement techniques and a few side projects. The additional benefit of my collaboration with surface physicists is that I was finally lucky enough to be introduced to the 3S Conferences!

My first, brief encounter with the area of nano safety was during the fall of 2008 in Munich, when I was collaborating with the group of Dr. Wolfgang Kreyling, studying rodent inhalation of titanium dioxide particles. My second project in nano safety, which started during the summer of 2009, was in collaboration with Dr. Annele Virtanen and Matti Happonen from Tampere University, where we investigated diesel soot particles. Before continuing my work on nano safety at Lund University I performed more investigations on nanowire growth. I had the opportunity to spend the first three months of 2010 at the Australian National University in Canberra, working with Professor Chennupati Jagadish's group. This time we worked on nanowire heterostructures. Upon my return to Lund, in the summer of 2010, I started to work on a large nano safety project involving several divisions within the university. The aim of this project was to gain a better understanding of nanoparticle toxicology.

List of Papers

The following papers are included in this thesis, and are referred to in the text by their Roman numerals.

I.
Generation of size-selected gold nanoparticles by spark discharge – for growth of epitaxial nanowires
M. E. Messing, K. A. Dick, L. R. Wallenberg and K. Deppert
Gold Bulletin, **2009**, 42(1), 20–26

I planned, organized and led the project, performed the experimental work and analyzed the data. I wrote the paper.

II.
Generation of nanoparticle aerosols by spark discharge
B. O. Meuller, M. E. Messing, D. L. J. Engberg, A. Jansson, L. I. M. Johansson, S. M. Norlén, N. Turesson and K. Deppert
Manuscript intended for submission to *Aerosol Science and Technology* **2011**

I participated in literature reviews, discussions and writing of the paper.

III.
Controlled polytypic and twin-plane superlattices in III/V nanowires
P. Caroff, K. A. Dick, J. Johansson, M. E. Messing, K. Deppert and L. Samuelson
Nature Nanotechnology, **2009**, 4(1), 50–55

I participated in the experimental work, the analysis of the data and in writing the paper.

IV.
Growth of straight InAs-on-GaAs nanowire heterostructures
M. E. Messing, J. Wong-Leung, Z. Zanolli, H. J. Joyce, H. H. Tan, Q. Gao, L. R. Wallenberg, J. Johansson and C. Jagadish
Nano Letters, **2011**, in press

I organized and led the project, performed the experimental work and analyzed the data. I wrote the paper.

V.
The use of gold for fabrication of nanowire structures
M. E. Messing, K. Hillerich, J. Johansson, K. Deppert and K. A. Dick
Gold Bulletin, **2009**, 42(3), 172–181

I planned, organized and led the project. I performed the literature review and the analysis, and I wrote the paper.

VI.
A comparative study of the effect of gold seed particle preparation method on nanowire growth
M. E. Messing, K. Hillerich, J. Bolinsson, K. Storm, J. Johansson, K. A. Dick and K. Deppert
Nano Research, **2010**, 3(7), 506–519

I planned, organized and led the project together with two of the co-authors. I played a major role in performing the experiments and analyzing the data, and I wrote the paper.

VII.
Generation of Pd model catalyst nanoparticles by spark discharge
M. E. Messing, R. Westerström, B. O. Meuller, S. Blomberg, J. Gustafson, J. N. Andersen, E. Lundgren, R. van Rijn, O. Balmes, H. Bluhm and K. Deppert
Journal of Physical Chemistry C, **2010**, 114(20), 9257–9263

I planned, organized and led the project together with the co-authors. I performed most of the experiments and analyzed most of the data. I wrote the paper.

VIII.
The oxidation and reduction of Pd(100) and aerosol deposited Pd nanoparticles
R. Westerström, **M. E. Messing**, S. Blomberg, A. Hellman, H. Grönbeck,
J. Gustafson, N. M. Martin, O. Balmes, R. van Rijn, J. N. Andersen, K. Deppert,
H. Bluhm, Z. Liu, M. E. Grass, M. Hävecker and E. Lundgren
Physical Review B, **2011**, 83(11), 115440

I participated in organizing the project, in performing most of the experimental work and analyzing most of the data, and in writing the paper.

IX.
Generation and characterization of stable, highly concentrated titanium dioxide nanoparticle aerosols for rodent inhalation studies
W. G. Kreyling, P. Biswas, **M. E. Messing**, N. Gibson, M. Geiser, A. Wenk,
M. Sahu, K. Deppert, I. Cydzik, C. Wigge, O. Schmid and M. Semmler-Behnke
Journal of Nanoparticle Research, **2011**, 13(2), 511–524

I participated in particle sampling, in performing the measurements and analyzing the results of the TEM experiments, and in writing the paper.

X.
The comparison of particle oxidation and surface structure of diesel soot particles between fossil fuel and novel renewable diesel fuel
M Happonen, T. Lahde, **M. E. Messing**, T. Sarjovaara, M. Larmi,
L. R. Wallenberg, A. Virtanen and J. Keskinen
Fuel, **2010**, 89(12), 4008–4013

I planned and performed the TEM analysis of the soot particles, and participated in the writing of the paper.

XI.
Gas-borne particles for nanotoxicology studies
M. E. Messing, C. R. Svensson, B. O. Meuller, K. Deppert, J. Pagels and J. Rissler
Manuscript submitted to *Nanotoxicology* **2011**

I took part in planning and organizing the project and played an important role in performing the experiments and analyzing the results. I wrote the paper.

Papers not included in this thesis

I contributed to the following papers which are not included due to overlapping content or content beyond the scope of this thesis. They are listed in chronological order.

xii.

InSb heterostructure nanowires: MOVPE growth under extreme lattice mismatch
P. Caroff, **M. E. Messing**, B. M. Borg, K. A. Dick, K. Deppert and
L. –E. Wernersson
Nanotechnology, **2009**, 20(49), 495606

xiii.

Control of III-V nanowire structure by growth parameter tuning
K. A. Dick, P. Caroff, J. Bolinsson, **M. E. Messing**, J. Johansson, K. Deppert,
L. R. Wallenberg and L. Samuelson
Semiconductor Science and Technology, **2010**, 25(2), 024009

xiv.

Diameter dependence of the wurtzite–zinc blende transition in InAs nanowires
J. Johansson, K. A. Dick, P. Caroff, **M. E. Messing**, J. Bolinsson, K. Deppert and
L. Samuelson
Journal of Physical Chemistry C, **2010**, 114(9), 3837–3842

xv.

Analysis of strain and stacking faults in single nanowires using Bragg coherent diffraction imaging
V. Favre-Nicolin, F. Mastropietro, J. Eymery, D. Camacho, Y. M. Niquet,
B. M. Borg, **M. E. Messing**, L. –E. Wernersson, R. E. Algra, E. P. A. M. Bakkers,
T. H. Metzger, R. Harder and I. K. Robinson
New Journal of Physics, **2010**, 12(3), 035013

xvi.

Epitaxial InP nanowire growth from Cu seed particles
K Hillerich, **M. E. Messing**, L. R. Wallenberg, K. Deppert and K. A. Dick
Journal of Crystal Growth, **2011**, 315(1), 134–137

xvii.

Synthesis and magnetic characterization of MnAs nanoparticles via nano-particle conversion
M. F. H. Wolff, D. Görlitz, K. Nielsch, **M. E. Messing** and K. Deppert
Nanotechnology, **2011**, 22(5), 055602

xviii.

Fabrication and characterization of AlP-GaP core-shell nanowires
M. T. Borgström, K. Mergenthaler **M. E. Messing**, U. Håkanson, J. Wallentin, L. Samuelson and M. –E. Pistol
Journal of Crystal Growth, **2011**, 324(1), 290–295

xix.

Parameter space mapping of InAs nanowire crystal structure
K. A. Dick, J. Bolinsson, **M. E. Messing**, S. Lehmann, J. Johansson and P. Caroff
Journal of Vacuum Science and Technology B, **2011**, 29(4), 04D103

xx.

Growth of doped InAs$_y$P$_{1-y}$ nanowires with InP shells
J. Wallentin, **M. E. Messing**, E. Trygg, L. Samuelson, K. Deppert and M. T. Borgström
Journal of Crystal Growth, **2011**, 31(1), 8–14

xxi.

A new route towards semiconductor nanospintronics: highly Mn-doped GaAs nanowires realized by ion-implantation under dynamic annealing conditions
C. Borschel, **M. E. Messing**, M. T. Borgström, W. Paschoal, J. Wallentin, S. Kumar, K. Mergenthaler, K. Deppert, C. M. Canali, H. Pettersson, L. Samuelson and C. Ronning
Nano Letters, **2011**, in press

List of abbreviations

1D	one-dimensional
ALI	air–liquid interface
APM	aerosol particle mass analyzer/analysis
bcc	body-centered cubic
CCD	charge-coupled device
CPC	condensation particle counter
CTF	contrast transfer function
DDC	directly deposited colloid particles
DMA	differential mobility analyzer
dme	differential mobility diameter
DP	diffraction pattern
e/c	evaporation/condensation
EBD	electron beam lithography-defined particles
EBL	electron beam lithography
ECA	evaporation/condensation-generated aerosol particles
EELS	electron energy-loss spectrometer/spectrometry
EFTEM	energy-filtered transmission electron microscope/microscopy
EN590	conventional fossil diesel fuel
ESC	electrosprayed colloid particles
ESP	electrostatic precipitator
fcc	face-centered cubic
FEG	field-emission gun
FET	field effect transistor
GIF	Gatan image filter
HPXPS	high-pressure X-ray photoelectron spectroscopy

HRTEM	high-resolution transmission electron microscope/microscopy
HT	high-temperature
HVO	hydrotreated vegetable oils
IA	idealized aggregate
LED	light-emitting diode
MBE	molecular beam epitaxy
MFC	mass flow controller
MOVPE	metal organic vapor phase epitaxy
PLL	poly-L-lysine
sc	simple cubic
SDA	spark discharge generated aerosol particles
SDG	spark discharge generator/generated
SEM	scanning electron microscope/microscopy
-SH	thiol
STEM	scanning transmission electron microscope/microscopy
SXRD	surface X-ray diffraction
TEM	transmission electron microscope/microscopy
TFA	particles generated by annealing of thin films
UHV	ultra-high vacuum
VPE	vapor phase epitaxy
VLM	visible light microscope/microscopy
VLS	vapor liquid solid
VPE	vapor phase epitaxy
VSS	vapor solid solid
WZ	wurtzite
XEDS	X-ray energy dispersive spectrometer/spectrometry
XPS	X-ray photoelectron spectroscopy
XRD	X-ray diffraction
ZB	zinc-blende

Acknowledgements

There are many reasons why I often smile when I go to work. All the advanced (and expensive) equipment I have access to is one reason, but the most important reason is because of all the people working there. I would like to thank all my inspiring, talented and motivated colleagues for creating such a great working place.

First, I would like to thank my main supervisor Professor Knut Deppert to whom I am extremely grateful. Thank you for convincing me to do a PhD and for sending me all around the world to meet, interact and collaborate with talented researchers from a number of different organizations. You have taught me so much, inspired me to work hard, always taken time to listen to my crazy ideas, and made these years so very enjoyable. I could not have wished for a better supervisor.

I have also been lucky enough to have three outstanding assistant supervisors: Dr. Kimberly Thelander, Professor Reine Wallenberg, and Dr. Jonas Johansson.

Kimberly, thank you for making me feel really welcome at the Division, for always taking the time to share your enormous knowledge about nanowire growth with me, for helping me improve my article writing, and for a huge amount of inspiration. Thank you also for being such a good friend and travel partner – our trip to the Iguaçu Falls was so much fun.

Reine, thank you for taking the time to teach me most of what I know about electron microscopy and how to use the TEM, which is definitely my favorite instrument. We have spent many hours by the TEM filled with laughter and hard work and I appreciate very much the way how you always encourage me to improve my microscopy skills. I also appreciate very much that it is not too hard to convince you that an hour or so of bike driving in the sun is sometimes more important than a few additional high-resolution images.

Jonas, thank you for equally patiently trying to explain nanowire growth theory to me. I am very grateful that you always took the time to discuss problems and to help me when I needed some good ideas and input for new projects.

Among the people I have had the privilege to work and interact with, there are some who have had slightly more impact on my time as a PhD student, than others.

My great friend and favorite colleague, Karla Hillerich, thank you for many successful projects in which I was lucky enough to work with you. I also enjoyed our conference trips, our late lunches, our discussions about nanowire (as well as other) problems, our dinner parties, your delicious cupcakes, and the fact that I can always talk to you about anything.

Bengt Meuller, what would I have done without you? Thank you for always solving my problems with the aerosol system, and for being patient with me when I bothered you with technical problems requiring immediate solution. In addition, I appreciated having another aerosol researcher at the Division to perform interesting nanoparticle projects with. Finally, I value you greatly as a close friend.

In addition to my official supervisors, I have also had a few unofficial supervisors, the most important one being Dr. Philippe Caroff. Thank you for giving me the opportunity to participate in exciting projects and for always taking time to discuss science as well as life in general with me. Your enthusiasm for research is enormously inspiring, and you were the first person to enthuse me sufficiently to go to the TEM at 6-o-clock in the morning with a smile on my face.

Dr. Bernhard Mandl, thank you for giving me the opportunity to work with you in fascinating "particle-free" projects, and for being my good friend. I will never forget how welcome you made me feel and how much you helped me when I was new at the Division. I miss having you around and I miss your lessons in "indispensable" Austrian expressions.

Christian Svensson, I am very happy that you decided to become a PhD student as I really enjoyed working with you on our collaborative projects within the field of nano safety. Thank you for many pleasant hours in the lab, and our amusing discussions.

I am very grateful to Dr. Rasmus Westerström for introducing me to, and expertly teaching me about, the world of catalysis and surface science. It was great working with you, and I miss you now that you are away doing your post-doc.

Contents

Chapter 1

Introduction

The field of nanotechnology, in which matter is studied and manipulated on the atomic or molecular level, is currently attracting enormous attention. Nanotechnology already has, and will continue to have, considerable impact on our life as well as on the global economy [1], but questions are being raised about potential health risks and the possible environmental impact of this complex technology [2]. The main reason for the fascination in nanometer-sized structures is their interesting properties, which are not found in the bulk material. Surface effects and quantum mechanical effects arise in nanostructures due to their large surface-to-volume ratio and the fact that their dimensions are of the same order as the electron wavelength, respectively. Such effects are utilized to produce new improved materials, as well as novel medical, optical and electronic devices. A typical nanostructure already in use in a number of consumer products, is the nanoparticle. In the work presented in this thesis, the generation of nanoparticles has been thoroughly investigated with the aim of realizing fully controlled production of engineered nanoparticles with tailored properties. The engineered nanoparticles were then used for different applications: as seed particles for nanowire growth, as model catalyst particles, and for research in the field of nano safety. The generation of nanoparticles is discussed in Chapter 2, their characterization in Chapter 3, and the different applications in Chapter 4, 5, and 6 respectively.

1.1 Nanoparticles

All human beings are exposed to nanoparticles in their everyday life. Nanoparticles are generated by several mechanisms including nature itself (in forests, oceans, and deserts), and arise from anthropogenic sources such as combustion engines, car tires, coal fires, cooking and construction. It is well known that nanoparticles can have a major impact on climate [3] and public health [4]. Nanoparticles in the atmosphere affect the climate both by direct scattering of short-wave incoming solar radiation and by influencing cloud formation [5]. Although nanoparticles may have a positive effect on climate, due to their effects on cloud formation, which is believed to reduce global warming nanoparticles in the air have severe negative effects on human health. It has been demonstrated that long-term exposure to airborne nanoparticles is an important risk factor in mortality due to cardiopulmonary disease and lung cancer [6].

The word nanoparticle is used to describe particles with diameters ranging from 1 to more than 1000 nm. Throughout this thesis the term nanoparticles is used to describe particles with diameters roughly between 1 and 200 nm. In addition to their size, the shape of nanoparticles can also vary significantly. Some nanoparticles are spherical, or almost spherical, some have a hexagonal shape, and others exhibit a less compact, chain-like structure. Furthermore, the internal structure of nanoparticles, often meaning the way in which their atoms are distributed, may also vary. Some are amorphous (randomly distributed atoms) while others are crystalline (regularly distributed atoms). Crystalline materials may be polycrystalline, which means that the structure (particle) contains different areas with different single-crystalline orientations.

A specific group of nanoparticles is categorized as aerosol particles, and the majority of the particles discussed in this thesis belong to this group. The precise definition of an aerosol is a solid or liquid particle suspended in a gas [7], thus the term aerosol refers to both the particle and the gas. It should be noted, however, that this expression is often used for the particle only. According to this definition, almost all nanoparticles could be considered to be aerosol particles, but in this thesis only particles suspended in a specific carrier gas, such as nitrogen, during generation will be termed aerosol particles.

1.2 Engineered Nanoparticles

Nanoparticles can be generated by human activity both unintentionally, e.g. in combustion engine exhaust, or intentionally, i.e. engineered to meet specific demands. A large number of useful applications based on engineered nanoparticles already exist today [8]. In the field of optoelectronics, nanoparticle-based light-emitting diodes (LEDs) [9] and gas sensors [10, 11] have been demonstrated. Another, well-known, application of nanoparticles is in sunscreens [12], but nanoparticles are also found in cosmetics [13], in paints [14], and even in new types of fabric [15]. It was also recently discovered that frescoes could be restored with the help of nanoparticles [16]. Furthermore, nanoparticles are used in the food industry, typically in packaging material [15, 17], but also in refrigerators where food is stored [15]. In the field of medicine and biology, several nanoparticle applications have already been approved for clinical use, and many others are at different stages of development. Nanoparticle-based biomedical applications include drug delivery, tissue engineering, fluorescent biological labeling, and MRI contrast enhancement, among others [18, 19].

The engineered nanoparticles described in this thesis have mainly been used for three distinct applications. The first is the production of so-called nanowires, which are rod-like with high potential as building blocks for electronic, optoelectronic and sensor applications. In this case the nanoparticles act as seeds to initiate the (epitaxial) growth of semiconductor nanowires. The second application is in catalysis research. Typical catalysts consist of small nanoparticles dispersed on an oxide support, but the mechanisms governing catalysts are not fully understood. It is hoped that a better understanding of the atomic-scale processes involved in catalysis can be achieved by using small nanoparticles as catalyst model systems. The final application of engineered nanoparticles in this work is in the area of nano safety. Since nanoparticles are found in a large number of products and applications, it is of the utmost importance that the possible risks be evaluated, so that nanoparticles can be manufactured, handled, and used safely.

Different nanoparticle applications require the manufacture of different kinds of nanoparticles. Nanoparticles synthesized from organic polymers are often used for biomedical applications, such as drug delivery, whereas semiconducting nanoparticles are used for optoelectronic applications. The nanoparticles produced during combustion, for example in car engines, are organic soot particles. However, soot particles are also commercially produced to obtain a substance known as

carbon black. Metal oxide nanoparticles are found in paints, cosmetics, and sunscreens, while metal nanoparticles have a broad range of applications. Silver is typically used for its antibacterial properties, gold both for its inert and catalytic properties, and other transition metals such as palladium, platinum, and rhodium, for their catalytic properties. For the applications described in this thesis, engineered nanoparticles were produced from a number of different materials. The nanoparticles used as seeds for semiconductor nanowires were mainly gold particles, palladium particles were used as model catalysts, while gold, titanium dioxide (TiO_2), and soot particles were used for nano safety research.

Several techniques can be used to engineer nanoparticles from different materials. These are usually divided into chemical processing, mechanical milling or physical processing. In chemical processing, chemical precursors and solvents in liquid or gas form are used to form nanoparticles. These methods often require expensive chemicals, and can result in partly contaminated particles, and significant amounts of chemical waste. Mechanical milling involves grinding a large piece of material into small particles. A very high energy input is required to produce small nanoparticles with this method, and it is difficult to manufacture particles with uniform size and shape. Nanoparticle production by physical processes comprises sputtering and evaporation in an inert gas. Although nanoparticle generation by physical processes may be complicated and a fairly high energy input is sometimes required, it has some advantages over the other techniques, such as the avoidance of chemical waste, good control of particle size, and the generation of highly pure particles. The majority of the nanoparticles described in this thesis were manufactured by inert gas evaporation. The method most commonly used was evaporation by means of spark discharge, but thermal evaporation was also used to a lesser extent.

Chapter 2

Nanoparticle Generation

Nanoparticles generated and deposited with different methods exhibit differences in the controllability of, for example, particle size, position on the substrate, surface density, morphology, crystal structure, and purity. A certain type of particle could be advantageous in one regard, but less useful from another point of view, and it is, therefore, not always obvious which type of particle or deposition method should be used. Throughout this thesis, "particle type" is used to indicate nanoparticles generated and deposited with a specific method. Certain generation and deposition methods can be more or less suitable depending on the required particle material. Throughout this thesis considerable effort has been put into investigating how different generation parameters affect particle production, so that the particle properties can be controlled and tailored to meet specific applications.

Aerosol-generated particles were used for the catalysis and nano safety applications. Aerosol-generated particles and chemically manufactured colloid particles were the main choice for nanowire seed particles. However, other particle types, including electron beam lithography- (EBL) defined particles and particles generated by annealing of thin films, were also used as seed particles to investigate the effect of nanoparticle generation and deposition method on nanowire growth.

2.1 Aerosol-Generated Nanoparticles

A common method for the production of aerosol particles is evaporation of a material in an inert gas. This can be done in several ways, such as laser ablation in which a laser is used to evaporate the material, spark discharge, or thermal evaporation in a furnace. The two different aerosol particle production methods

used in the present work were spark discharge generation (SDG) and thermal evaporation, referred to as the evaporation/condensation (e/c) method. Gold particles were produced by both methods, whereas palladium and titanium dioxide particles were generated exclusively by spark discharge.

2.1.1 Spark Discharge

A commercially available aerosol generator (GFG 1000, Palas, Karlsruhe, Germany) primarily constructed for carbon soot particle production was used to produce nanoparticles by spark discharge. The mechanism is based on the discharge between two conducting cylindrical electrodes positioned in the middle of a polymer (or ceramic) chamber with the electrode ends separated by a distance of about 2 mm (Figure 2.1). The distance between the electrodes is automatically kept during particle production to maintain a constant breakdown voltage. A capacitor connected to one of the electrodes is charged by a high-voltage supply with adjustable output current [20], and when the breakdown voltage of 2 kV is reached the capacitor discharges instantaneously forming a spark across the electrode gap. The local temperature of the spark is high [21], resulting in evaporation of electrode material. Primary particles are formed by homogeneous nucleation of this supersaturated vapor, and coalesce into larger particles. In the original setup a stream of argon gas and/or air flowing between the electrodes is used to transport the as-produced primary particles towards the aerosol outlet about 15 mm downstream of the electrodes. Further growth of primary particles by condensation and coagulation results in the production of highly charged, nanometer-sized agglomerate particles [22]. For the production of nanoparticles in this work the argon/air carrier gas was replaced by ultra-pure nitrogen gas in all cases except in the generation of TiO_2 particles. Furthermore, the graphite electrodes used in the original setup were replaced by high-purity metal (gold, palladium, or titanium) rods (99.99%) with diameters of 3 mm, mounted on cylindrical stainless steel holders with diameters of 6 mm.

Two parameters can be adjusted to optimize particle production, namely the spark discharge frequency and the carrier gas flow rate. The spark discharge frequency, f, is determined by the charging current, I, of the capacitor which has a capacitance, C, and the discharge voltage, V_d, [22] by:

$$f = \frac{I}{CV_d} \qquad\qquad (2.1)$$
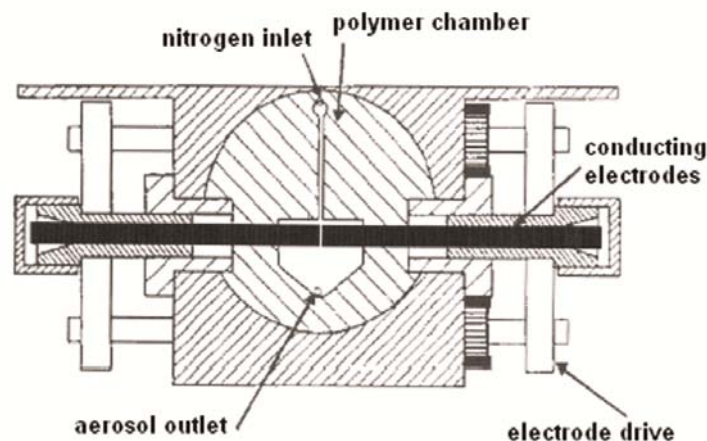
Figure 2.1 Schematic of the aerosol spark generator used to produce nanoparticles by spark discharge between two conducting electrodes [20].

It should be noted that the discharge voltage is not exactly equal to the breakdown voltage, V_b, but slightly higher since some time is required for the discharge conditions to develop [23]. An additional overvoltage, V_O, is therefore introduced to balance the discharge and breakdown voltages: $V_d = V_b + V_O$. The spark discharge frequency can be varied between 0 and 300 Hz, which corresponds to an increase in charging current from 0.13 to 20 mA [24]. Increasing the spark discharge frequency results in an increase in the particle number concentration and a shift towards larger particle diameters [Paper I], which is in good agreement with other reports on particles produced by spark discharge [Paper II, 20, 23, 25]. Figure 2.2 shows the relation between the increase in particle number concentration, from 3×10^5 cm^{-3} to 1.3×10^6 cm^{-3}, and particle diameter, from approximately 10 to 30 nm, for gold particles with an increase in spark discharge frequency from 30 to 300 Hz. The higher the spark discharge frequency, the greater the increase in the number of particles produced per second, since more electrode material is evaporated per second. The increase in evaporated particle material also leads to a higher coagulation rate, and hence faster growth of the particles, resulting in particles with larger diameters.

The carrier flow rate can be adjusted between 2 and 8 l/min in order to obtain a reproducible and constant rate of particle generation. The flow rate must be high enough to remove all primary particles and ions between the electrodes before the next spark. Increasing the carrier flow rate from 3.4 to 5.9 l/min resulted in a slight decrease in gold particle number concentration, but had no effect on gold particle diameter. However, specific carrier flow rates combined with specific spark discharge frequencies resulted in more stable particle production.
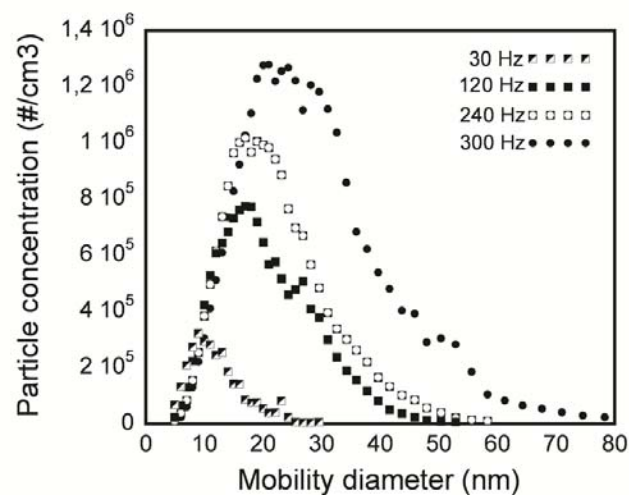
Figure 2.2 Size distribution of agglomerated gold particles generated with a nitrogen gas flow rate of 5.9 l/min while varying the spark discharge frequency from 30 to 300 Hz (measured with a differential mobility analyzer).

The highest yield of gold particles obtained under stable conditions was observed when combining a carrier flow rate of 5.9 l/min with a spark discharge frequency of 300 Hz [Paper I], and these parameters were used for the production of SDG nanowire seed particles throughout this work. The most stable conditions for palladium particles were found to be a carrier flow rate of 3.4 l/min, used in combination with different spark discharge frequencies depending on the desired size of the palladium particles. It should be noted that using a gas other than nitrogen affects the stability and size distribution of the particles [23], and the optimum parameters for stable particle production will probably differ from the settings where the original argon gas and graphite electrodes are used.

2.1.2 Evaporation/Condensation

The evaporation/condensation method is also based on evaporation from a solid piece of material, but in this case by thermal evaporation, using a high-temperature (HT) furnace. The evaporated material is transported away from the bulk material by a flow of ultra-pure carrier gas (nitrogen), and primary particles formed by homogeneous nucleation, grow by coagulation into agglomerated particles. The size distribution of the particles can be shifted to larger diameters and higher particle concentrations can be obtained by increasing the temperature of the furnace [26]. During this work temperatures between 1575 and 1950°C were used for the production of gold particles.

2.1.3 The Aerosol Nanoparticle Generation Setup

Regardless of the method of generation, the agglomerated nanoparticles should preferably be reshaped into compact particles if they are to be used for applications such as nanowire seed particles or catalyst model particles. Monodisperse nanowires of a known diameter are often required, which in turn require monodisperse seed particles of a known diameter [27]. To achieve this, the spark generator or high-temperature furnace was connected to an aerosol nanoparticle generation setup [Paper I, 28]. The entire setup, which enables size distribution measurements, reshaping of the agglomerate particles, and controlled particle deposition, is illustrated in Figure 2.3. The agglomerate particles are first passed through a neutralizer in order to achieve a reproducible and known charge distribution of primarily uncharged and singly-charged particles by collision with ions from a β-emitting ^{63}Ni source [29]. Once the stable charge distribution is achieved, the charged particles are size-selected in a differential mobility analyzer (DMA), labeled DMA 1 in Figure 2.3. The DMA is a standard instrument in aerosol science, used to classify charged particles according to their mobility in an electric field [30]. If the particles are singly charged, their mobility can be related to the particle mobility diameter, d_m, which for spherical particles is equal to the geometrical particle diameter. An agglomerated particle can be transformed into a compact, spherical-like particle by heating inside a compaction tube furnace (Route 1 in Figure 2.3). The mobility diameter may thus decrease substantially due to the reduced drag force (increased mobility) of spherical particles compared to that of agglomerates, although the mass of the particles remains the same. If the particles are not reshaped, size distribution measurements can be performed directly on the agglomerated particles using an electrometer, provided that each particle passing through the DMA carries one single charge (Route 2 in Figure 2.3). A second DMA (DMA 2 in Figure 2.3) is used to obtain size distributions of the reshaped particles. Size distributions are obtained by scanning the voltage of the DMA and measuring the resulting particle concentration with the electrometer. To determine the appropriate compaction temperature for the agglomerated particles the reshaping temperature is scanned and the peak value of the size distributions is determined at each temperature [31]. The final part of the aerosol nanoparticle generation setup includes an electrostatic precipitator (ESP) for controlled continuous deposition of particles onto a substrate. The ESP focuses the charged particles onto a collector electrode [32], on which the substrate is placed, allowing high-efficiency deposition of particles with diameters up to about 150 nm.
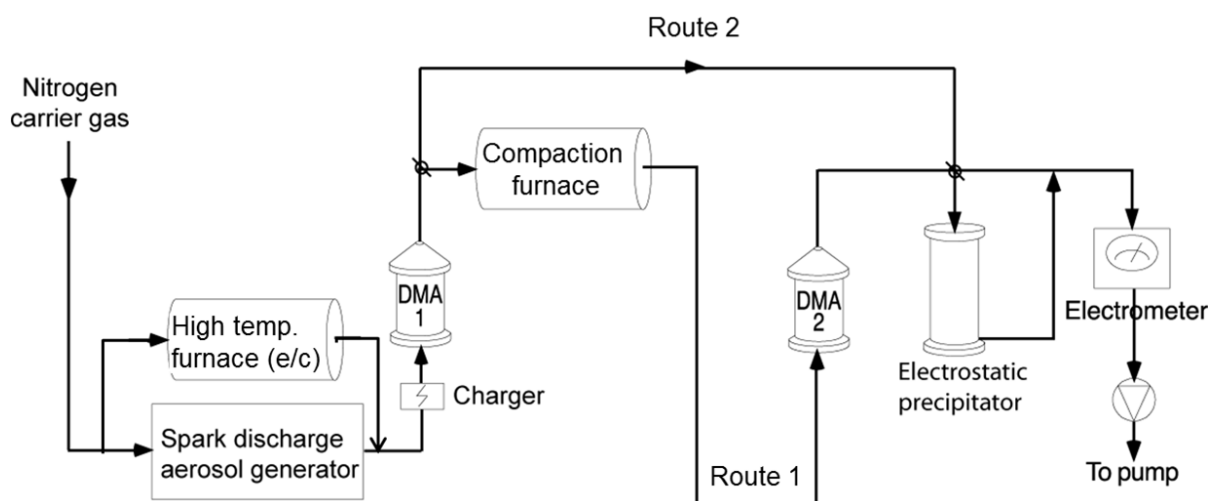
Figure 2.3 Schematic of the aerosol nanoparticle generation setup in which nanoparticles are generated, reshaped, size-selected, and deposited on a substrate.

Both SDG- and e/c-generated gold particles are fully compacted below 300°C, and thus no further compaction of the particles occurs [Paper I, 28]. For palladium particles, a slightly higher reshaping temperature was needed, as will be further discussed below. However, although no further shrinkage of the particles occurs above this compaction temperature the reshaping continues at higher temperatures due to internal rearrangement of the particle structure. With increasing temperature the particles become more spherical and transform from polycrystalline into mono-crystalline. Figure 2.4 shows the change in particle structure with increasing reshaping temperature for SDG gold particles, starting with the collection of primary particles that constitute the non-reshaped agglomerated particles (Figure 2.4a). After reshaping at 600°C (Figure 2.4c) the particles exhibit a reasonably spherical structure, which is very similar for both SDG- and e/c-generated gold particles. The highest yield of particles with the required seed particle structure was obtained at this temperature, and 600°C was therefore used for the production of all aerosol-generated nanowire gold seed particles described in this thesis. The particles were more spherical at 1200°C (Figure 2.4d), but the yield was lower.

Aerosol-generated particles have some advantages and some disadvantages compared to the other nanoparticle generation methods used to produce nanowire seed particles. The disadvantages of aerosol-generated particles include the more complicated and expensive setup, the waste of particle material (especially due to low charging efficiency and size selection), and the somewhat limited size distribution of the particles. The compacted SDG-generated gold particles are limited to a maximum diameter of around 35 nm, while the upper limit for e/c

generated particles is around 100 nm, due, in both cases, to limitations of the setup used. However, the main disadvantage associated with aerosol-generated gold particles, as for most particle types, is the random positioning of particles on the substrate. The advantages of aerosol-generated particles are that extremely pure particles with a tunable, monodisperse diameter can be produced and deposited with a well-controlled surface density at a reasonable throughput. Moreover, the aerosol deposition method offers greater substrate flexibility. Particles can be deposited onto more or less any type of substrate with diameters up to several centimeters.
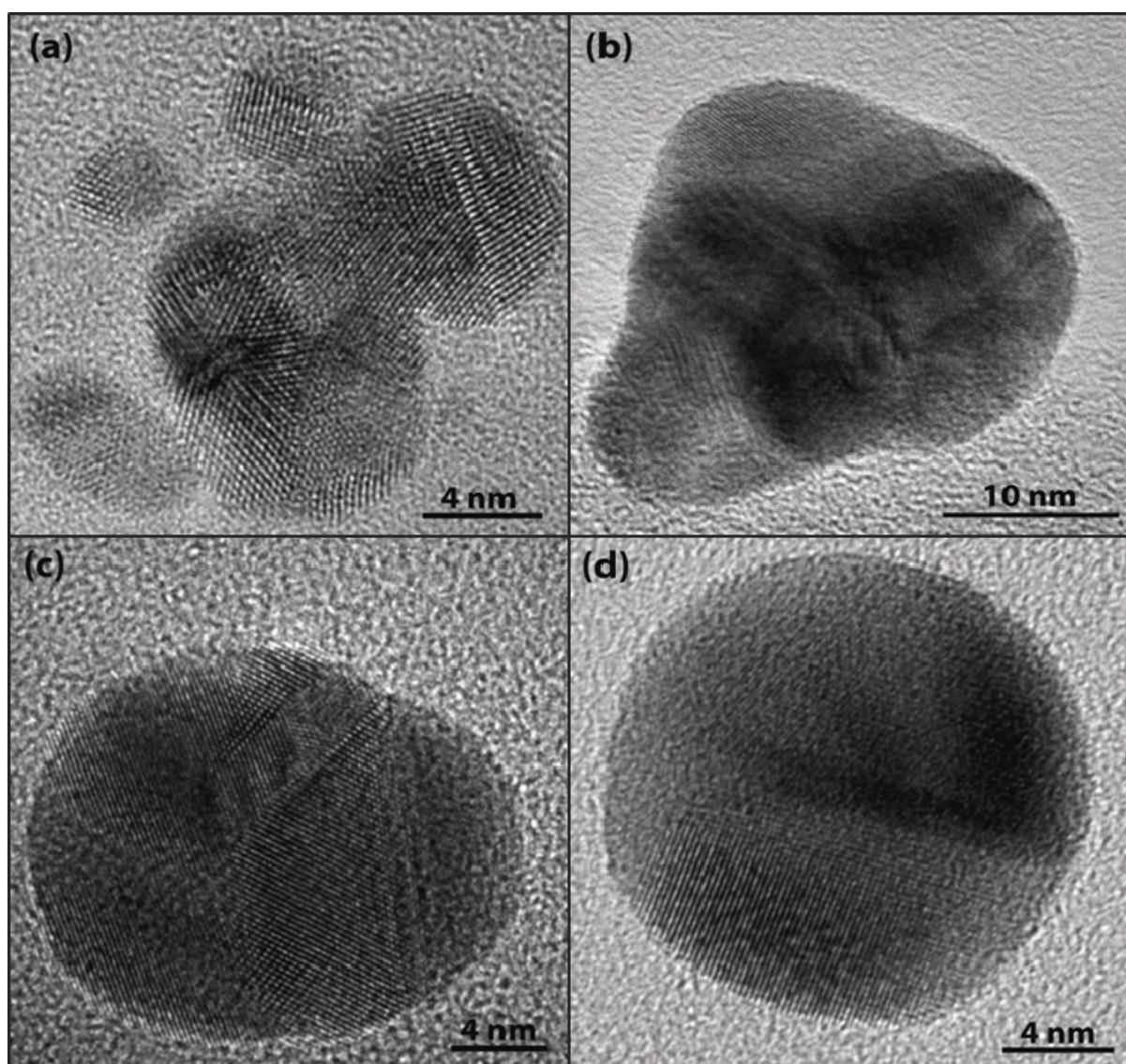
Figure 2.4 TEM micrographs of **(a)** an SDG-generated agglomerated gold particle and SDG-generated gold particles reshaped in a compaction tube furnace at **(b)** 300°C, **(c)** 600°C, and **(d)** 1200°C.

2.2 Other Methods of Nanoparticle Generation

In addition to aerosol generation, a few other methods are commonly used to produce and deposit seed particles for nanowire growth. Colloidal particles, electron beam lithography (EBL) defined particles, and particles generated by annealing of thin films are often used to seed nanowire growth. Gold is by far the most widely used seed particle material and, although particles of many different materials can be produced with these methods, only gold particles were produced with these methods in this work.

2.2.1 Colloidal Nanoparticles

Colloidal nanoparticles are synthesized by chemical reactions. In the case of gold particles, chloroauric acid ($HAuCl_4$) is reduced by citric acid ($C_6H_8O_7$) or trisodium citrate ($Na_3C_6H_5O_7$) in an aqueous solution [33]. Normally, ligands such as sodium citrate ($C_6H_5Na_3O_7$), phosphines (PH_3) or thiols (-SH) are attached to the particles in order to keep them suspended in the solution and prevent them from agglomerating [34]. Gold colloid particles are commercially available in a wide range of diameters with a diameter dispersion of less than 10%. All colloidal particles used as nanowire seed particles in this work were commercially produced (British Biocell International, Cardiff, UK).

Two different methods were used to deposit colloid particles: the direct deposition method and the electrospray method. In the direct deposition method, a droplet of colloidal solution is placed on a substrate. Rotation of the substrate, typically between 500 and 3000 rpm, allows excess liquid to be removed, providing a more even surface distribution of the particles. The surface density of the particles can be controlled to some extent by varying the concentration of the colloid solution. One problem may arise with direct deposition of colloids onto a substrate when both the colloid solution and the substrate surface are negatively charged. To solve this problem an intermediate layer of the surfactant poly-L-lysine (PLL), containing a positively charged end, can be used. This method is often used to ensure adhesion of the particles to the substrate by electrostatic interactions [35].

A commercially available electrospray generator was used for electrospray deposition (model 3480, TSI, Shoreview, USA). The colloid solution is drawn through a capillary in a very high electric field, and is atomized at the tip of the capillary due to electrohydrodynamic breakup, resulting in small, highly charged droplets

carrying approximately one particle each [36]. Directly after formation, the droplets are neutralized by a radioactive α-emitter ^{210}Po leading to mainly singly and doubly charged droplets. Following neutralization, an ultra-pure carrier gas (nitrogen) is used to dry the particles, by evaporation of the liquid, and transport them to an ESP (model 3089, TSI) for deposition. The deposition process is similar to that of aerosol-generated particles, and hence no PLL is required for the particles to adhere to the substrate.

The main advantage of colloid particles is the availability of particles of a variety of different diameters with a narrow size distribution. Some of the other advantages and disadvantages of colloid particles differ slightly depending on the deposition method used. Direct deposition often results in inhomogeneous particle surface coverage, and it is difficult to produce samples with precisely controlled particle densities, although it is a fairly rapid method. Moreover, if mechanical rotation of the samples is required, the samples must not be too thin/fragile, too small, or too large. These disadvantages can be overcome by using the electrospray method, in which samples with a homogeneous distribution of a given particle surface density are generated. In addition, when using electrospray deposition, particles can be deposited onto more or less any type of substrate with diameters up to a few centimeters. Such a setup is, however, rather expensive and more difficult to use than the direct deposition method. Furthermore, regardless of the deposition method used, it is generally not possible to control the position of colloid particles on the substrate. The major problem associated with both methods is that of contamination. Organic remnants from the synthesis and stabilization processes, as well as PLL if the direct deposition method is used, contaminate the particle and substrate surfaces.

2.2.2 Production of Nanoparticles by Annealing of Thin Films

The procedure most commonly used for the generation of nanoparticles from thin films is thermal evaporation of a metal film directly onto the substrate. The deposition rate is typically around 0.1 nm/s, and can be measured using a quartz crystal monitor. The thickness of the film normally varies between 0.1 nm and a few nanometers. Following film deposition, the substrates are heated to elevated temperatures to break the film into particles. When the particles are to be used as nanowire seed particles this step is often performed inside the nanowire growth reactor. In addition, *in situ* deposition of the metal film inside the nanowire growth apparatus prior to heating has also been reported [37].

A number of parameters can be used to control the particle size and particle surface density to some extent. The temperature used during the heating step affects the particle distribution slightly; higher temperatures yielding larger particles and lower particle surface densities [38]. The use of thicker films also results in larger particles and lower particle surface densities [39]. However, regardless of the film thickness or temperature it is extremely difficult to achieve a low surface density, or to control particle diameter and surface density independently.

Although nanoparticles produced by the annealing of thin films suffer from relatively poor controllability with respect to particle diameter, particle surface density, and particle positioning, this method of producing particles has some advantages. It is a fairly simple, reasonably cheap, and very clean method, especially if the film is deposited *in situ* (which is not possible for most other types of particles). Particles generated by annealing of thin films can be prepared on most types of substrates regardless of size, provided the substrate material allows for diffusion and agglomeration of gold at temperatures that do not destroy the substrate.

2.2.3 Electron Beam Lithography-Defined Nanoparticles

The production of gold particles by EBL can be seen as an extension of the thin-film method, since the generation of EBL-defined particles also requires the evaporation of a thin gold film. However, prior to gold film evaporation, a pattern is defined on the substrate that determines the size, surface density and position of the particles to be produced. A schematic of the EBL-defined particle production process is given in Figure 2.5. In the first step, the substrate (a) is coated with an electron-beam-sensitive resist (b), which is irradiated by an electron beam to obtain the desired pattern. (If a positive resist is used, the exposed areas will be removed upon development, whereas if a negative resist is used, the exposed areas will remain upon development.) Following development (c), a thin gold film is thermally evaporated onto the substrate (d). A liftoff step is used to remove the remaining resist and the excess gold. The entire procedure results in well-defined gold disks precisely positioned on the substrate (e). As for the particles produced by annealing of thin films, a heating step, often performed inside the nanowire growth reactor, is required to transform the gold disks into particles (f).

The major advantage of EBL-defined particles is the high degree of control possible in the process. Not only can EBL-defined particles be homogeneously prepared

with a given, tunable, diameter and surface density, but the exact particle position on the substrate can also be controlled. It is difficult to define exact limitations on particle diameter and density, but the EBL process becomes increasingly difficult with decreasing particle diameter and increasing surface density. As for colloidal particles, the main problem associated with EBL-defined particles is contamination of the substrate surface by organic residues from the chemical preparation process. In addition, EBL-defined particles cannot be prepared on substrates that are too thin, brittle, or otherwise unable to withstand of the large number of handling and processing steps. The process must also be modified slightly depending on the substrate material used, and there is a significant waste of material. Finally, the preparation method itself is rather expensive, and more complicated and time-consuming than the other methods, resulting in low sample throughput.
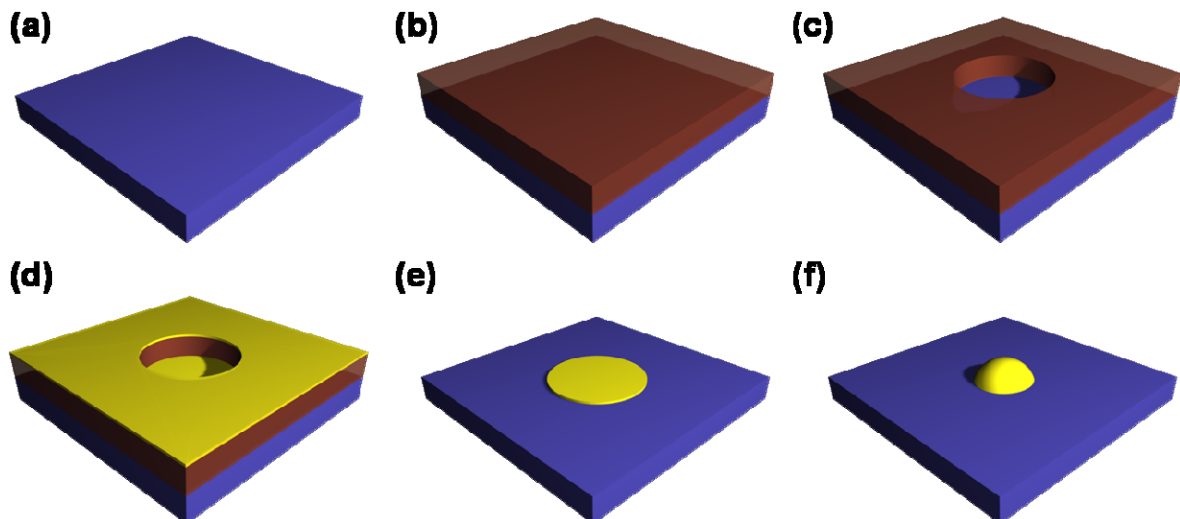
Figure 2.5 Schematic of the EBL process, illustrating how a pattern is defined before deposition of a thin gold film.

Chapter 3

Characterization Methods

In order to be able to tailor the properties of the engineered nanoparticles, careful investigation of the produced particles is crucial. If characterization is performed directly after an adjustment to the nanoparticle production process it is easy to determine whether that specific adjustment improved or impaired the properties of the particles. In addition, thorough characterization with regard to the intended application is important.

Both online and offline characterization are possible, and were used in this work. The main method used for offline characterization for both particles and nanowires were transmission electron microscopy (TEM). In addition to electron-based methods, X-ray-based techniques were also used for particle characterization, primarily for catalysis applications. Most of the nanoparticles and nanowires fabricated in this work are crystalline. This structure is especially suitable for analysis with TEM and X-ray-based characterization techniques, providing information on the atomic level, (although TEM can also be used for non-crystalline materials).

The aerosol-generated particles used in all applications in this work were characterized online using the aerosol generation setup described above. The gold particles used for nano safety applications were also characterized using an online aerosol technique, namely aerosol particle mass (APM) analysis.

3.1 Transmission Electron Microscopy

Microscopy is useful when investigating small structures. Conventional visible-light microscopy (VLM) can be used when working with nanostructures, but its resolution is limited. The smallest feature that can be resolved with a VLM, δ, according to the Rayleigh criterion, is given approximately by:

$$\delta = \frac{0.61\lambda}{\mu \sin \beta} \tag{3.1}$$

where λ is the wavelength of the light, μ the refractive index of the viewing medium and β the semi-angle of collection of the magnifying lens. For simplicity, μ and β can be approximated to unity, which results in a resolution of about half the wavelength of the light. Since visible light has a wavelength between approximately 400 and 700 nm, the investigation of nanowires and nanoparticles with diameters smaller than 200 nm, such as those investigated in this work, requires the use of more powerful microscopes with higher resolution. Microscopy techniques that still make use of visible light but are limited by factors other than the wavelength of the illuminating light, such as scanning near-field optical microscopy and stimulated emission depletion microscopy, can resolve smaller features. However, the use of electron microscopes which have even better resolution, is much more common.

In electron microscopes, the resolution depends on the wavelength of the electrons (although the Rayleigh criterion is no longer valid since it is based on incoherent illumination). Since the de Broglie wavelength of electrons is much shorter (on the order of pm) than the wavelength of visible light, much smaller features can be resolved with an electron microscope than with a VLM. It should be noted, however, that the resolution of an electron microscope is not limited by the wavelength of the electrons, but by the quality of the electromagnetic lenses used, which will be discussed later.

Two different types of electron microscopes were used in this work: a scanning electron microscope (SEM) and a transmission electron microscope (TEM). Note that the abbreviations commonly also refer to the method of microscopy and not only the instrument. SEM provides a good overview of samples containing nanoparticles or nanowires and is reasonably fast and easy to operate. TEM, on the other hand, provides detailed information on the atomic structure of individual nanoparticles or nanowires, but is more time-consuming and rather difficult to

operate. In the remaining part of this chapter, the TEM will be discussed in more detail.

3.1.1 The Instrument

The basic structure of the TEM (Figure 3.1) is not that different from that of a VLM, and can be divided into three components: the illumination system, the objective lens and the imaging system [40]. The role of the illumination system is to create electrons and transfer them to the sample, and consists of an electron gun and condenser lenses. An electron gun comprises an electron source, to create electrons, and an assembly that accelerates and directs the electrons into the rest of the illumination system. Two different types of electron sources can be used in a TEM, thermionic sources and field-emission sources. Thermionic sources are either fine tungsten tips or lanthanum hexaboride (LaB$_6$) crystals which emit electrons when sufficient heat is applied to overcome the work function, Φ, of the material. Field-emission guns (FEGs) consist of a fine tungsten needle that emits electrons when a high electric field is applied close to the tip. Compared to thermionic sources FEGs have a longer lifetime, emit electrons with a smaller energy spread, and are the brightest electron source known (brightness is defined as the current density per unit solid angle of the source). The TEM used in this work (model 3000F, JEOL, Tokyo, Japan) is equipped with a FEG.

Once the electrons have been created by the electron gun, the condenser lenses focus the electron beam onto the specimen. Since electrons are used for illumination instead of light, electromagnetic lenses are used instead of glass lenses to direct the electron beam. An electromagnetic lens is a magnetic field created in the hollow part of a pole piece with a coil surrounding it [41]. Unlike the VLM, where the position of the glass lenses is changed to direct the light, the electromagnetic lenses in a TEM are fixed. Instead, the strength of the electromagnetic lenses is changed by changing the current through the coil in order to change the focus, intensity of illumination, or magnification of the electron beam.

The objective lens and the specimen stage constitute the part of the TEM where the images and diffraction patterns (DPs) are formed. Specimen preparation is important, in order to obtain sufficiently thin specimens to allow high-quality imaging. Fortunately, the nanoparticles and nanowires investigated in this work

19

were thin enough, and complicated specimen preparation processes could be avoided.

Apart from the quality of the specimen, the quality of the objective lens plays a major role in image/DP formation, and the objective lens is clearly the most important lens in the TEM [40]. Unfortunately, electromagnetic lenses, such as the objective lens, suffer from severe limitations, such as spherical and chromatic aberration and astigmatism. Spherical aberration means that the electrons traveling through the electromagnetic lens at different angles from the optical axis will be focused at slightly different focal points. This is due to the different strength of the lens at the edges compared to the region closer to the optical axis. The consequence of spherical aberration is that a point in the object will be imaged as a disk. Spherical aberration can be corrected for by spherical aberration correctors, but they are very expensive. Therefore, only a small number of TEMs are equipped with such correctors today, but the number of spherical aberration corrected TEMs is increasing. Chromatic aberration arises as the electromagnetic lenses focus electrons of different energies at slightly different focal lengths, also resulting in a disk. Monochromators and improved specimen preparation, since thick specimens may result in a small energy loss of some electrons, can be used to correct for chromatic aberration. Astigmatism is caused by a non-symmetrical electric field in the lenses, and low-order astigmatism can easily be corrected for by stigmators which induce a compensating electric field. These aberrations caused by the electromagnetic lenses limit the resolution of a TEM, rather than the wavelength of the electrons.

Following image or DP formation by the objective lens, the imaging system uses several lenses to magnify the image or DP and to focus them onto a viewing screen or a charge-coupled device (CCD) connected to a computer.

TEM can be performed either in conventional mode or in scanning mode, so-called scanning transmission electron microscopy (STEM). In conventional mode the sample is illuminated by a (preferably) parallel beam, whereas in STEM mode the sample is illuminated by a convergent beam; i.e. a small (< 10 nm) probe. In order to form an image in STEM mode, the probe is scanned across the surface. This is particularly useful when images of a specific area of the sample are required, for example, to obtain chemical information from a certain location. A TEM may either be a conventional TEM, a dedicated STEM or be able to work in both modes, such as the instrument used in this work.

Electron gun

Accelerating tube

Anode chamber isolation valve

1st condenser lens coil
2nd condenser lens coil

Condenser aperture assembly

Goniometer

Condenser mini-lens (CM lens) coil

Specimen holder

Objective aperture assembly

Objective lens coils

Objective mini-lens (OM lens) coil

Field limiting aperture assembly

Intermediate lens coils

Binoculars

Projector lens coil

Viewing window

Viewing chamber isolation valve

Viewing chamber

Camera chamber

Figure 3.1 Cross section of a JEOL 3000F TEM.

3.1.2 Imaging

The image created by a TEM is at best a two-dimensional shadow image of a three-dimensional specimen averaged over the thickness of the specimen. Therefore, image interpretation is far from straightforward, and a good understanding of the interactions between the electrons and the specimen is required in order to correctly interpret TEM images. When describing electron–specimen interactions the electrons can be thought of both as charged particles and as waves with a specific amplitude and phase. From a particle view point, electrons that enter a specimen can be scattered either by a single atom or by an electron cloud. If the impinging electron maintains its energy and velocity but changes direction upon scattering, the scattering is said to be elastic. The contrast in TEM images is mainly due to elastically scattered electrons. Inelastic scattering means that the electron changes

21

both direction and velocity while some of its energy is transferred to the specimen. Inelastic scattering can cause damage to the specimen and impair the resolution, but also provides useful chemical information on the sample, as is discussed below. When using the wave approach, the interaction of the electrons with the specimen is called diffraction. The diffraction pattern, i.e. the distribution of diffracted electrons in reciprocal space, contains information on the crystalline structure of the specimen.

The contrast in TEM images is the result of electron–specimen interactions, and is defined as the difference in intensity between two adjacent areas [40]. When the electrons pass through the specimen, changes in both amplitude and phase may occur, giving rise to amplitude and phase contrast, respectively. A combination of amplitude and phase contrast contributes to the image, but often one type dominates. Amplitude contrast can be divided into mass-thickness contrast and diffraction contrast, and are the result of differences in thickness and density or local diffraction differences in the specimen. Mass-thickness contrast is more important for imaging of non-crystalline materials, such as biological materials. This contrast arises from Rutherford scattering of electrons and is therefore strongly dependent on the atomic number, the density, and the thickness of the specimen. Areas of greater mass or greater thickness will show more pronounced scattering and multiple scattering events can occur, reducing the number of electrons transmitted through the specimen in the forward direction. If electrons scattered at large angles (>50 mrad) are used to form the image, as in high-angle annular dark-field microscopy, the contrast depends almost entirely on the atomic number.

Diffraction contrast is related to the local variation in diffraction in the specimen. An amorphous region will scatter less than a crystalline region of the same material, and will therefore appear brighter. In addition, a crystal (particle) oriented closer to a highly diffracting zone will scatter more than a crystal (particle) oriented further from a highly diffracting zone, and hence appear darker. This means that on-axis oriented crystals (particles) are more often selected for investigation than off-axis oriented ones when high-resolution images are required.

Phase contrast is the source of contrast exploited in high-resolution TEM (HRTEM) images and arises when more than one beam (the direct beam and one or more diffracted beams) contributes to the image causing interference. The phase of the electron wave can be changed relative to the direct beam as a result of interactions with the sample, causing phase contrast. The phase contrast is very

sensitive to small changes in the orientation, thickness, and scattering factor of the specimen, as well as variations in the objective lens, such as focus and astigmatism. Because of this, phase contrast can be difficult to interpret but, on the other hand, it is sensitive enough to image the atomic structure of the specimen.

HRTEM images contain a great deal of information which must be correctly interpreted. Therefore, a thorough understanding of the way in which the image is formed is crucial. As mentioned above, a point in the specimen, described by $f(\mathbf{r})$, is transformed into a disk in the image, described by $g(\mathbf{r})$. Therefore, each point in the final image is made up of contributions from many points in the specimen.

The point spread function, $h(\mathbf{r})$, describes this smearing of a point into a disk, and the three terms are related by:

$$g(\mathbf{r}) = f(\mathbf{r}) \otimes h(\mathbf{r}) \tag{3.2}$$

The point spread function describes how certain frequencies (equivalent to lattice distances) are filtered through the lens system [41]. Since the frequency in HRTEM images is related to $1/x$, x being the distance, high spatial frequencies correspond to small distances in the specimen. High resolution therefore requires high spatial frequencies. Since $h(\mathbf{r})$ describes how information in real space is transferred from the specimen to the image, its Fourier transform, $H(\mathbf{u})$, describes how information (contrast) in the reciprocal ($\mathbf{u}$) space is transferred to the image. When using the Fourier transform of the terms in Equation 3.2 they are related by:

$$G(\mathbf{u}) = H(\mathbf{u})F(\mathbf{u}) \tag{3.3}$$

$H(\mathbf{u})$ is known as the contrast transfer function, and can be expressed as a product of the aperture function, $A(\mathbf{u})$, the envelope function, $E(\mathbf{u})$, and the aberration function, $B(\mathbf{u})$:

$$H(\mathbf{u}) = A(\mathbf{u})E(\mathbf{u})B(\mathbf{u}) \tag{3.4}$$

The aperture function describes which spatial frequencies are cut off by the radius of the aperture, the envelope function is a property of the lens related to chromatic aberration and the spatial coherence of the electron beam, and the aberration function describes the effects of spherical aberration.

If the specimen is sufficiently thin that the amplitude contrast can be neglected, it can be regarded as a weak-phase object, and $B(\mathbf{u})$ can be set to $2\sin\chi(\mathbf{u})$, where the term $\chi(\mathbf{u})$ can be expressed as:

$$\chi(\mathbf{u}) = \pi\Delta f u^2 + \frac{1}{2}\pi C_s \lambda^3 u^4 \tag{3.5}$$

where Δf is the defocus value chosen to form the image, and C_s is the spherical aberration constant.

Furthermore, a new quantity, $T(\mathbf{u})$, can be defined, often referred to as the contrast transfer function (CTF).

$$T(\mathbf{u}) = A(\mathbf{u})E(\mathbf{u})2\sin\chi(\mathbf{u}) \tag{3.6}$$

It is, however, important to note that $T(\mathbf{u})$ can only be equated with the CTF if the amplitude contrast is negligible [40]. The CTF is an oscillatory function (Figure 3.2) with maximum contrast transfer at multiple odd values of $\pm\pi/2$ and no contrast transfer for multiple values of $\pm\pi$. For negative values of CTF, positive phase contrast will occur, meaning that electrons appear dark on a bright background. The opposite is true for positive values of CTF. In theory, the CTF can transfer information for any spatial frequency meaning that the oscillations can continue indefinitely. In reality, however, the oscillations are attenuated by the envelope function.

Of the terms affecting the CTF, the minimum wavelength (determined by the electron acceleration voltage) and C_s are fixed values of the microscope itself, but the defocus value, Δf, can be adjusted. At the optimum value of Δf, known as Scherzer defocus, all beams will have an almost constant phase until they cross the x-axis. This cross-over is known as the resolution limit of the microscope. At this point, the point resolution of the microscope is found, and up to this spatial frequency, the contrast in the images can be intuitively interpreted. At higher spatial frequencies the information in the images must be interpreted with image processing methods.
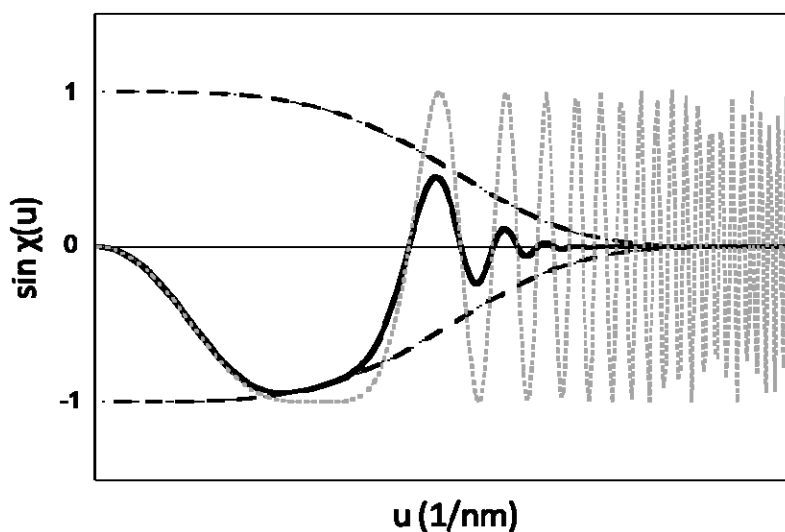
Figure 3.2 The contrast transfer function (CTF) at Scherzer defocus for a 300 kV FEG TEM with C_s = 0.6 nm. The unattenuated function is shown by the dotted gray line, the symmetrical envelope function by the dashed black lines and the resulting attenuated CTF by the full line.

3.1.3 Analytical Electron Microscopy

The chemical analysis of a specimen is possible in TEM, using a technique called analytical electron microscopy, which is based on the transfer of energy from some of the electrons (those inelastically scattered) to the specimen. If an electron from a high-energy beam interacts with an inner-shell (core) electron, the latter can be ejected leaving a hole in the inner shell.

For the electron to be ejected a specific amount of energy, known as the critical ionization energy, must be transferred from the beam electron to the inner-shell electron. After the ejection of the inner-shell electron, the atom is said to be in an excited state. The atom will strive to return to its ground state and can do so by filling the empty inner-shell hole with an electron from an outer shell. The energy released by this transition will result in the emission of either an Auger electron or an X-ray. The entire process is illustrated in Figure 3.3. Both the Auger electron and the X-ray have a characteristic energy related to the energy difference between the two electron shells involved. This energy is element specific and, hence, the detection of Auger electrons or characteristic X-rays provides information on the chemical composition of the sample. In addition, the beam electrons transmitted through the specimen have lost some of their energy when exciting electrons. The energy lost by the electrons from the impinging beam can also be measured to provide information on the chemical nature of the sample.

25
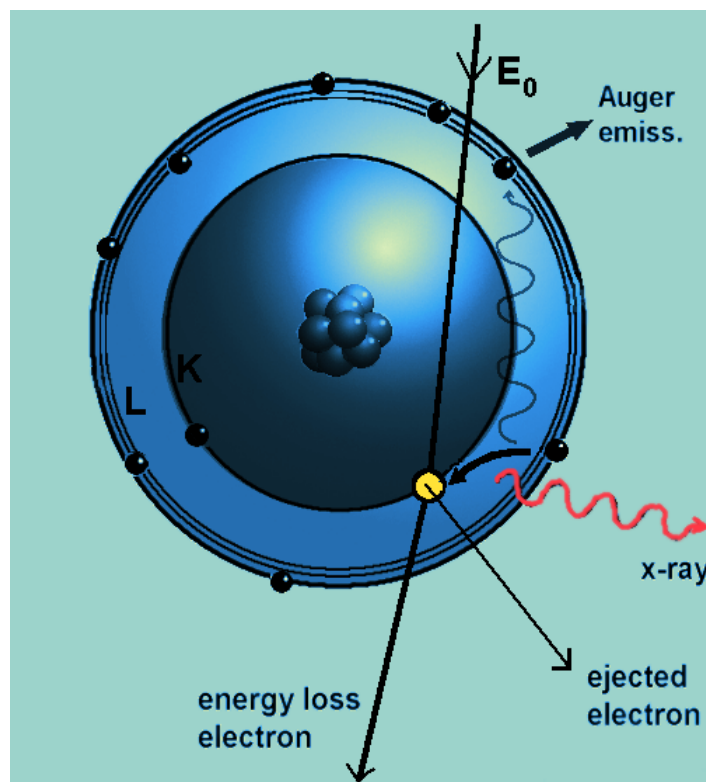
Figure 3.3 Schematic of the mechanism behind characteristic X-ray and Auger electron emission.

X-ray Energy Dispersive Spectrometry

The detection of characteristic X-rays is more common in TEM than the detection of Auger electrons, since the Auger signal is weaker. To detect characteristic X-rays, an X-ray energy dispersive spectrometer (XEDS), typically a Si(Li) detector is used. Inside the detector the incoming X-rays generate a number of electron–hole pairs resulting in a charge pulse proportional to the X-ray energy, which can be measured. The detection limit of the XEDS used in this work is around 1 atomic%, and the lightest detectable element is Be. Quantitative information on the elements in a specimen can also be obtained by XEDS [40]. Furthermore, if the TEM is operated in STEM mode, information on the local chemical composition of the sample can be obtained using a probe smaller than 1 nm. This can be done at a certain point (point analysis), along a line (a line scan), or over a defined area (elemental mapping).

Electron Energy-Loss Spectrometry

A widely used complementary technique to XEDS is electron energy-loss spectrometry (EELS) in which chemical information is obtained from the transmitted electrons. EELS is often used for lighter elements whereas XEDS is often the preferred technique for heavier elements. Due to the scattering events that

occur when the beam electrons interact with the specimen, the transmitted electron beam consists of electrons with a wide range of energies and scattering angles (in contrast to the incoming beam which should ideally be uniform in energy and direction). By using a magnetic prism (located below the CCD camera in the TEM used here) that acts both as a spectrometer and a lens, the transmitted electrons can be sorted according to their energy loss. After passing through the entrance aperture the transmitted electrons travel down a drift tube through the spectrometer and are deflected ≥ 90° by the magnetic field in the prism. Electrons with no energy loss (the majority) are deflected less than electrons that have lost some energy, and hence a spectrum showing the distribution of intensity versus energy loss is formed in the dispersion plane. Since the prism also acts as a magnetic lens, electrons with different scattering angles but the same energy loss are focused at the same point in the spectrum [40].

Figure 3.4 shows a schematic of a typical EELS spectrum. The most intense peak is located at zero energy loss, and is hence known as the zero-loss peak. This peak consists of the elastically scattered electrons (which comprises the majority of the transmitted electrons). The main reason for the finite width of the zero-loss peak is that the incoming electrons have a small energy spread (even if a monochromator is used). The zero-loss peak contains some information about phonon scattering, but this cannot be distinguished from the energy spread and is in any case not very interesting. From a spectrometric point of view, the zero-loss peak is therefore not very interesting (but the information it contains could be useful for zero-loss filtering of thick specimens or in convergent-beam electron diffraction).

The second peak in the EELS spectrum, is located between approximately 5 and 50 eV energy loss, and is referred to as the plasmon peak. This peak corresponds to the interaction of the beam electrons with the weakly bound electrons in the valence or conduction bands. This interaction can result in wave-like oscillations of the electrons, known as plasmons, or in inter- or intra-band transitions (e.g. excitation of valence electrons into the conduction band). From this low-loss region in the spectrum, information can be obtained about the thickness, the band gap, the free-electron density, and the local dielectric constant of the sample [40]. Information like this cannot be acquired with XEDS, but the interpretation of the EELS spectrum is far from straightforward.

The ionization edge, or core-loss edge, is found in the high-loss region of the spectrum (> 50 eV). Similar to the peaks in the XEDS spectrum, this edge contains

direct elemental information on the sample. The intensity of the core-loss edge is much lower than those of the plasmon and zero-loss peaks. Energies higher than the critical ionization energy can be used to ionize an atom, and electrons with higher energies are seen in the spectrum as the slowly decreasing curve at energies above the ionization energy. As for XEDS, quantitative elemental information can be obtained from an EELS spectrum. In addition, information on how the ionized atom is bound, the coordination of the atom, and its density of states can be obtained [40]. However, these techniques have not yet been fully developed.

Energy-Filtered Transmission Electron Microscopy
If the TEM is equipped with an energy filter, such as the Gatan Image Filter (GIF) as in the TEM used in this work, energy-filtered transmission electron microscopy (EFTEM) can be performed. The idea behind EFTEM is that specific energies from the EELS spectrum are selected (or filtered out) to form an image. An energy-selective slit and a slow-scan CCD camera are positioned after the magnetic prism in the GIF to achieve this. Typically, EFTEM images are formed by selecting specific edge energies to create an elemental map of the sample. However, EFTEM images based solely on the electrons from the zero-loss peak (the elastically scattered electrons) may be useful as they can improve the contrast in the image [40]; a technique known as zero-loss filtering, which is mostly used for thick sections of biological materials.
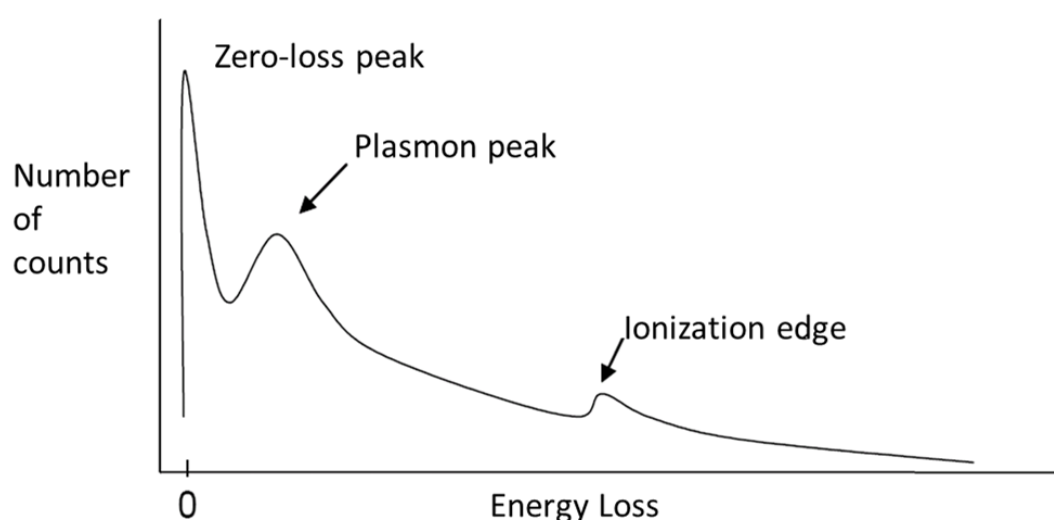
Figure 3.4 A schematic of a typical EELS spectrum showing the low-loss region containing the zero-loss and the plasmon peaks, and the high-loss region containing the ionization edge.

3.2 X-ray Techniques

Instead of using electrons, as in the TEM techniques described above, X-rays can also be used to obtain information about the engineered nanoparticles. X-ray diffraction (XRD) and X-ray photoelectron spectroscopy (XPS) were used for characterization of the engineered nanoparticles in this work. X-rays generated by a synchrotron light source were used in the majority of these measurements. A synchrotron is a particle accelerator where strong magnetic fields are used to convert the energy of accelerated particles into electromagnetic radiation, such as high-energy X-rays [42–44].

XPS is a so-called ultra-high vacuum (UHV) technique, which means that it is normally performed at pressures of 10^{-9}–10^{-6} mbar. XRD can also be performed at such low pressures if it is important to keep the investigated surface very clean, which is often the case for surface XRD (SXRD) studies. XPS setups and XRD setups, which normally work at low pressures, have recently been developed for operation under higher pressure (a few mbar) [45–48]. XRD and XPS measurements were performed at higher pressures on the nanoparticles acting as model catalysts in this work.

3.2.1 X-ray Diffraction

X-ray diffraction is a widely used technique for studying the structure of crystals, in which monochromatic photons are scattered by the electrons surrounding the atoms in a crystal. In order for the photons to interact with the crystal, their wavelength must be on the same order of magnitude as the spacing of the planes in the crystal, and hence X-rays are used. Since the atoms in a single crystal are periodically spaced, all lattice points in the crystal can be said to emit a scattered wave. These scattered waves will interfere with each other according to Bragg's law. Depending on the phase difference, the scattered waves can interfere destructively (zero amplitude) or constructively (twice the amplitude), producing an interference pattern with intense spots, from which information can be obtained about the symmetry and spacing of the scattering centers [49]. Normally, XRD is a bulk analysis technique, but when a grazing incidence angle is used (as in SXRD), the penetration depth is reduced and the technique becomes more surface sensitive.

The study of small (non-ordered) particles with XRD differs slightly from the study of large single crystals. Each particle should preferably be a single crystal, but the

particles are randomly oriented on the substrate, causing the diffraction planes to be randomly oriented. This is analogous to the investigation of a polycrystalline surface, and is referred to as powder diffraction. The interference pattern obtained will consist of rings, formed by the many different diffraction orientations, instead of bright spots. However, the lattice constant and inter-plane distance of the atomic planes can still be determined from these rings [50].

3.2.2 X-ray Photoelectron Spectroscopy

XPS is a technique based on the ejection of core electrons from the investigated sample, by high-energy X-rays. The number and kinetic energy of the ejected photoelectrons can then be related, via the photon energy, to the binding energy of the core electron. The characteristic set of peaks corresponding to the ejection of core electrons from different energy levels are used to identify different elements. The binding energy of the core electron of the atoms surrounding the photo-emitting atom can also be obtained from the XPS spectrum, providing information on the chemical and structural composition [51]. In contrast to XRD, which is a bulk analysis technique (unless a gracing incidence angle is used), XPS is a highly surface-sensitive technique as only electrons ejected from the uppermost atomic layers can escape into the vacuum level and be detected.

3.3 Aerosol Techniques

Some of the aerosol characterization techniques were described in Section 2.1.3 since they are integrated with the aerosol nanoparticle generation setup described there, where DMAs combined with an electrometer were used not only to size-select particles, but also for online diameter distribution measurements. To add an extra dimension to the online characterization, an aerosol particle mass analyzer (APM) was integrated into the system (Figure 3.5) and used during gold particle production for the nano safety application.

3.3.1 Aerosol Particle Mass Analyzer

In an APM, the particle mass is measured by introducing the particles into a gas flow between two concentric rotating cylinders with an electric field between the two cylinders [52]. Only particles within a certain mass interval, for which the

electrical force equals the centripetal force that keeps the particles in a circular orbit within the air gap between the rotating cylinders, will pass through the AMP. A condensation particle counter (CPC) is placed after the APM, which determines the number of particles within a certain mass interval by detecting the light scattered from each particle [53].

For completely spherical particles, the mass can be approximated fairly accurately without the use of an APM, by using the measured mobility diameter (which, for spherical particles, should be equal to their geometric diameter) to calculate their volume and then multiplying this by their bulk density. However, for agglomerated particles that are far from spherical the particle mass cannot be obtained without an APM. Moreover, by connecting the APM in series with a DMA (as in the setup illustrated in Figure 3.5) the effective density, ρ_{eff}, of the nanoparticles can be calculated using the relation:

$$\rho_{eff} = m/\left(\frac{\pi d_m^3}{6}\right) \tag{3.7}$$

where m is the particle mass measured by the APM and d_m is the mobility diameter measured by the DMA. An indication of the configuration of the particles (spherical or agglomerated) can be obtained by comparing the effective density to the bulk density of the particle material.
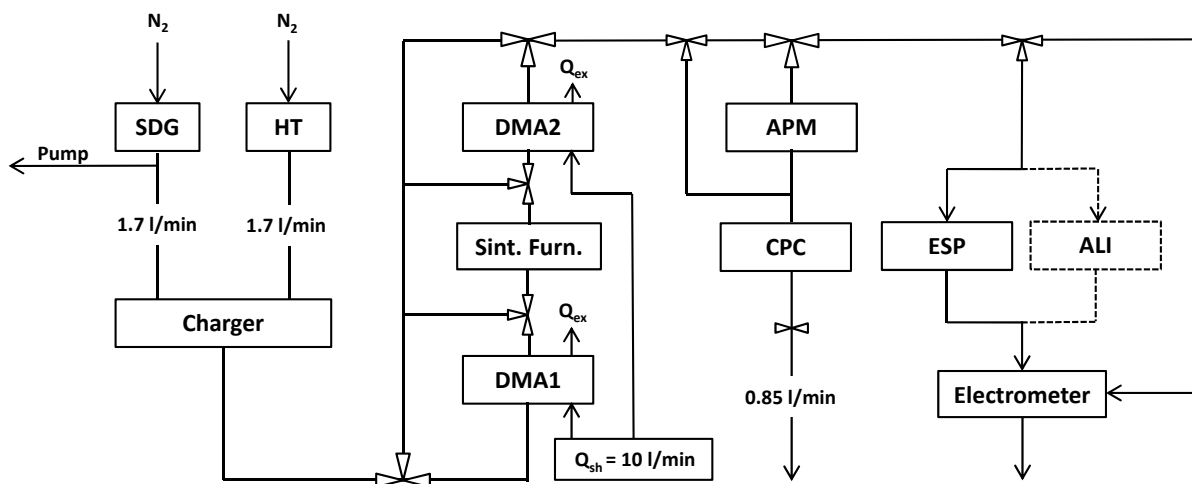
Figure 3.5 Schematic of the aerosol nanoparticle generation and characterization system including the APM and CPC, as well as the possibility to connect an air liquid interface (ALI) deposition chamber.

Chapter 4

Seed Particles for Nanowire Growth

One reason for the considerable interest in semiconductor nanowires is their potential as building blocks in advanced semiconductor devices. However, large-scale production of nanowire-based devices requires better understanding and control of the nanowire manufacturing process. It should be possible to control the dimensions of a nanowire (length and diameter), its crystalline structure and the surface density of nanowires. In vertical device design, which means that devices are manufactured directly around standing nanowires, it is also desirable to be able to control the position of the nanowires on the substrate. When complex combinations of materials, so-called heterostructures, are needed for certain devices, defect-free nanowire heterostructures with well-defined interfaces will be required. Finally, to meet the purity requirements of the semiconductor industry, all possible residues and contaminations from the production process must be removed. One means of achieving this high level of control is to manufacture nanowires by epitaxial growth, usually initiated by a seed particle.

4.1 Nanowires

Nanowires are one-dimensional (1D) rod-shaped structures characterized by a high length-to-width ratio. The diameter is in the size range of tens of nanometers or less, whereas the length is much greater, typically a few micrometers. For nanowires to act as actual 1D structures their diameter must be less than the Fermi wavelength of electrons. When this is the case, electrons can be laterally quantum confined and occupy discrete energy levels in that direction. These quantum confinement effects can be utilized in photonic and electronic applications and for fundamental studies of transport phenomena.

Apart from quantum confinement effects nanowires exhibit three other highly interesting kinds of unique properties, namely surface-related effects, crystal structure effects, and strain–relaxation effects. Surface-related effects arise from the large surface-to-volume ratio of nanowires and can be utilized in nanowire-based biosensor applications. Secondly, the crystal structure of nanowires can be of very high quality with few defects, depending on the production method. Furthermore, the crystal structure can be controlled to a high degree by nanowire growth parameter tuning, which is not as easy in the production of bulk structures. Finally, defect-free material combinations that cannot be achieved in bulk structures, can be realized in nanowires due to the lateral strain–relaxation allowed in nanowires. The ability to control the crystalline quality, and the possibility of producing defect-free heterostructures makes semiconductor nanowires suitable for industrial manufacture and applications.

A number of devices based on nanowires have been demonstrated, such as LEDs [54–58], field effect transistors (FETs) [59–63], solar cells [64–67], thermo-electric devices [68, 69], and biosensors [70–72]. In addition to biosensors, nanowires could also be used for other medical applications in the future. Patterned nanowire arrays have been demonstrated to act as rectifiers and guides for nerve cells on a substrate, which opens up new possibilities for neural network design [73].

Nanowires have been produced from a variety of materials, including metals, metal chalcogenides, metal carbides, oxides, and semiconductors. For an extensive review of the materials systems used for nanowire production see, for example, Rao *et al.* [74]. In this thesis, only semiconductor nanowires will be discussed with the emphasis on III-V semiconductor nanowires; typical examples being InP, InAs, and InSb, as well as GaP, GaAs, and GaSb. In comparison to commonly used semiconductor materials such as Si, III-V materials have some advantageous properties. Firstly, III-V materials (with the exception of GaP) have a direct bandgap, meaning that electrons and holes can recombine directly with conserved momentum while emitting photons during the process. This property makes III-V materials very useful for optoelectronic applications. Secondly, III-V materials exhibit much higher electron mobility, which makes them useful for high-frequency electronic applications.

Nanowires can be made by a number of different techniques, normally divided into top-down and bottom-up methods. Nanowires, as well as other nanostructures, can be produced by lithographically "carving out" the structures from the desired bulk

material, which is referred to as top-down production. This method has been used for many years, and is still the method of choice for producing electronic devices today. However, practical problems arise when using the top-down approach on the nanometer scale. The surfaces of the structures are damaged by the lithographic process, resulting in nanowires of poor crystalline quality. In addition, it may not be able to produce sufficiently small structures with lithographic techniques, and it may be difficult to form heterostructures. To overcome these problems and produce small enough nanowires of sufficiently high crystal quality, the bottom-up approach can instead be used. This means that the nanowires are formed by self-organized growth, atom by atom, in a highly controllable manner.

Among the bottom-up techniques, the vapor phase epitaxy (VPE) method dominates nanowire growth today [75]. VPE is especially advantageous for two reasons. First, a wide range of vapor phase precursors is available, making it possible to grow nanowires from many different types of materials. Second, it is possible to control the growth process, enabling the production of complex nanowire structures. The VPE technique used for nanowire growth in the present work is the so-called metal organic VPE (MOVPE) technique, in which metal organic precursors are used.

The most widely used method to grow nanowires by MOVPE is the particle-assisted method, in which a metal seed particle is used to induce growth, but considerable effort has also been devoted to growing nanowires without the use of seed particles [76–79]. A variety of different metal particles have been used to seed nanowire growth [xvi, 80–83], but gold is by far the most frequently used material. The reason for this is probably the many early reports on successful nanowire growth from gold, as well as the difficulty in achieving and controlling nanowire growth when using particles of other materials. A majority of the nanowires grown in this work were seeded with gold particles.

4.1.1 Metal Organic Vapor Phase Epitaxy

Epitaxial crystal (nanowire) growth means that a substrate with a specific crystal structure is used to direct the growth of the crystal (nanowire) such that the crystal (nanowire) adopts the same crystalline structure as the substrate. If the substrate is of the same material as the crystal (nanowire), the kind of growth is known as homoepitaxy, whereas if the substrate is of a different type of material, it is called heteroepitaxy.

Several different epitaxial growth techniques are used for nanowire growth, including molecular beam epitaxy (MBE), chemical beam epitaxy, and MOVPE. Variations of these techniques include, for example, the use of different precursors, different pressures during growth, and different ways of distributing the precursors. MOVPE is the main technique used in the semiconductor industry today because it is reasonably fast and reliable, a wide range of precursors are available, and the cost is relatively low.

MOVPE is operated under atmospheric or reduced pressures, normally 100 mbar, as was used for the nanowire growth described in this thesis. In MOVPE at least one of the precursor species, usually the group III precursor in the case of III-V material growth, is a metal organic compound. Trimethylindium and trimethylgallium are commonly used as group III precursors, while the hydrides arsine (AsH_3) and phosphine (PH_3) are used as group V precursors. Crystal growth occurs due to reactions between the decomposed metal organic compounds and hydrides at the substrate, with carbon–hydrogen compounds as a residual product. Epitaxial layer growth of GaAs, for example, is carried out between 600 and 700°C to ensure decomposition of the precursors into elemental Ga and As, which are incorporated into the GaAs crystal, forming the layer. The detailed chemical processes involved are highly complicated, but the general chemical reaction for epitaxial GaAs growth can be expressed as:

$$Ga(CH_3)_{3(g)} + AsH_{3(g)} \rightarrow GaAs_{(s)} + 3CH_{4(g)} \tag{4.1}$$
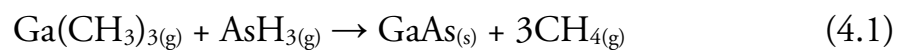
All the methyl groups should ideally be desorbed from the surface to prevent residual carbon levels from contaminating the GaAs crystal. However, carbon contamination is quite common, but can be controlled to some extent by adjusting the growth temperature used [84].

Figure 4.1 shows a schematic of the MOVPE setup used in this work to grow nanowires. The substrates are placed inside the reactor cell on a graphite susceptor, which is heated by a radio-frequency coil outside the reactor chamber. To ensure that the chemical reactions only take place near the substrate, the walls of the reactor cell are kept cold. The growth precursors are transported to the reactor chamber via the run line with an ultra-pure carrier gas, often hydrogen (H_2), where a laminar gas flow is formed over the substrate surface [84]. The gas flows of the different sources are regulated by mass flow controllers (MFCs) and the vent/run

line. Waste material, including unreacted precursors, is removed from the reactor cell and the vent line, and rendered harmless by combustion.

4.1.2 Particle-Assisted Nanowire Growth

Gold-particle-assisted epitaxial growth of semiconductor nanowires typically starts with the deposition of gold particles onto a clean semiconductor substrate. Particles with a specific diameter and known surface density are desirable since the diameter and surface density of particles determine the diameter and surface density of the nanowires. The substrates "decorated" with the deposited particles are then, in the case of MOVPE, placed inside the rector cell (Figure 4.2a). During the first step the substrate is heated to the desired growth temperature, or to a temperature slightly above the growth temperature causing annealing. The purpose of the annealing step is mainly to remove the native surface oxide. Heating takes place under a constant group V partial pressure to prevent decomposition of the substrate at elevated temperatures. Once the growth temperature is reached the group III precursor is also turned on, and nanowire growth is initiated (Figure 4.2b). When the precursor materials come into contact with the gold particle at the elevated temperature an alloy is formed. This alloy particle may be either liquid or solid, depending on its melting temperature. When a certain amount of precursor material has been incorporated into the particle, which is then believed to be (locally) supersaturated, precipitation of material will occur at the particle–substrate interface, referred to as nucleation (Figure 4.2c). Nanowire growth takes place at the particle–nanowire interface as long as a continuous supply of precursor material is available (Figure 4.2d). Growth is terminated by turning off the supply of the group III precursor.
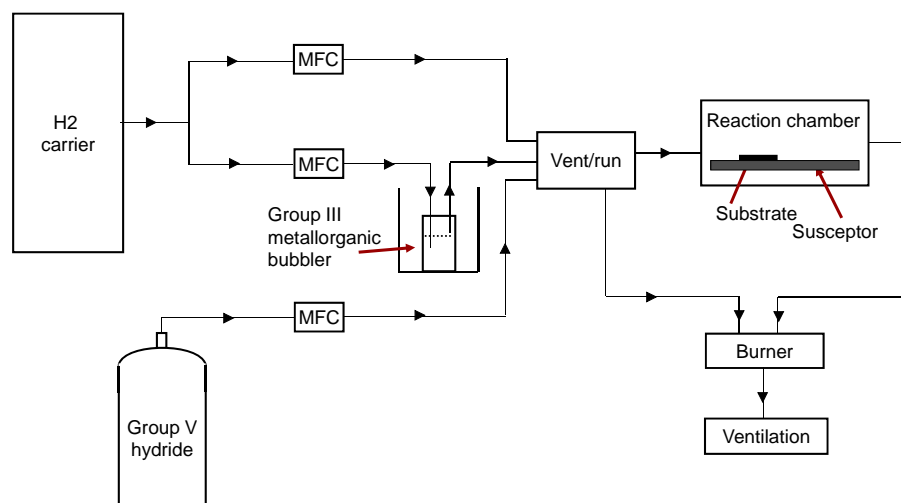
Figure 4.1 Schematic of the MOVPE system used for nanowire growth.

The growth rate of nanowires is largely determined by the supersaturation, which in turn is controlled by the precursor concentration and the growth temperature. Nanowires are typically grown between approximately 380 and 550°C, which is significantly lower than the temperatures used for layer growth. In addition, highly complex nanowire structures can be grown by adjusting the growth parameters. Nanowires containing radial heterostructures, so-called core–shell nanowires (Figure 4.2e), are grown by switching to conditions that favor layer growth [85]. Axial heterostructured nanowires (Figure 4.2f) with very sharp interfaces are grown by abrupt switching between different precursor gas flows [86]. Finally, complex nanowire networks consisting of branched nanowires are grown by the deposition of new gold particles onto the already grown wire (Figure 4.2g), and repeating the growth process (Figure 4.2 h) [87].

Particle-assisted nanowire growth is most often described by the vapor liquid solid (VLS) model developed already in the 1960s by Wagner and Ellis [88]. In this model, the precursors are in the vapor phase, the particles in the liquid phase, and the nanowires in the solid phase. As mentioned above, the particle can also be in the solid phase during growth and, therefore, the vapor solid solid (VSS) model [89] is also used to describe particle-assisted nanowire growth. However, neither of these models fully explains the mechanism of nanowire growth, and the actual role of the particle is still under discussion. Moreover, it is not completely understood why gold particles are superior to particles of other materials in most cases of nanowire growth.
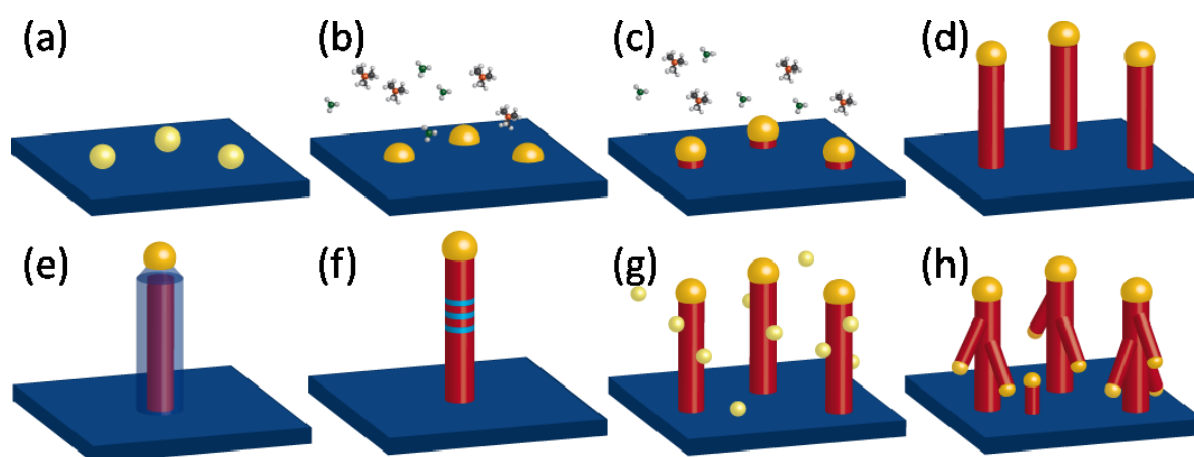
Figure 4.2 Schematic illustrating particle-assisted nanowire growth.

4.2 Particle Effects on Nanowire Growth

Gold-seed-particle-assisted nanowire growth can be affected by the properties of the gold seed particle, such as the diameter, as well as other properties induced by the particle generation or deposition method, as discussed in the sections below.

4.2.1 The Effect of Particle Diameter on Crystalline Structure

The crystalline quality of nanowires may play an important role in nanowire-based electronic and optoelectronic devices. III-V nanowires exhibit the hexagonal wurtzite (WZ) or cubic zinc-blende (ZB) crystal structure, and are often composed of a mixture of the two structures, which is known as polymorphism. Typically, crystal defects such as stacking faults or rotational twin planes are found in III-V nanowires, especially in nanowires with significant mixing of the two crystal structures. Stacking faults and twin planes can act as scattering centers for electrons [90] and, in addition, affect the optical properties of the nanowires [91], which is detrimental in electronic and optical devices.

The ZB and WZ crystal structure of III-V nanowires consists of differently stacked layers. Each layer is a bilayer, consisting of pairs of one group III and one group V atom. Each bilayer is represented by a letter. The WZ and ZB structures are extremely similar, with WZ having an ABABAB configuration and ZB an ABCABC configuration in the close-packed direction. A stacking fault is the term used to describe an irregularity of the WZ structure, such as ABAB<u>C</u>BAB, <u>C</u> being the misplaced bilayer creating the stacking fault. A stacking fault may also be a small region of one crystal structure inside the other. A rotational twin plane, on the other hand, is found in the ZB structure when the stacking sequence switches from ABCABC to ABC<u>A</u>CBACB, <u>A</u> being the misplaced bilayer, referred to as the twin plane.

From attempts to control the crystal structure of III-V nanowires it is known that temperature and V/III ratio can modify the crystal structure to some extent [92, 93]. The addition of dopant species has also been shown to affect crystal structure [94], at the expense of changing the electronic and optical properties of the nanowires. Finally, nanowires more or less free from twin planes can be grown using other directions than the one frequently used, <111>B [95]. However, growth of nanowires in other directions is extremely difficult, and often results in a very low yield.

Another means of influencing the nanowire crystal structure is by changing the diameter of the wire by changing the diameter of the seed particle. Figure 4.3 shows TEM images of InAs nanowires of different diameters, determined by their seed particle diameter, grown at 460°C at a V/III ratio of 130 [Paper III]. At small diameters the nanowires exhibited WZ structure, and were almost completely free of stacking faults (Figure 4.3a). Upon increasing the diameter slightly, the number of stacking faults increased, but the structure was still mainly WZ. At a diameter of 43 nm (Figure 4.3b), the number of stacking faults was roughly 30-35 per micrometer (determined as the average of 10 nanowires with this diameter). Further increase in the diameter led to a further increase in stacking faults, and ZB segments of a few nanometers were seen. At larger diameters the nanowires exhibited a mixture of ZB and WZ structure. At a diameter of 84 nm (Figure 4.3c) the composition was approximately 75% ZB and 25% WZ. At even larger diameters (Figure 4.3d) a transformation to pure ZB was observed, defined as less than 1 WZ segment per micrometer. The pure ZB structure in these large nanowires exhibits periodic twinning, meaning that the nanofacets (the exposed surfaces) are alternating (111)A and (111)B surfaces of the same area. Furthermore, decreasing the nanowire growth temperature increased the proportion of WZ in the nanowires for all diameters. Thus, good control of nanowire crystal structure can be obtained by combining the two parameters growth temperature and seed particle diameter.

One way to predict WZ or ZB crystal structure in III-V nanowires is to consider the ionicity of the chemical bonds, as high ionicity favors WZ structure, whereas low ionicity favors ZB structure. This holds for materials with extreme ionicity values, such as nitride nanowires, which have a very high ionicity and exhibit WZ structure [96], and antimonide nanowires, which have a low ionicity and exhibit ZB structure [97, 98]. However, standard III-V nanowires (GaP, GaAs, InP and InAs) all have ionicity values between these extremes and show polymorphism. Therefore, other concepts must be used when trying to understand the polymorphism in these III-V nanowires.

Akyiama and colleagues [99] suggested that the energy of the side facets in a small structure dominates the total energy of that structure. Since WZ is assumed to have lower side facet energies than ZB, this would explain why small nanowires exhibit WZ structure. However, the diameter at which the transformation from ZB to WZ is predicted is much smaller than that observed for InAs nanowires.
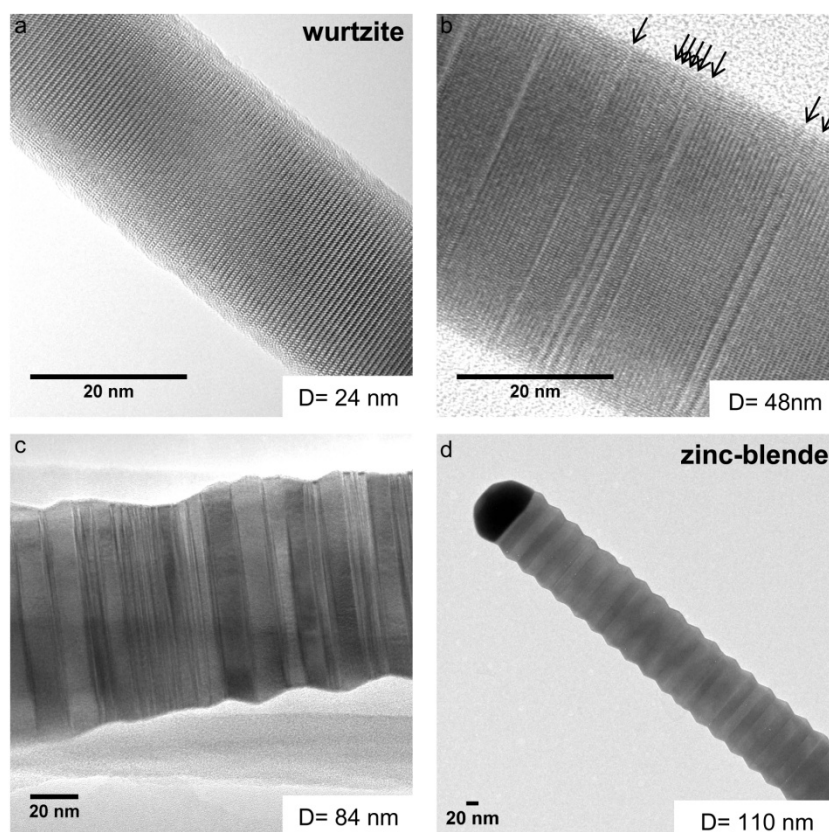
Figure 4.3 Dependence of InAs nanowire crystal structure on diameter from wurtzite (WZ) to zinc-blende (ZB). TEM images viewed along the <-110> zone axis (zinc-blende notation), for increasing diameter, D, from (a) to (d). The crystal structure changes progressively from **(a)** pure WZ, to **(b)** WZ with single stacking faults (see arrows), to **(c)** a mixed WZ–ZB structure and, finally, to **(d)** pure ZB.

Johansson *et al.* [xiv] and Dubrovskii *et al.* [100] used classical nucleation theory with the Gibbs–Thomson effect included in the chemical potential, to explain the cross-over diameter. This approach leads to larger and more realistic cross-over diameters, and seems to provide a reasonable explanation of the effects of diameter on nanowire crystal structure.

4.2.2 The Effect of Particle Diameter on Heterostructures

One of the main reasons for the great interest in semiconductor nanowires is the possibility of easily growing advanced heterostructures, which would be difficult or even impossible in thin films. The epitaxial growth of semiconductor heterostructures in thin films often suffers from problems due to lattice mismatch between the different materials involved. When one lattice-mismatched material is grown on top of another, a large number of defects, such as misfit dislocations, normally appear. These defects are usually undesirable since they lead to severe

degradation of the transport and optical properties of the material [101–103]. However, defect-free or nearly defect-free axial heterostructures of highly lattice mismatched materials can be achieved in semiconductor nanowires [xii, 104]. Due to the geometry of the nanowires and their relatively small size compared to bulk material, the stress induced by the lattice mismatch can be relaxed at the nanowire side walls, hence preventing the occurrence of defects [105].

Although the epitaxial growth of axial nanowire heterostructures has been reported since 1996 [106], it is not straightforward, and far from being fully understood. One major challenge that remains is that it is easier to form straight nanowires in one interface direction than in the opposite interface direction, where the nanowires often grow kinked. For instance, it is well known that straight heterostructure nanowires can be achieved with GaAs on top of InAs, but InAs nanowires grown on top of GaAs are kinked, which has been explained using thermodynamic arguments [107, 108].

Using a novel approach developed in this work, in which heterostructure growth is combined with crystal structure and diameter tailoring, it was possible to grow straight InAs on GaAs axial nanowire heterostructures (henceforth referred to as GaAs–InAs heterostructures) with sharp interfaces [Paper IV]. When growth parameters such as temperature and V/III ratio are tuned to result in InAs with predominantly ZB crystal structure [109], the GaAs–InAs heterostructures grew kinked (Figure 4.4a, c). When the growth parameters were instead chosen to result in InAs with a predominantly WZ crystal structure [109], a considerable fraction of the GaAs–InAs heterostructures grew straight (Figure 4.4b, d).

The crystal structure of the GaAs part seems to have no effect on whether the nanowire heterostructures grow straight or not. However, it affects the nature of the heterostructure interface. If the GaAs part exhibits the ZB crystal structure, significant lateral InAs growth along the nanowire is observed, resulting in the encapsulation of the GaAs wire by an InAs shell. Thus, there is a lateral heterostructure in addition to the axial heterostructure intentionally grown. If instead the GaAs part exhibits the WZ crystal structure, overgrowth of InAs about 50 – 300 nm downwards from the interface is observed, but no full shell is seen. A possible reason for the observed differences could be the different nature of the side facets in GaAs with WZ and ZB crystal structures. ZB twin-free GaAs typically exhibits {112}-oriented side facets, whereas WZ GaAs typically exhibits {1$\bar{1}$00}-oriented side facets [109].
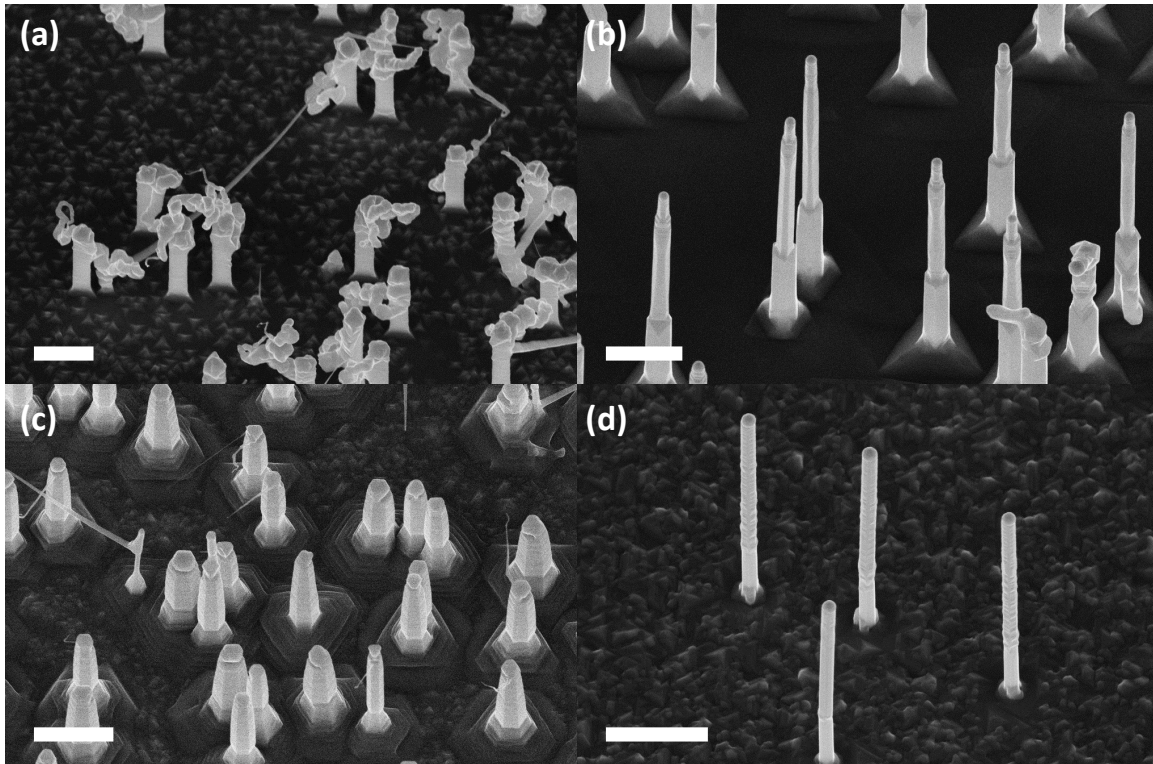
Figure 4.4 SEM images (30° tilting angle) of **(a)** GaAs (ZB)–InAs (ZB), **(b)** GaAs (ZB)–InAs (WZ), **(c)** GaAs (WZ)–InAs (ZB), and **(d)** GaAs (WZ)–InAs (WZ) nanowire heterostructures. The nominal diameter of the nanowires is 100 nm, and the scale bar is 1000 nm.

The {112}-oriented side facets are rougher than the {1$\bar{1}$00}-oriented side facets, increasing the probability of nucleation, and hence promoting lateral growth [xx].

In addition to the effect of crystal structure tailoring on GaAs–InAs heterostructure growth, the diameter of the seed particle (nanowire) also has a significant effect on whether or not the nanowire heterostructure grows straight. The general trend observed when the GaAs part exhibited the WZ or the ZB crystal structure was an increase in vertical yield (percentage of straight nanowires) with increasing nominal seed particle diameter. In the WZ GaAs case, the vertical yield was below 1% when the nominal seed particle diameter was 50 nm or smaller, and increased to about 40% for a nominal seed particle diameter of 100 nm. In the ZB GaAs case, the vertical yield was around 5% at a nominal seed particle diameter of 30 nm, and increased gradually to roughly 65% for a nominal seed particle diameter of 100 nm.

The effect of diameter on heterostructure growth, showing increasing vertical yield with increasing diameter, could be explained by the area-to-length ratio at the

nanowire–particle interface. Because of the decrease in surface tension at the seed particle when Ga is replaced by In, one could expect a situation where it is favorable for the seed particle to wet the nanowire side wall. Since smaller seed particles have their centers of mass closer to the nanowire edge, this effect should be more pronounced for thinner nanowires, making kinked growth more probable. The effect of crystal structure tailoring on heterostructure growth can partly be explained using thermodynamic arguments. First-principle calculations of the heterostructure interface energies clearly showed an energy gain when the InAs part exhibited the WZ crystal structure, compared to the ZB structure [Paper IV] which is consistent with the present experimental results. However, according to the calculations, straight heterostructure growth should also be possible for ZB InAs [Paper IV], indicating that nucleation kinetics also play an important role.

4.2.3 The Use of Gold for Seed Particles

Gold is by far the most widely used material for nanowire seed particles, since it is superior to other materials in most cases of nanowire growth. The major advantage of gold is that it is reasonably easy to achieve high-quality nanowire growth, regardless of the growth parameters. High-quality growth is defined as growth that provides a high yield of straight crystalline nanowires, epitaxially grown in a certain crystal direction. When a <111> oriented substrate is used, which is often the case, the nanowires grow perpendicular to the substrate due to the preferred <111> growth direction of nanowires. To illustrate high- versus low-quality nanowire growth, nanowires seeded with gold and palladium particles, grown under similar conditions, are shown in Figure 4.5a and b, respectively. Although nanowires are formed from the palladium particles, they do not grow straight and are not epitaxial, clearly demonstrating the advantage of gold particles [Paper V].
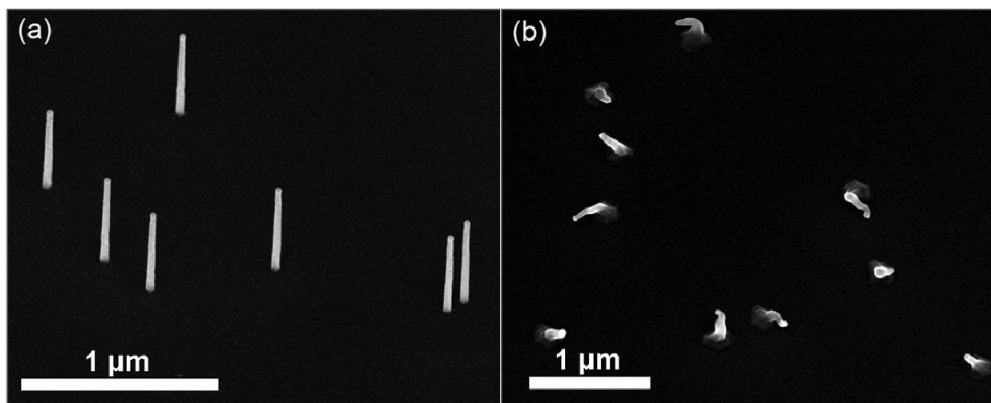
Figure 4.5 SEM images (30° tilting angle) of GaAs nanowires seeded with 30 nm sized aerosol-generated **(a)** gold particles, and **(b)** palladium particles.

Although gold-particle-assisted nanowire growth dominates reports of successful nanowire growth today, there is still no clear understanding of why gold is such a suitable seed particle material. The models typically used for particle-assisted nanowire growth, such as the VLS [88] and VSS [89] models, and the recently suggested more general preferential interface nucleation model [110], all explain the involvement of the particle during growth to some extent, but are applicable to particles of any material. To date, the only attempt to theoretically predict which metals might be appropriate for seeding of nanowires is the model by Nebol'sin and Shchetinin [111]. Their model was developed for the growth of Si nanowires, and is based on the wetting angle of liquid metal droplets on Si. However, the predictions do not generally agree well with experimental data. Since no applicable theoretical model exists, several experimental attempts have been made to find suitable nanowire seed particle materials other than gold [xvi, 80–83, 112]. Apart from improving our understanding of the mechanism behind nanowire growth, finding other particle materials is useful from a device perspective since gold is not really compatible with the silicon semiconductor industry of today [113].

One of the most common explanations of why gold is such a suitable material for nanowire seed particles is that many of the precursor materials used for nanowire growth are soluble in gold. Liquid alloys of gold and indium and gold and gallium exist at temperatures below the growth temperatures commonly used. However, no stable gold–phosphorus or gold–arsenic alloys have been reported, raising the question of how the group V species are incorporated into the nanowire. A possible explanation could be that group V precursors travel along the growth interface or along grain boundaries when the particle is in the solid state [75].

As mentioned above the seed particle may not necessarily have to be in a liquid state for nanowire growth to occur, but it might be an advantage if it is, at least for materials other than gold. Controlled nanowire growth at temperatures below the melting point of an existing liquid-gold-based alloy has been reported [89, 93, 114]. In addition, when materials other than gold have been used for seeding, the particles are often in the solid phase. Although growth is possible from these solid seed particles, the direction of the nanowires is often difficult to control, probably due to the difficulty for a solid seed particle to orient epitaxially with the substrate. GaAs nanowires seeded with iron particles [83] and manganese particles [115], and Si nanowires seeded with copper particles [112] have all been shown to grow in several different directions. In contrast, controlled growth in the <111> direction of

Si nanowires seeded with solid aluminum particles [82], and InP nanowires seeded with solid copper particles [xvi], has been reported.

A further advantage of liquid seed particles is that they are more likely to have a more uniform shape than solid seed particles, which are often faceted, and may thus form nanowires of a more uniform shape. (However, gold is a very soft material, and it probably forms reasonably uniformly shaped particles in the solid state, illustrating yet another advantage of gold.) The final advantage of a liquid seed particle, is the often much higher diffusion of precursor material, such as gallium or indium, through a liquid than through a solid material. The diffusion rate of particles through many solid materials is very slow, resulting in an impractically low nanowire growth rate. Again, gold is the exception, since the diffusivities of both indium and gallium through a solid gold particle are very high. Moreover, gold has a high self-diffusivity coefficient permitting the rapid formation of equilibrium shapes, perhaps one more small advantage of gold compared to other materials.

The catalytic property of gold seed particles with respect to precursor decomposition is the subject of much debate. The common method of determining whether a catalytic effect exists has been to compare the activation energies of decomposition with and without catalyst particles. There have been reports of unchanged activation energies [88, 116–118] as well as reports of enhanced activation energies [119, 120] in the presence of gold, indicating that gold can act as a catalyst in some systems, but that catalytic activity is not a requirement for growth to occur. If catalytic activity were crucial to achieve nanowire growth, other particle materials known to normally have a much higher catalytic activity than gold, such as platinum or rhodium, would be a more suitable choice. Instead, the property of gold as a highly unreactive material, better explains why gold particles are extremely suitable as nanowire seed particles. Unlike many other materials that easily form oxide layers when exposed to air, gold particles larger than 5 nm are known not to spontaneously oxidize in air [121]. An oxide shell surrounding the particle probably prevents the epitaxial orientation of the particle with the substrate, resulting in uncontrolled growth or no growth at all. In addition, gold particles do not react with the commonly used carrier gasses hydrogen and nitrogen, simplifying continuous alloy formation between the growth precursors and the gold particle.

When comparing gold to other materials capable of seeding nanowires, the major difference is that gold has been reported to successfully seed the growth of all types of nanowires under a wide range of growth conditions, whereas other materials may

seed the growth of one type of nanowire under a (very) limited range of growth conditions. Of all the advantageous properties of gold discussed in this section, it seems unlikely that one specific property makes gold superior to other nanowire seed particle materials. Particles of other materials may have some of these advantageous properties, but not all of them, and it is therefore likely that the combination of the advantageous properties makes gold the most universal material for nanowire seed particles [Paper V].

4.2.4 Gold Particles of Different Origin

In the many reports of gold-seeded nanowire growth, the gold seed particles have been generated and deposited by various methods. Successful and highly controlled nanowire growth has been reported from aerosol-generated gold particles [Papers I and III], colloidal gold particles [Paper IV, 122], EBL-defined gold particles [123], and gold particles generated by annealing of thin films [124]. A few reports on nanowire growth from gold particles defined by other methods, such as laser ablation [125] and nanoimprint lithography [126], can also be found, but such techniques are less common and will therefore not be considered here. In this section the effects of gold particle generation and deposition methods (described in detail in Chapter 2) on nanowire growth will be discussed. Six different types of gold particles were used to seed nanowires for this comparison, namely aerosol gold particles generated by spark discharge (SDA) and e/c (ECA), colloidal gold particles deposited by direct deposition (DDC) and by electrospray deposition (ESC), gold particles generated by annealing of thin films (TFA), and EBL-defined gold particles (EBD). These abbreviations for the particles generated and deposited with different methods will be used below.

A direct comparison of the different types of gold particles showed that particle type has little effect on the general characteristics of nanowire growth such as overall growth rate, tapering, and side faceting [Paper VI]. ECA, SDA, ESC, DDC, and EBD particles with diameters of 30 nm and an approximate particle surface density of 1 particle/μm^2, and TFA particles with a broad diameter distribution and a surface density greater than 70 particles/μm^2 all seed straight epitaxial growth of GaAs nanowires at 430°C (Figure 4.6) and 480°C at a V/III ratio of 60. Straight epitaxial growth was also observed for particles with a diameter of 80 nm at these temperatures and V/III ratio. However, at a growth temperature of 380°C a small fraction of the 30 nm diameter nanowires showed kinks during growth, and the growth of free-standing straight nanowires from 80 nm seeds was not possible. This

was found for all the particle types studied, and is not surprising since 380°C is a rather low temperature for the growth of GaAs nanowires [116], and nanowires with diameters as large as 80 nm are known to be more sensitive to growth conditions than slightly thinner nanowires.

All nanowires exhibiting straight epitaxial growth had {112}-oriented side walls consisting of alternating {111}A and B microfacets, regardless of seed particle type. Moreover, for all types of seed particles, of both 30 and 80 nm diameter, the overall nanowire growth rate increased with growth temperature, as expected [116]. No clear difference in nanowire length was observed after growth times of 4 min and longer between nanowires seeded with the different types of particle (except for nanowires seeded with TFA particles) indicating a similar overall nanowire growth rate for all particle types. The TFA-seeded nanowires were much shorter than the other nanowires at all growth temperatures, which is attributed to the much higher particle density on these samples (due to the limitations of the preparation technique), resulting in a lower local supply of growth species. Nanowire growth from ECA samples with a similar particle surface density to the TFA particle samples were used to verify the hypothesis that the higher surface density of particles, rather than particle type, is responsible for the shorter nanowires. As expected, nanowires seeded from these high-density samples decorated with ECA particles also exhibited a reduced growth rate compared to the ECA samples with a density of 1 particle/μm^2.
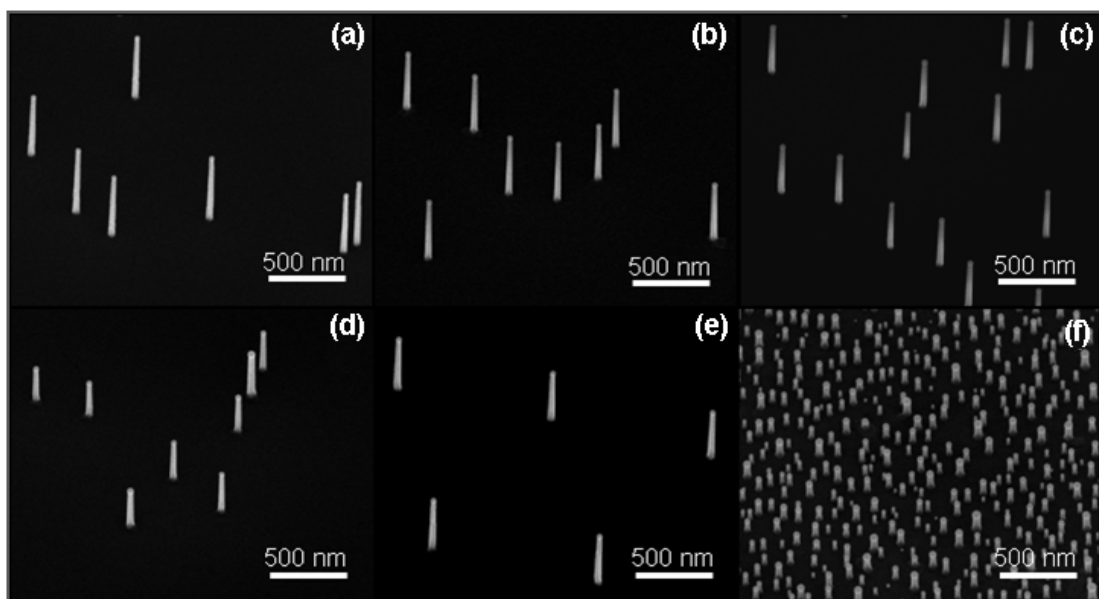
Figure 4.6 SEM images (30° tilting angle) of nanowires grown at 430°C for 4 min, seeded with 30 nm diameter **(a)** SDA, **(b)** ECA, **(c)** DDC, **(d)** ESC, **(e)** EBD, and **(f)** TFA particles.

Little difference was observed between nanowires seeded with different particle types regarding tapering, i.e. non-seeded lateral growth on the nanowire side walls that often results in conically-shaped nanowires [Paper VI]. Tapering was observed to increase with temperature, as expected, since the growth conditions approach those for layer growth. However, the TFA particles and the high-density ECA particles again proved to be the exception. No tapering was observed with these seed particles at any growth temperature, again attributed to the higher particle density rather than particle type.

The major difference between particle types with respect to nanowire growth was found in their behavior during annealing. Annealing was typically performed under group V pressure at a rather high annealing temperature of 650°C in order to achieve TFA particles with the lowest possible surface coverage. At this annealing temperature, a small fraction of the 80 nm particles split into particles of various sizes. Moreover, some of the EBD particles appeared to have moved on the substrate since the positions of the wires deviated from the defined pattern (Figure 4.7a). This is likely to be the case for the other particle types, but could not be confirmed due to the random distribution of particles following deposition. Particles of 30 nm diameter seemed to be unaffected by this annealing temperature.

When growth was performed without the annealing step, i.e. heating directly to the growth temperature, nanowires seeded with colloidal and aerosol-generated particles were slightly shorter than when the annealing step was included prior to growth, under the same growth conditions. However, they still grew straight and perpendicular to the substrate, which is not always the case for TFA- and EBD-seeded nanowires grown without annealing. Regardless of growth temperature, a larger amount of "crawling" and kinked TFA-seeded nanowires was observed when the annealing step was excluded. It thus appears that a certain temperature is needed for appropriate particle formation to take place before the growth precursors can be turned on. For the EBD particles, no annealing seems necessary if a growth temperature as high as 480°C is used. For 80 nm particles, excluding the annealing step was even observed to improve the growth since no particle movement was observed (Figure 4.7b). On the other hand, at the lower growth temperatures the majority of the nanowires were short, kinked, not nucleated at all or "crawled" when annealing was not performed (Figure 4.7c). Hence a certain temperature is needed to provide controlled nanowire growth from EBD particles, in order for the particles to form, and residues from the particle processing to be evaporated [Paper VI].
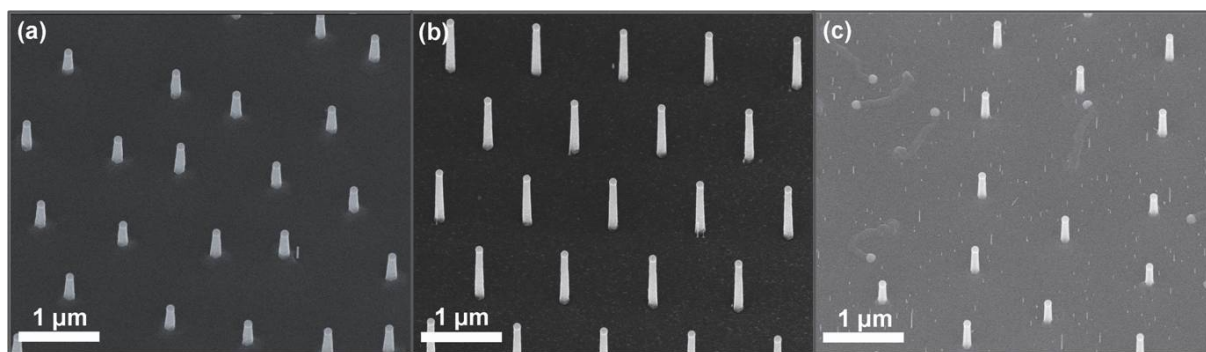
Figure 4.7 SEM images (30° tilting angle) displaying annealing effects for nanowires seeded with 80 nm sized EBD particles and grown for 4 min at: **(a)** 480°C with annealing, **(b)** 480°C without annealing, and **(c)** 430°C without annealing.

Another pronounced difference between nanowires seeded with different particle types is apparent in the very first stage of the growth process. Clear differences in nanowire incubation time were observed, i.e. the time between turning on the growth precursors and the observation of nanowire growth (Figure 4.8). However, the observed differences were too small to affect the final length of the nanowires, and hence the overall nanowire growth rate. Typically, nanowires seeded with aerosol-generated particles had the shortest incubation time, followed by the ECA-seeded nanowires, and then the SDA-seeded nanowires. These were followed by the ESC-seeded nanowires, which showed a similar incubation time to the ECA-seeded nanowires. Nanowires seeded with DDC and EBD particles were found to have longer incubation times, with EBD-seeded nanowires normally demonstrating the longest incubation time. It is difficult to determine and compare the incubation times of TFA-seeded nanowires to the other particle types, due to their broad diameter distribution and high particle density, but they appeared to be very similar to that of nanowires seeded with EBD particles [Paper VI].

An important particle characteristic that seems to be related to the difference in incubation time may be the carbon content in and/or surrounding the particles, which may interfere with the interaction between the gold, substrate, and precursor, hence increasing the incubation time. Carbon-containing chemicals are involved in the preparation of both colloidal particles and EBD particles, but not in the aerosol particle process. Moreover, larger amounts of chemical residues were observed to surround the DDC particles than the ESD particles. This, in addition to the PLL layer used for the deposition of DDC particles, indicates that DDC particles are probably surrounded by more carbon, which may explain the longer incubation time for DDC than ESC particles.

Investigations of nanowire crystal structure showed that there was no pronounced difference between nanowires seeded with different particle types. The only deviation was observed for the TFA-seeded nanowires. At a growth temperature of 430°C nanowires seeded from the other particle types exhibited cubic ZB structure with a number of randomly distributed twin planes. Nanowires seeded with TFA particles also exhibited cubic ZB structure, but contained a significantly lower density of twin planes. This observation is also attributed to the much higher surface density of TFA particles than the other samples, resulting in a considerable difference in local supersaturation, which is known to affect crystal structure [127]. This was confirmed by nanowires seeded from the high-density ECA particle sample, with a similar particle surface coverage to the TFA particle samples, which also exhibited a reduction in twin planes to a level roughly the same as for the TFA particle samples (Figure 4.9).
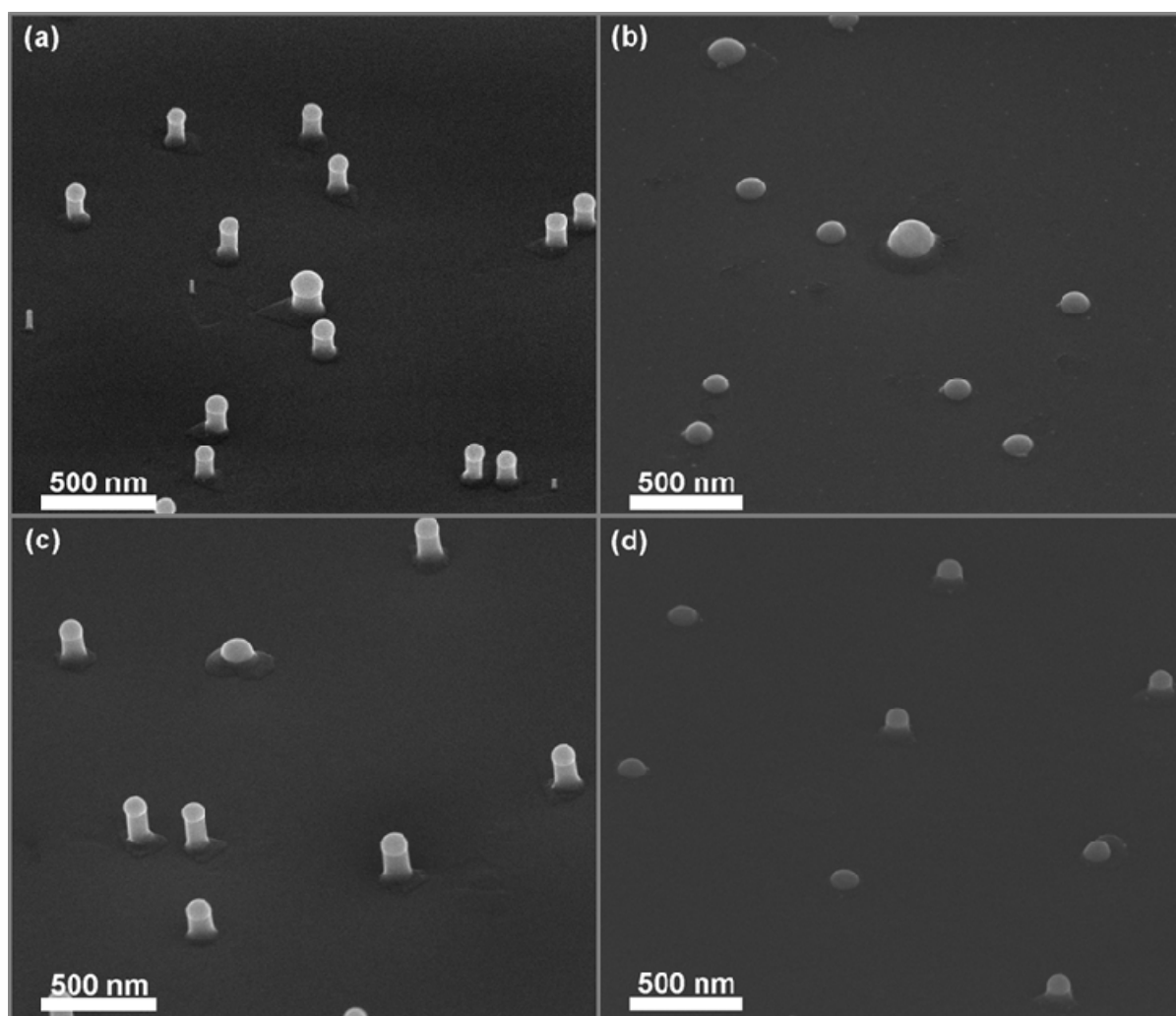
Figure 4.8 SEM images (52° tilting angle) after growth at 430°C for 1 min for nanowires seeded with 80 nm **(a)** ECA, **(b)** DDC, **(c)** ESC, and **(d)** EBD particles.

It can be concluded from the above discussion that there are very small differences in general nanowire growth characteristics between nanowires seeded with the various types of particles. The overall growth rate, microfaceting, tapering behavior and crystal structure were extremely similar. Although differences were found in incubation time and sensitivity to annealing, these can be reduced by using an appropriate annealing temperature and a sufficiently long growth time for incubation not to affect the overall growth rate. It is, however, important to be aware of the number density and size of the particles, since both seem to have a greater effect than the particle type itself, on characteristics such as overall growth, tapering, and crystal structure. These results strongly indicate that direct comparisons of nanowire growth performed in similar systems can be made, even when different types of gold particles have been used as seeds for the wires [Paper VI].
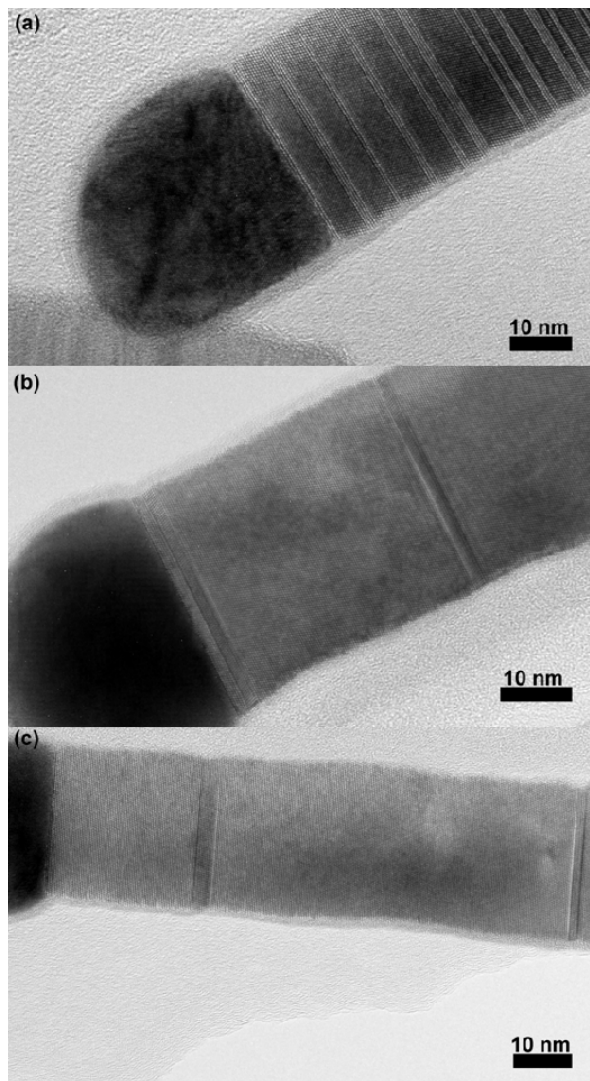
Figure 4.9 TEM images of nanowire crystal structure for nanowires grown at 430°C seeded with: **(a)** ECA particles with a density of $1/\mu m^2$, **(b)** TFA particles with a density of $70/\mu m^2$, and **(c)** ECA particles with a density of $70/\mu m^2$.

Chapter 5

Nanoparticles in Catalysis Research

More than 80% of all chemical products are formed via catalytic processes in today's chemical industry. Additionally, catalysts are used in our cars, motorbikes, and other vehicles to clean exhaust gases. Because of the practical and economic importance of catalysis, it has been studied intensively for decades. Despite all the effort devoted to research in this field, much remains unknown about the atomic-scale processes involved in catalytic reactions, and catalyst development is normally based on a trial-and-error approach. With better knowledge it may be possible to develop more efficient and cheaper catalysts, tailored for specific reactions.

The definition of a catalyst is a substance that accelerates a chemical reaction without itself being consumed in the process. In most cases the catalyst is in a different phase from the reactants, for example a solid catalyst and gaseous reactants, referred to as heterogeneous catalysis. When the catalyst is a solid, typically a metal, the catalytic reaction takes place at, or within a few atomic distances of the surface. Reactants from the gas phase adsorb onto the catalyst surface, diffuse, react, and leave the surface in the form of reaction products. A traditional example is the catalysis of exhaust gases, in which poisonous carbon monoxide (CO) is oxidized into non-poisonous carbon dioxide (CO_2). For this reaction, a single oxygen atom is needed. Oxygen is, however, only present as oxygen molecules (O_2) in air. When O_2 binds to a specific metal surface (such as palladium or platinum) it can dissociate into two single oxygen atoms. The oxygen atom can then combine with an adsorbed CO molecule to form CO_2 which subsequently leaves the surface [50].

To gain a better understanding of the catalyst surface, UHV techniques that allow for investigations of contamination-free surfaces have been used. These studies have provided useful information about surface reconstruction and surface

imperfections, for instance. Catalyst reaction models have been developed by combining UHV measurements with investigations of reactions with various gases at low pressures ($< 10^{-6}$ mbar) [128]. The drawback of models based on UHV techniques is that they do not properly reflect the real catalytic reaction, since industrial catalysts operate at atmospheric, or even higher, pressures. One way to bridge this so-called pressure gap is to perform measurements under higher pressures, as was done in some of the XPS and XRD measurements presented in this thesis (described in Chapter 3). In addition to the pressure gap, there is also a materials gap. A real catalyst is a highly complicated system of materials, usually consisting of an insulating oxide support with dispersed metal nanoparticles of the active catalyst, as well as a wide range of additives to promote a specific reaction. Unfortunately, such systems are normally too complicated to study in surface science experiments. Therefore, simpler model systems have been developed. In the work presented in this thesis engineered nanoparticles were used as a catalyst model system.

5.1 Model Catalysts

To mimic the surface of the nanoparticles in the complex catalyst where the catalytic reactions take place, single-crystal surfaces have been used as model catalyst systems. This approach has been very successful, and G. Ertl was awarded the Nobel Prize in Chemistry in 2007 for his work in this area. However, in order to advance the knowledge, well-characterized model systems that better reflect the real catalyst are needed.

As mentioned above, in a single crystal all the atoms are arranged in a certain repeating order. The long-range order of atoms in the crystal is normally described in terms of repeated units, called unit cells. A unit cell consists of one or more atoms, in a specific spatial arrangement. The atomic order of the single crystal can be described as several unit cells stacked in three dimensions. Figure 5.1 shows the most common three-dimensional unit cells: the simple cubic (sc), the body-centered cubic (bcc), and the face-centered cubic (fcc).
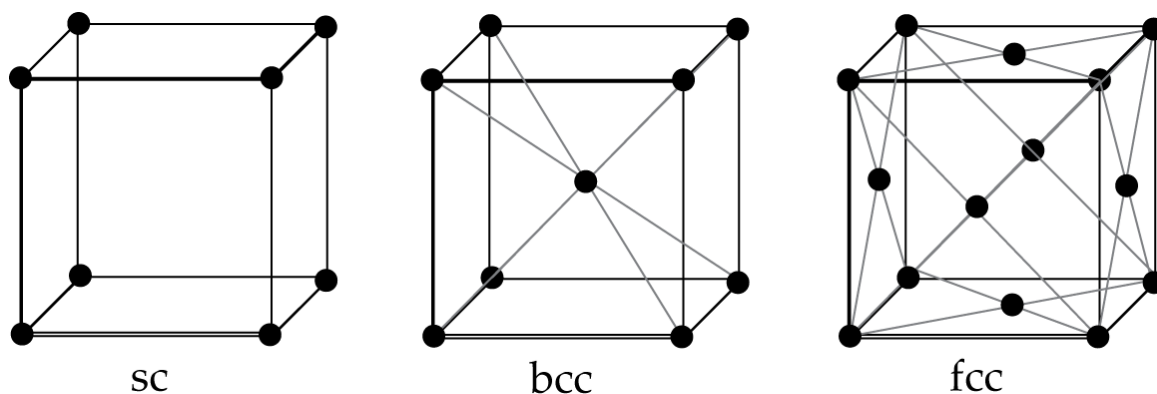
Figure 5.1 The most common unit cells: the cubic (sc), the body-centered cubic (bcc), and the face-centered cubic (fcc).

The surface of the single crystal will have a specific orientation depending on how the crystal is cut: horizontally, vertically or diagonally. These orientations are described by the planes facing the surface. The planes are in turn denoted by Miller indices (*hkl*), such as the low-index (100), (110), or (111) planes. These low-index single crystals with large flat surfaces do not imitate the surfaces of the nanoparticles found in catalysts very well. Nanoparticles consist of differently oriented surfaces containing steps, kinks, defects, and terraces, which will affect the adsorption, diffusion and reactions of atoms and molecules on the surface.

One step towards a more realistic situation is the use of high-index, or so-called vicinal surfaces. A vicinal surface consists of terraces separated by monatomic steps. The atoms at the edge of the steps have similar properties to the atoms in defects or between different facets on a nanoparticle. To bridge the materials gap, different types of nanoparticles and clusters have also been used as catalyst model systems. MBE has been used to deposit metal molecules on a conducting surface with a thin oxide film [129, 130]. The molecules adsorb onto the surface and grow into epitaxial metal islands. The drawback of this method is that MBE is expensive, quite slow, and that it is difficult to control the size and number of metal islands. Colloidal methods have also been used to produce model catalyst nanoparticles [131], but these suffer from the drawbacks described in Section 2.2.1. Furthermore, cluster sources have been used to deposit platinum clusters, consisting of a few atoms, for catalysis investigations [132, 133]. Although the density and cluster size can be controlled, the clusters are much smaller than the nanoparticles in common industrial catalysts, which is a drawback of this model system. In the present work SDG palladium particles were used as model catalysts.

5.1.1 Palladium Aerosol Nanoparticles as a Model Catalyst

The optimal settings for the production of SDG palladium particles differ slightly from those for SDG gold particles. Figure 5.2 shows the size distributions of agglomerated palladium particles generated at carrier flow rates of 3.4 (a) and 5.9 (b) l/min with different spark discharge frequencies. Particle generation was found to be stable for both flow rates, but a higher number concentration of particles was achieved at 3.4 l/min and therefore this flow rate, combined with a spark discharge frequency of 300 Hz, was used for the production of model catalyst particles [Paper VII].

The temperature required to transform the agglomerated palladium particles into compact model catalyst particles is slightly higher than that used for the compaction of gold particles. This is not surprising since the compaction temperature of metal particles is related to the bulk melting temperature of the metal [31], which is higher for palladium than for gold. The transformation of palladium particles into compact particles is shown in Figure 5.3. At a temperature of 800°C the particles are fully compacted, exhibiting a single crystalline core surrounded by an amorphous shell, and this temperature was used to produce model catalyst particles for further measurements using XPS and XRD. TEM, XRD, and XPS measurements strongly indicated that the amorphous shell may well consist of a carbonaceous palladium species. It has been observed that the use of polymer chambers in a spark generator can lead to carbon contamination of the particles [134].
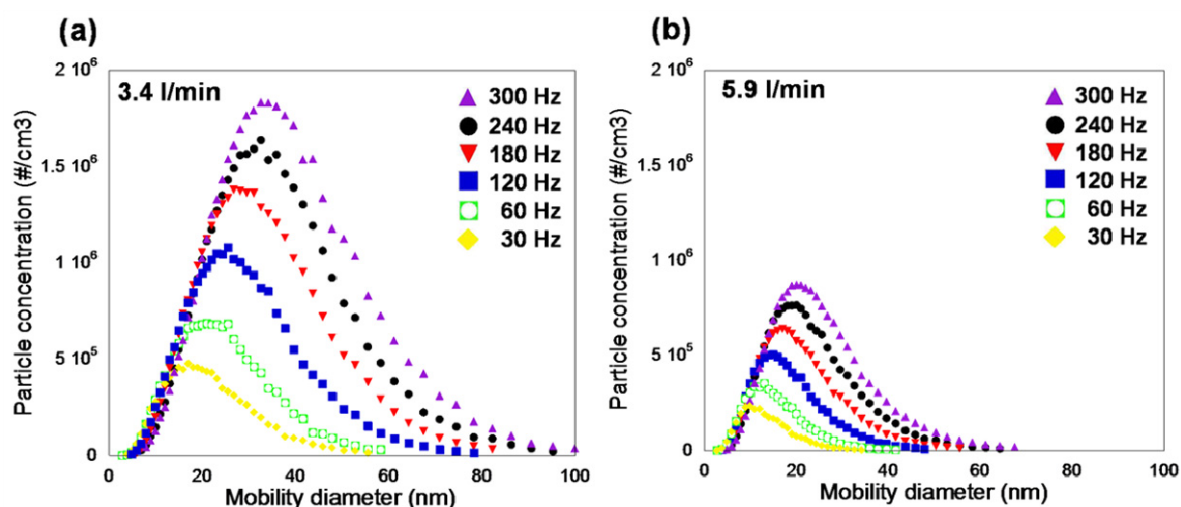
Figure 5.2 Size distributions of agglomerated palladium particles generated at carrier flow rates of (a) 3.4 l/min and (b) 5.9 l/min and spark discharge frequencies between 30 and 300 Hz, measured by DMA 1.
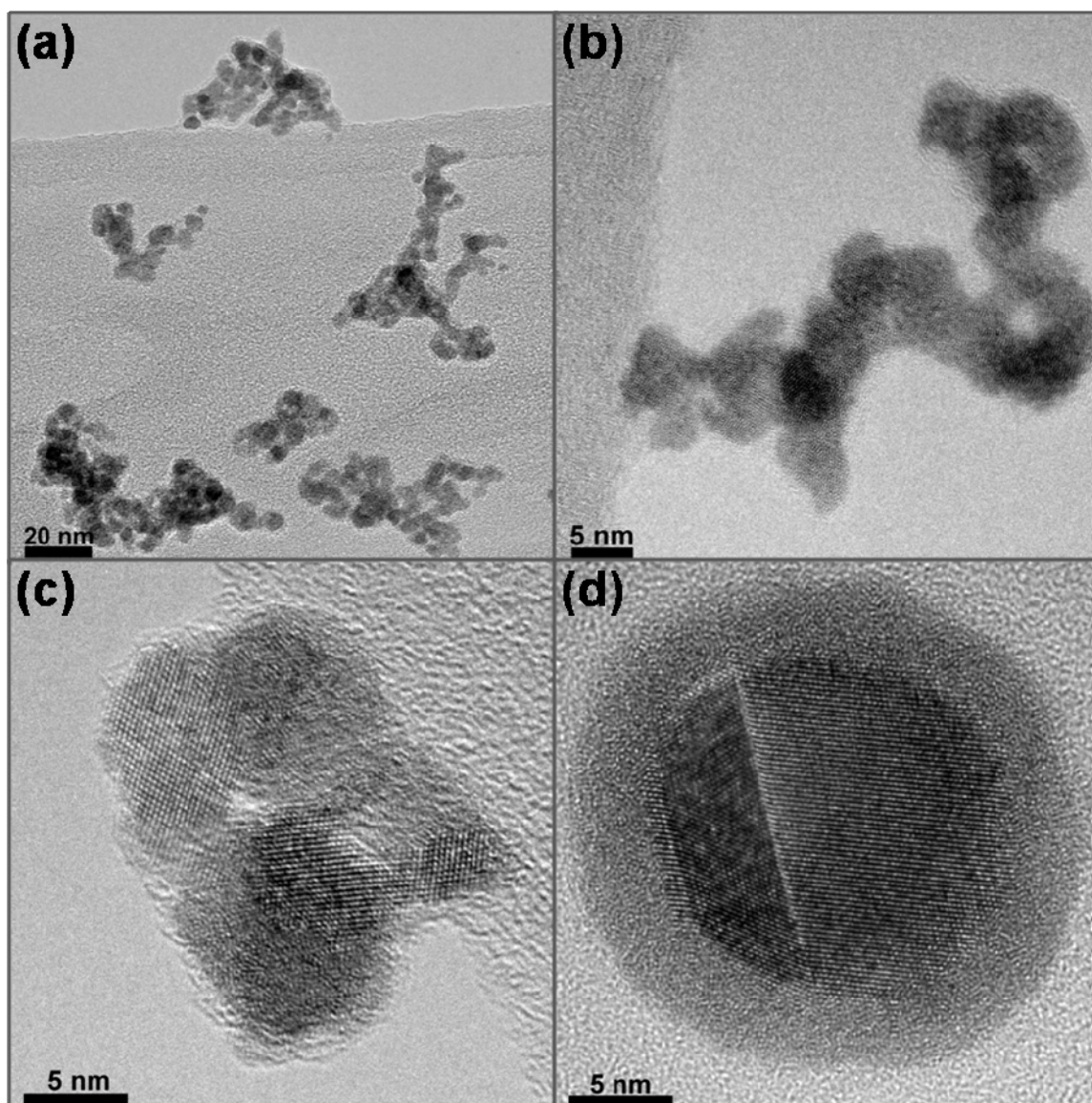
Figure 5.3 TEM micrographs of **(a)** agglomerated palladium particles and palladium particles reshaped at **(b)** 300, **(c)** 600, and **(d)** 1150°C.

For standard XPS and XRD investigations of catalytic properties, a rather high surface coverage of particles, about 5-15%, is required. For particles with diameters of 15 and 35 nm, 10% surface coverage corresponds to 566 and 104 particles/μm^2, respectively. At the optimal conditions, i.e. the conditions under which the highest yield of particles is obtained (a spark discharge frequency of 300 Hz, carrier flow rate of 3.4 l/min, and reshaping temperature of 800°C), deposition times of roughly 6 and 22 h were required to obtain 10% surface coverage for 15 and 35 nm sized particles, respectively [Paper VII]. Even during such long deposition times, the particle concentration per unit time and diameter remained almost constant, indicating the extremely controllable, constant, and simple production of model catalyst nanoparticles by spark discharge.

XPS and XRD measurements performed on the as-generated particles deposited onto silicon and sapphire substrates confirmed the composition of the particles. Furthermore, a shift of the XRD (111) diffraction peak was observed, which could be explained by carbon atoms binding to the palladium atoms, consistent with the carbonaceous shell observed in TEM. The carbon could be removed by oxidizing the palladium particles [Paper VII]. From the above it is clear that aerosol deposition is a useful method for the deposition of nanoparticles on virtually any substrate for use as a model system for studies of catalytic properties. Using this method, particles with a well-defined size can be chosen, and suitable surface coverage obtained, depending on the technique to be used for the investigation of the catalytic properties.

5.1.2 Oxidation and Reduction of Palladium Nanoparticles

With the development of surface science measurement techniques that operate at pressures higher than UHV, several studies of the oxidation and reduction of palladium single-crystal surfaces have been conducted. From such studies it has been found that a surface oxide forms on the palladium metal surface prior to bulk oxidation [135]. In parallel, it has been reported that the oxidation of CO to CO_2 over transition metal surfaces is often more efficient on surfaces with a thin oxide (such as a surface oxide) than on the corresponding clean metallic surface [136–140]. Although theoretical studies support the observation that a surface oxide is indeed the most active phase for CO oxidation [141], the results are still under debate [142, 143]. The active phase must be known for the "intelligent" design of new and better catalysts. Therefore, it is important to perform such studies under catalytically relevant pressures. Moreover, much less is known about the role of surface oxide formation on palladium nanoparticles during oxidation under catalytic conditions.

High-pressure XPS (HPXPS) measurements following the oxidation of 15 and 35 nm diameter palladium particles (with a carbide phase) showed that a thin surface oxide forms before the onset of bulk palladium oxidation (PdO) [Paper VIII]. No significant difference was observed in the oxidation behavior between the two particle sizes, and it was similar to the oxidation of a Pd(100) single-crystal surface. The most pronounced difference between the particles and the single crystal was, that at an oxygen pressure of 0.5 mbar and increasing temperature, the bulk oxide formed at a temperature roughly 40°C lower in the particles (at 210-230°C) than in the single crystal.

Following oxidation, both the oxidized palladium particles and the oxidized Pd(100) single-crystal surface were reduced by 0.5 mbar CO at 100-120°C. The HPXPS measurements strongly indicated that the CO adsorbs onto the PdO surface, both in the particle and Pd(100) single-crystal case. However, when the reduction of the PdO was complete, a significant difference was found between the particles and the Pd(100) single-crystal surface. In the Pd(100) single-crystal case the surface was metallic and was covered with adsorbed CO. The particles, however, did not reduce to the metallic state, but palladium carbide was formed, i.e. the initial state of the particles before oxidation and reduction [Paper VIII]. This indicates that CO can dissociate on the palladium particle surface, whereas no such behavior was observed on the Pd(100) single-crystal surface. Figure 5.4 illustrates the oxidation/reduction cycle of the palladium particles.

These HPXPS results demonstrate the similarities, as well as the important differences, between the single crystals conventionally used as model systems for catalysis and nanoparticles on oxide supports. Not only do these results stress the importance of using a catalytically relevant model system, but also the importance of using catalytically relevant pressures.
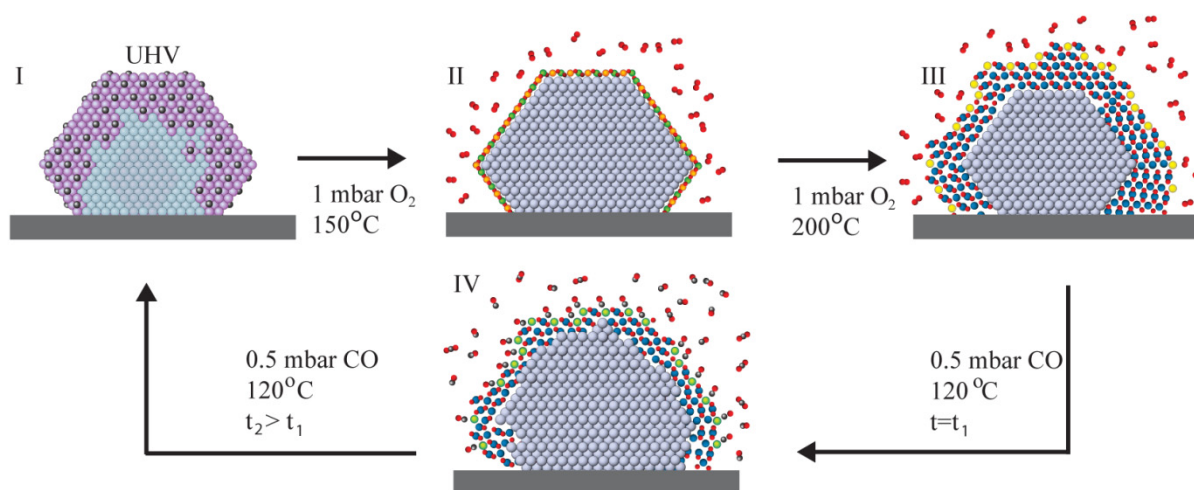
Figure 5.4 Illustration of the oxidation-reduction cycle of palladium nanoparticles. I: Original particles in a carbide phase. When the sample is heated under 1 mbar of O_2, the carbide is reduced, and as the sample temperature reaches 150°C, the HPXPS data suggest that the particles are covered with a surface oxide (II). III: Increasing the sample temperature by 50°C results in particles being surrounded by a shell of PdO. IV: When the O_2 atmosphere is replaced with 0.1 mbar of CO at 120°C, the oxide starts to decompose into metallic Pd and CO_2. The reaction takes place at sites where CO can bind to under-coordinated Pd atoms at the surface of the oxide layer. When the oxide is reduced, we are again left with a carbide phase (I).

Chapter 6

Nano Safety

During the past decade there has been a massive increase in novel applications and products based on nanoparticles. Although belief in the potential of nanoparticles is strong, major concerns have been expressed regarding their effect on human health and the environment [2]. Not only should nanoparticle-based products be safe for consumers to use, but their effects on the environment (e.g. when consumers wash off sunscreens or cosmetics containing nanoparticles) should be harmless. Moreover, the handling of particles during the fabrication of products must be carried out safely. Such issues are being addressed in the broad research field of nano safety, using various different approaches. The aim is to gain a complete understanding and control of the entire life cycle of nanoparticles.

It is well known that the properties of nanometer-sized particles of a certain material are different from the properties of the same material in bulk form. This is exploited in novel products, but is also the reason behind the widespread concern about the safety of nanoparticles. A material known to be non-toxic in bulk form might be toxic on the nanometer scale due to its special properties. Conventional toxicology regulations for materials are often based on total mass, which may not be relevant in the case of nanoparticles. Several studies on the toxicity of nanoparticles have shown that the toxicological response is largely dependent on particle's characteristics, such as surface area, shape, number concentration, mass (of the individual particles), solubility and surface chemistry [144–146]. It is, however, not clear which of these properties plays the most important role in toxicological response and, hence, should be regulated. Extensive research is required in the field of nanotoxicology to elucidate these issues.

One of the most likely ways for nanoparticles to enter the human body is via respiration, since many nanoparticles are airborne; a number of inhalation studies

have been performed [146]. In addition, *in vitro* studies of the interaction of nanoparticles with lung cells have been carried out [145, 147–150]. For nanoparticle toxicology investigations to provide relevant and reproducible results two important issues must be addressed. First, *in vitro* experiments on nanoparticle–lung cell interactions should closely mimic the *in vivo* situation. In order to reproduce genuine *in vivo* conditions, nanoparticles can be deposited from the aerosol phase [147, 149]. A recent development in the *in vitro* study of aerosol nanoparticle–cell interactions is the air–liquid interface (ALI) deposition chamber [151], in which nanoparticles are efficiently and evenly deposited onto cells under physiological conditions, without changing the chemical or physical properties of the particles. Furthermore, it is of the utmost importance in all nanoparticle exposure studies that the investigated nanoparticles are thoroughly characterized. The features of the deposited nanoparticles must be known to enable relevant interpretation of toxicological dose–response relationships and systematic studies of nanoparticle toxicity [152].

The generation and thorough characterization of aerosol nanoparticles for the nano safety studies carried out are discussed below. The generation of titanium dioxide (TiO$_2$) particles for rodent inhalation studies is described. Following this, the characteristics of diesel soot particles from renewable diesel fuel are compared to diesel soot particles emitted from conventional diesel fuel. Finally, a setup allowing the deposition of nanoparticles with highly controllable features, to be used for nanotoxicology studies, is described.

6.1 Rodent Inhalation of TiO$_2$ Nanoparticles

TiO$_2$ in the form of nanoparticles is used in several commercial products such as paint, toothpaste, paper, ink, and sunscreens, to produce whiteness and offer protection against UV light. Although TiO$_2$ is chemically not very reactive in bulk form, TiO$_2$ nanoparticles have been shown to cause adverse health effects such as respiratory tract cancer in rats [153–155]. However, in epidemiologic studies conducted on workers exposed to pigment-grade TiO$_2$ no association has been found between occupational exposure and increased risk of lung cancer [156, 157]. In addition, little is known about the fate of the inhaled TiO$_2$ particles in the human body. Clearly, more research on the subject using well-characterized nanoparticles is required.

The TiO$_2$ nanoparticles used for rodent inhalation studies in this work were generated by spark discharge. Since no data on inhaled TiO$_2$ particles in the 10–50 nm range are currently available, particles with diameters down to 20 nm were generated. In contrast to the generation of palladium and gold particles described in previous chapters, an argon/air mixture was used instead of nitrogen as carrier gas. Further, the radiolabeling of nanoparticles with ^{48}V was investigated, so that the particles could be used for *in vivo* dosimetry analysis. Radiolabeling was performed by proton irradiation of the outermost tip of the TiO$_2$ electrodes [158]. Two types of particles were studied: as-generated agglomerate particles, and particles heat-treated at 950°C.

The morphology and chemical composition of the generated particles were determined from TEM analysis. Both types of particles, the as-generated and the heat-treated, consist of almost spherical primary particles with a geometric diameter of 2–5 nm. The primary particles are linked to form a chain-like, agglomerated morphology with lengths varying between about ten and several tens of nanometers depending on the direction of measurement. This is consistent with the observed median mobility diameter of 20–25 nm, measured with the DMA [Paper IX]. However, high-resolution imaging combined with diffraction measurements showed that the two different particle types had different internal structures (Figure 6.1). The as-generated particles showed an amorphous structure, whereas the heat-treated ones were crystalline. XRD measurements revealed that the crystal structure was anatase. Although the heat-treated particles were slightly more strongly agglomerated than the as-generated particles, it was not surprising that the heat treatment did not make the particles more compact, as was the case for the gold and palladium particles described in previous chapters. A much higher temperature is necessary to bring about such morphological changes in oxide particles [31]. In addition to the morphological characterization, XEDS and EFTEM confirmed the chemical composition of the particles to be TiO$_2$. Finally, it was shown using gamma-spectrometry that the ^{48}V became more strongly bound to the TiO$_2$ particles after heat treatment [Paper IX].
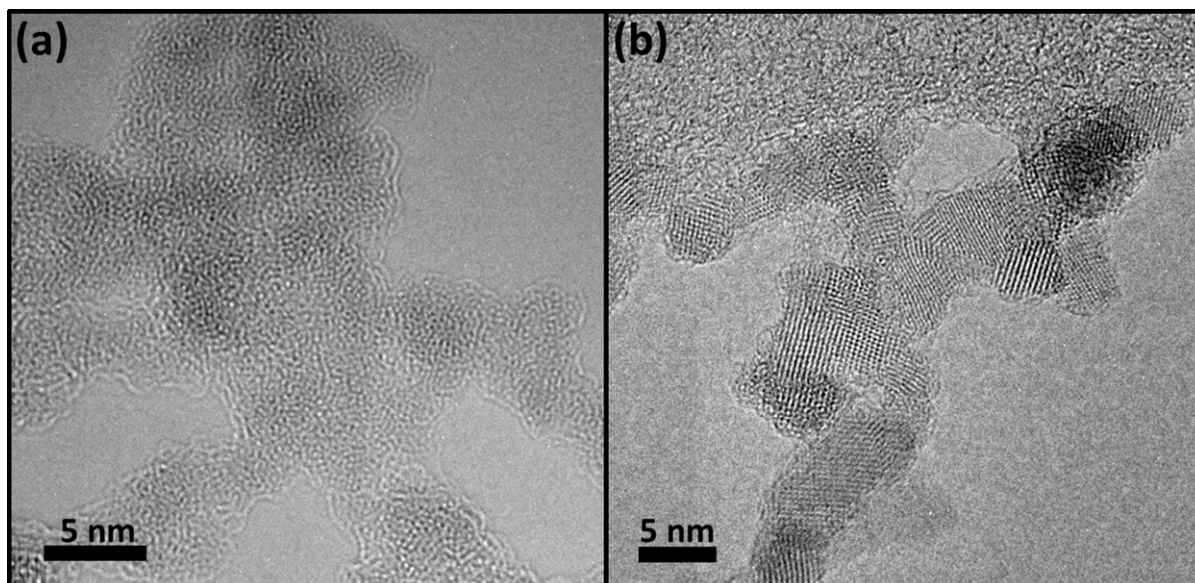
Figure 6.1 HRTEM images showing the internal structure of **(a)** as-generated and **(b)** heat-treated TiO_2 particles.

For rodent inhalation studies, the particles were fed through a rodent inhalation apparatus equipped with an absolute filter and pump unit to adjust the aerosol pressure. Prior to entering the rodent inhalation apparatus the aerosol was humidified by controlled diffusion of water molecules through a semipermeable tube to achieve a final relative humidity of the aerosol between 50 and 80%. The aerosol-generated TiO_2 particles must be used within 5–10 s of generation for inhalation experiments with rodents.

This setup allows for studies of the deposition of very small particles in the respiratory tract and their interactions with lung tissues. It should be noted that such small-sized nanoparticle aerosols for inhalation can usually not be achieved when starting from nanoparticle powders, which is otherwise a conventional method of generating small nanoparticles for such studies. The powder cannot be completely dispersed and the aggregated particles remain in the sub-micrometer range [159]. Hence, the spark generation method used in this work allows biomedical and toxicological studies on the interactions and effects of the smallest nanoparticles with respiratory tract tissues and subsequently with tissues of secondary organs via blood circulation. Such studies will hopefully lead to increased knowledge on the fate of inhaled nanoparticles inside the human body.

6.2 Diesel Soot Particles

The emission of diesel soot nanoparticles to the atmosphere is of great concern due to their adverse effects on health. A common method of reducing particle emission is to use oxidizing aftertreatment devices, such as catalysts (which also reduce the emission of CO and hydrocarbons), or particulate filters. The oxidation properties of the soot particles have a direct effect on the reliability of the particle filters and, further, on the counterpressure caused by the filters, i.e. on fuel consumption [160]. Moreover, it has been demonstrated that the fine structure of the soot particles affects their oxidation properties. Particles with a rougher surface, and hence larger surface area, are more easily oxidized than particles with a smooth surface [161].

Another way of reducing the emission from combustion engines is to replace conventional fossil diesel fuel by renewable diesel fuel based on hydrotreated vegetable oils (HVO). By using renewable diesel fuel, all the regulated emissions, as well as (mass based) fuel consumption, can be reduced [162–164]. However, if this is to be realized, the renewable diesel fuel must be compatible with the oxidizing aftertreatment devices used for conventional fossil diesel fuel in cars and trucks today. To obtain an indication of whether or not this is possible, the oxidation properties and fine surface structure of diesel soot particles were investigated.

To study the oxidation properties of diesel soot particles, the reduction in particle diameter with increasing temperature was monitored, when the emitted particles were fed through a heated tube furnace. Comparing the change in particle diameter of the renewable diesel fuel, denoted HVO, and conventional fossil diesel fuel, denoted EN590, at different engine conditions showed that the change in diameter was similar for both types of fuels under all engine conditions studied [Paper X]. This indicates that the oxidation characteristics of the two fuels are comparable.

HRTEM studies of the fine structure of soot particles emitted by HVO and EN590 also showed little difference. Both particle types are agglomerates consisting of primary particles, with a mean diameter of 26 ± 4 nm. The surface structure of the soot particles is shown in Figure 6.2. In both cases, the soot particles consist of strongly bent graphene layers, affording the soot an "onion-like" structure. However, the structure is not clear or symmetric. The graphene layers are rather irregular, especially near the center of the primary particles. Some of the primary particles included multiple nuclei. According to Su *et al.* [161], multiple nuclei are

caused by the strong bending of the graphene layers. The distances between the graphene layers in the particles are also very similar: 3.76 ± 0.19 Å for the HVO fuel and 3.63 ± 0.19 Å for the particles emitted from EN590 [Paper X]. This is larger than the distance observed between the graphene layers in graphite, which has been reported to be 3.362 Å [165].

In addition to the HRTEM images, electron energy-loss spectra were also obtained from both soot particle samples. It is clear from the carbon K ionization edge in the EELS measurements that the particles are graphite-like, judging from the electron energy-loss near-edge structure (Figure 6.3). No clear difference was seen between the spectra from the different soot samples regarding the first small peak corresponding to the 1s → π^* transition, or in the second broader peak corresponding to the 1s → σ^* transition. Figure 6.3, also shows a spectrum from the carbon film on the TEM grid as a reference, showing clear differences with the sample spectra, with less graphite contribution in the π^* pre-edge peak. Thus, the spectra obtained from EELS measurements confirmed the conclusion that the soot samples were similar in structure, but deviated from the structure of graphite [Paper X].
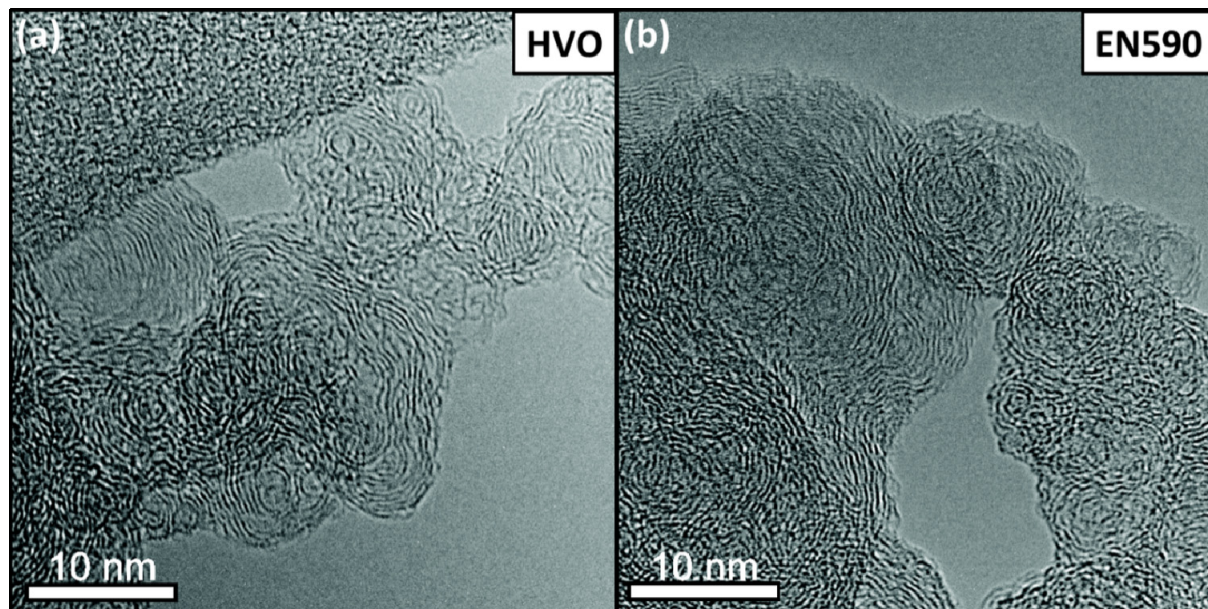
Figure 6.2 HRTEM images of soot particles emitted by **(a)** diesel fuel from a renewable source, and **(b)** conventional fossil diesel fuel.

The fact that the surface structure and oxidation behavior of the soot nanoparticles emitted from both renewable diesel fuel and conventional fossil diesel fuel is similar is important, since it indicates that oxidative aftertreatment devices designed for fossil diesel should also function properly with the renewable diesel fuel studied.
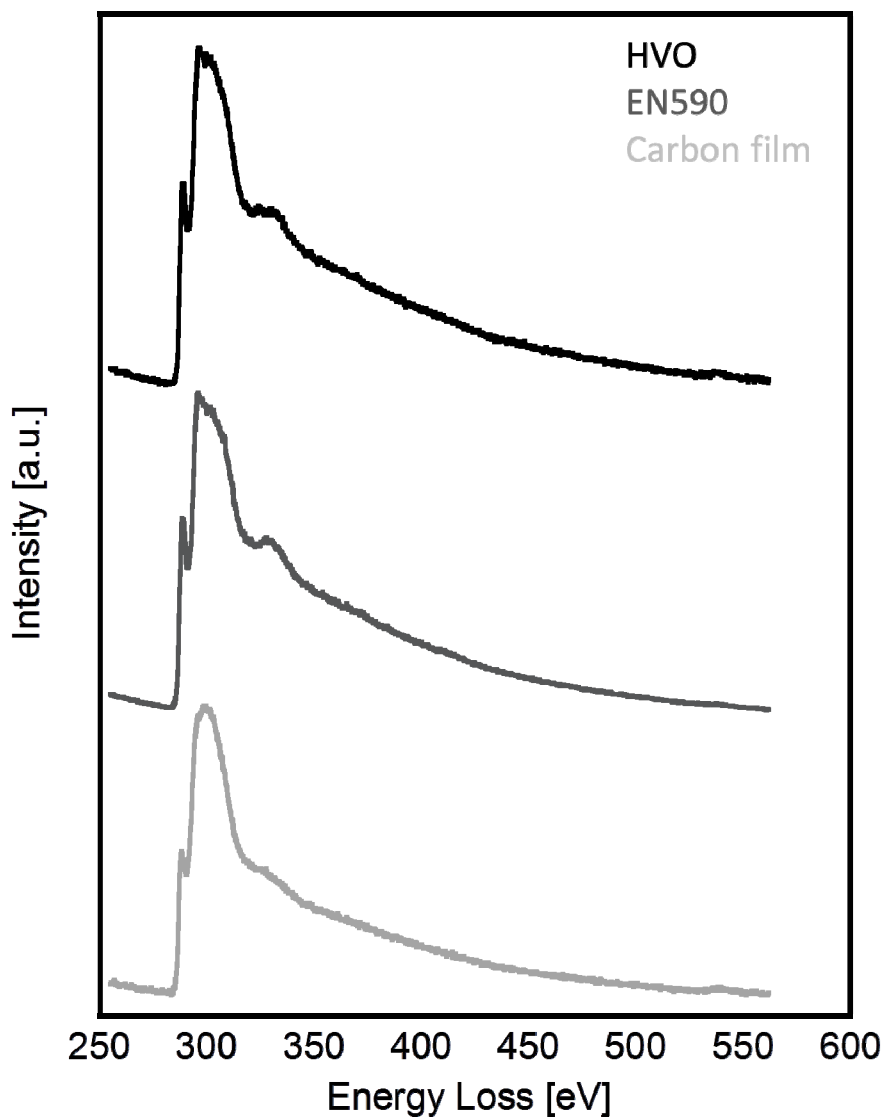
Figure 6.3 Spectra (EELS) of the soot samples from the renewable diesel fuel (HVO, black) and the conventional fossil fuel (EN590, dark gray), together with a spectrum from the carbon film coating on the TEM grid for comparison (pale gray).

6.3 Gold Particles for Nanotoxicology Studies

For a particle generation method to be useful in nanotoxicology exposure studies not only must the important particle characteristics be well controlled and easily measurable, but the concentration of particles must also be high enough to be able to use reasonably short exposure times (hours rather than days). The aerosol nanoparticle system described in Section 2.1.3 was modified to include an aerosol particle mass analyzer. Its use to generate gold nanoparticles for nanotoxicology exposure studies is discussed below.

The advantages of the system, in addition to the facility for detailed on-line measurements, are the flexibility in choice of generation method (HT furnace (e/c) or SDG) and the possibility of easily producing a variety of different types of metal and metal oxide particles. This allows for the deposition of particles of different materials with, for example, the same number concentration or the same mass dose. This in turn allows the direct toxicological comparison of different materials on the nanometer scale, while other parameters are the same. Another advantageous feature of this system is the possibility to use a sintering furnace to reshape the agglomerated particles into more compact particles, which results in a significant reduction in particle surface area. The same number concentration of particles with the same mass, but clearly different surface area, can thus be deposited [Paper XI]. This allows the direct comparison of toxicological responses to particles of different surface areas; a parameter that is believed to play a major role in nanoparticle toxicity [166].

The integration of the APM into the system is beneficial not only because the particle mass can be measured on-line, but also since it provides a reasonably simple way of determining the particle surface area. The conventional method of investigating nanoparticle surface area is by Brunauer-Emmett-Teller measurements [167]. However, this is done by depositing a large number of particles onto a filter, and usually requires a total surface area of 10 m^2. The major drawback of this method is that it is extremely time consuming (around 2 weeks of deposition for the generators used in this study), which leads to poor time resolution of the data, and the fact that the measurement cannot be performed on-line.

The particle surface area can also be calculated from the diameter measurements performed with the DMA, either through the differential mobility diameter (dme) approach or the idealized aggregate (IA) theory approach. In the dme approach, the

particles are assumed to be spherical with a geometric diameter corresponding to the measured mobility diameter. This is obviously a suitable approach for compact, roughly spherical particles but less suitable for agglomerated particles (were the surface area is severely underestimated). The IA approach, described in detail by Lall *et al.* [168], gives the volume of the agglomerated particles by relating the number and radius of the primary particles (evaluated from TEM images) to the measured mobility diameter of the agglomerated particles. In the IA approach it is assumed that the mobility diameter can be calculated by adding the drag force of each primary particle in the whole agglomerated particle. If shielding of inner monomers is present, the mobility diameter will be overestimated with the IA approach. If an APM is used the surface area can also be calculated using the DMA–APM approach. In this approach the mass corresponding to each mobility diameter is extrapolated from the measured data and combined with the bulk density of the particle material to calculate the particle volume [169]. Here point contact is assumed between the primary particles in the agglomerate, thus necking between primary particles is neglected. In both the IA and DMA–APM approach the measured primary particle size must be combined with the calculated volume in order to determine the particle surface area. It is likely that the DMA–APM approach provides a more accurate value of surface area than the IA approach, since the particle mass is actually measured, which leads to fewer assumptions in the estimation of the surface area [Paper XI].

The dose deposited in the alveolar region of the lungs or in an ALI chamber can be estimated using the measurements described above and calculations of particle mass and surface area. Figures 6.4 and 6.5 show the estimated deposited mass and surface area dose, respectively, for gold particles generated using the HT furnace at two different settings, and the SDG at two different settings. Typically, a surface area dose of about 2 cm^2/ h cm^2 is required to cause inflammation in cells exposed to nanoparticles [170]. As can be clearly seen from Figures 6.4a and 6.5a, mass and surface area doses of these values can be reached in the ALI chamber after 1 to 2 hours of deposition, depending on the settings used. This system was shown to be capable of generating and characterizing particles on-line in a stable manner for up to several days [Paper XI], and is thus suitable for particle deposition in the ALI chamber. In contrast, it can be seen from Figures 6.4b and 6.5b that the mass and surface area doses in the alveolar region are well below the values reported to cause an inflammatory response. Cell deposition is used to accelerate a process that may take years in the body, and to achieve a measurable level of inflammatory markers. Lower levels of particles, not measurable by the commonly used analysis methods,

69

may also have an impact on health. Therefore, this setup may also be useful for inhalation studies on the alveolar region in animals, such as the ones described above, although prolonged deposition times would have to be used.
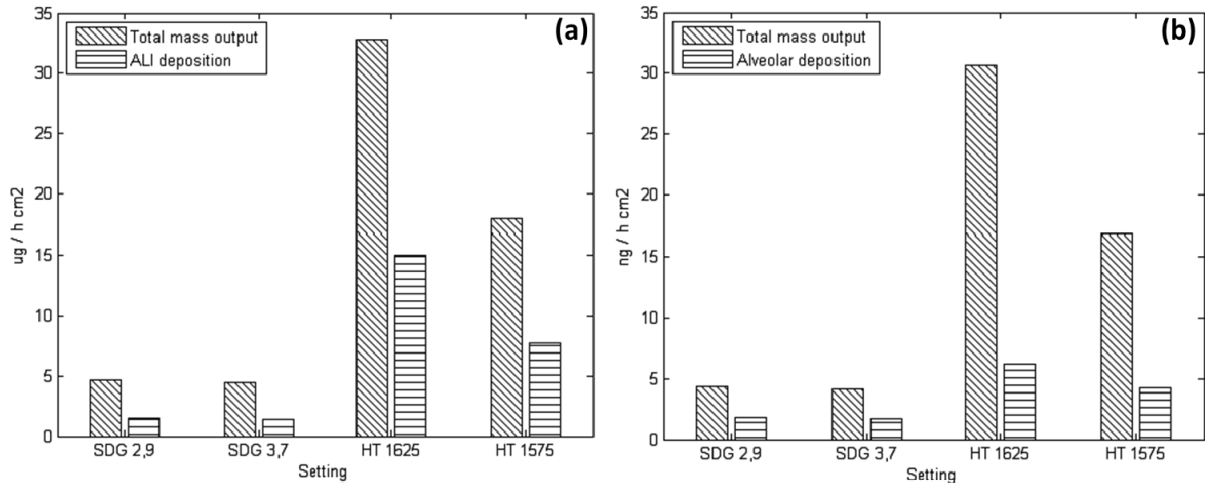
Figure 6.4 The modeled particle mass doses together with the theoretical maximum mass doses for **(a)** the ALI chamber, and **(b)** the alveolar region in the lungs.
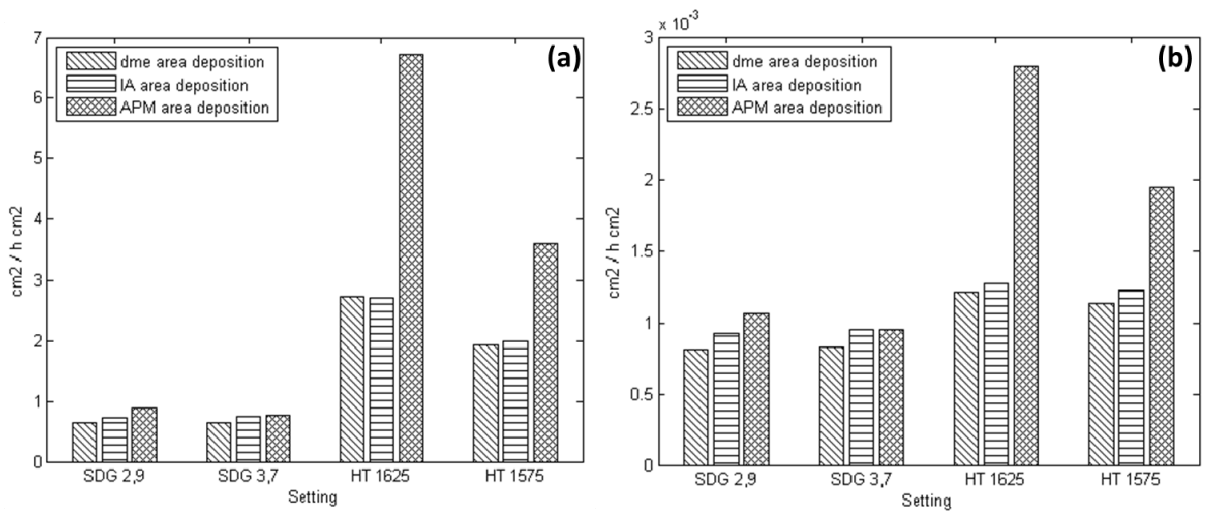
Figure 6.5 The modeled surface area doses together with the theoretical maximum surface area doses for **(a)** the ALI chamber, and **(b)** the alveolar region in the lungs.

Chapter 7

Conclusions and Outlook

Engineered nanoparticles are found in several commercially available products on the market today. Optimistic reports in the media ascribe extraordinary properties to nanoparticles, and predict that they will be used to fabricate many new products that will greatly simplify our everyday life. Other less positive reports voice concern over the possible negative effects of nanoparticles on the environment and human health. Regardless of one's view, the specific properties of nanoparticles, not found in the same bulk materials, are too exciting not to explore and develop. Therefore, nanoparticles will play a major role in future materials. Together with the development of new exciting applications of engineered nanoparticles, it is extremely important to be aware of, and to investigate, the possible effects of engineered nanoparticles on human health and the environment, so that we can handle these particles safely and sustainably.

Many methods can be used to engineer nanoparticles, some of which have been described in this thesis. Most attention was devoted to the generation of aerosol nanoparticles by means of spark discharge, as this allows great freedom in tailoring the properties of engineered nanoparticles for specific applications. For the application of nanoparticles as seed particles for epitaxial growth of advanced semiconductor nanostructures, so-called nanowires, compact spherical gold particles with a specific uniform diameter are desirable. This is important since both the crystalline structure of nanowires and the ability to grow advanced nano-wire heterostructures can be controlled by the seed particle diameter. In addition, gold particles are superior to particles of other materials since they can seed the growth of nanowires of all types of materials over a wide range of growth conditions.

When engineered nanoparticles are used in an attempt to gain a deeper under-standing of the atomic mechanisms involved in catalytic processes, the particles should again be compact, of a specific known diameter, and it should be possible to deposit them at a high surface concentration. From *in situ* reactivity measurements of deposited palladium particles it was shown that model nanoparticles behave differently from conventional catalytic model systems, such as single crystals, in some respects. This emphasizes the importance of bridging the materials gap, i.e. the gap between model systems and real catalysts, in such investigations. The specific properties of nanoparticles used in nano safety research are less important since particles with a wide variety of properties are used in commercial nanoparticle-based products. However, it is of the utmost importance that the specific properties, such as size, shape, mass, surface area, and composition, are known, in order to ensure relevant and reproducible results. Therefore, it is extremely important to be able to engineer well-characterized particles.

Although the spark discharge aerosol generator was developed more than two decades ago, its full potential has still not been investigated. Compared to other methods of producing metal particles, it has some clear advantages with respect to flexibility, cost and being environmentally friendly. In the future, it would be of great interest to study the scale-up of nanoparticle generation by spark discharge. It should be possible to scale up nanoparticle generation, without changing the basic design or idea behind the spark discharge generator, by using several electrode pairs in parallel.

It would also be interesting to conduct studies to find materials other than gold that are capable of seeding the growth of nanowires in order to broaden their application in various devices. One possible route may be to produce gallium or indium particles in a controlled way (perhaps by spark discharge), since "self-seeding" of nanowires seems promising. In addition, further *in situ* TEM studies of particle nucleation, as well as the actual growth, may improve our understanding of the mechanisms behind nanowire growth. Further *in situ* investigations, under even more realistic conditions, would also be useful in the field of catalysis research. To better approximate industrial catalysts, smaller nanoparticles are desirable. This could be made possible by constructing a spark discharge generator with greater freedom to adjust the particle production parameters. In addition, the production of epitaxial nanoparticles would be highly interesting.

The number of future projects in the field of nano safety is almost unlimited. It would of course be exciting to use the nanoparticle system-APM setup for *in vitro* studies of cell deposition. In addition, workplace exposure studies would be useful since workers developing or constructing products will probably be exposed to higher amounts of particles than consumers. The key aspect of successful studies within nano safety is to design relevant experiments in order to gain a thorough understanding of the mechanisms behind a certain toxicological response.

Chapter 8

Populärvetenskaplig sammanfattning

Nanopartiklar
Tillverkning, karakterisering och användningsområden

Nanopartiklar är något som vi alla kommer i kontakt med dagligen, ofta utan att vi är speciellt medvetna om det. Naturligt förekommande nanopartiklar har funnits i alla tider och bildas från våra skogar, från havet eller vid vulkanutbrott, för att nämna några exempel. Även vi människor producerar nanopartiklar, bland annat genom att laga mat, tända levande ljus, göra upp eld, köra bil (från avgasutsläpp och genom friktion mellan däck och asfalt), och genom att röra på oss, eftersom vi själva avger nanopartiklar.

När man pratar om nanopartiklar menar man ofta partiklar med en diameter från en nanometer (1×10^{-9} meter), vilket är lika mycket som våra fingernaglar växer varje sekund, upp till kanske tusen nanometer, vilket är den ungefärliga storleken av en bakterie (dock finns ingen vedertagen definition). En atom har en diameter som motsvarar ungefär 0,1 nanometer. När man pratar om nanopartiklar eller nanoteknik menar man inte enstaka atomer utan partiklar som består av ett antal atomer som samverkar. Att definiera en övre storleksgräns för nanopartiklar är inte heller trivialt. En bra definition är att nanopartikeln ska ha andra egenskaper än de som finns hos partiklar av samma material i bulkform (dvs har en storlek som ligger inom vår "familjära" storleksskala). Två olika typer av effekter uppkommer hos nanopartiklar, nämligen yteffekter och kvantmekaniska effekter. Yteffekter uppkommer eftersom man har en så stor yta i förhållande till volym hos partiklarna på nanoskalan. De kvantmekaniska effekterna uppkommer om nanopartikeln har en dimension av samma storleksordning som våglängden hos en elektron. Båda effekterna kan utnyttjas för att producera material med nya egenskaper och nya

komponenter för användning inom medicin, optik och elektronik, vilket starkt motiverar det stora intresset för nanopartiklar och nanoteknik som finns idag.

Föreliggande avhandling fokuserar på så kallade aerosolpartiklar. En aerosolpartikel definieras som en fast eller vätskeformig partikel som förekommer i någon form av gas. Ordet aerosol innefattar egentligen både partikeln och gasen, men ofta används ordet enbart om själva partikeln. Enligt definitionen av aerosolpartiklar kan nästan alla nanopartiklar anses vara aerosolpartiklar. För att till viss del begränsa definitionen kommer bara partiklar som genereras i en specifik bärargas, t ex kvävgas, att anses vara aerosolpartiklar i den här avhandlingen.

Förutom de oavsiktligt genererade nanopartiklarna har det på senare tid väckts ett enormt intresse för avsiktligt tillverkade nanopartiklar. Målet är att kunna tillverka nanopartiklar med vissa skräddarsydda egenskaper så att de ska kunna användas för olika applikationer eller i olika produkter. Redan idag finns det ett antal produkter på marknaden som innehåller nanopartiklar och många företag arbetar för att kommersialisera ytterligare nanopartikelbaserade produkter. Ett av de vanligaste exemplen är solkrämer med nanopartiklar, men det finns även annan kosmetika och målarfärg som innehåller nanopartiklar. Inom livsmedelsindustrin används nanopartiklar i förpackningsmaterial och i vissa kylskåp, och inom klädindustrin tillverkas kläder gjorda av tyger som innehåller nanopartiklar. Inom medicinen använder man nanopartiklar bland annat som fluorescerande markörer, som kontrastförstärkning i magnetkameraundersökningar, och för framställning av konstgjord vävnad. Det finns även en stark tro på att nanopartiklar ska kunna användas för riktad läkemedelstransport inuti våra kroppar, exempelvis för att bekämpa cancer. Forskargrupper har även demonstrerat att det går att bygga lysdioder och gas-sensorer baserade på nanopartiklar.

I den här avhandlingen har tillverkning av nanopartiklar, främst med hjälp av aerosolmetoder, undersökts grundligt. Målet har varit att optimera tillverknings-processen för att tillverka nanopartiklar med specifika egenskaper som passar för specifika användningsområden. Efter optimering av tillverkningsprocessen har nanopartiklarna använts för forskning inom tre olika användningsområden: För tillverkning av så kallade nanotrådar, för forskning inom katalysområdet, och för forskning inom området nanosäkerhet, där man undersöker hur nanopartiklar kan tillverkas och hanteras på ett säkert sätt.

De två främsta tillverkningsmetoderna för nanopartiklarna i det här arbetet var genom att använda en gnisturladdningsgenerator (SDG) och genom evaporation/ kondensations (e/c) metoden, vilka båda är aerosolmetoder. Båda metoderna bygger på att man med hjälp av värme förångar materialet man vill tillverka nanopartiklar av. Genom att använda en bärargas, tex kvävgas, och transportera bort det (övermättade) förångade materialet så att det kyls ner, kommer gasen att nuekleera. Det innebär att det bildas små kärnor av fast material. De här kärnorna kommer sedan att växa i storlek, dels genom att mer ånga kondenserar på dem, dels genom att vissa kärnor slår sig ihop och bildar en större kärna. Slutligen har man sin bärargas fylld med små partiklar med en diameter på mellan en och ett par nanometer, så kallade primärpartiklar. De här primärpartiklarna kommer sedan, i sin tur, att slå sig ihop till större agglomeratpartiklar.

För att bilda sin partikelånga, i SDG metoden, använder man sig av två elektroder (av materialet man vill tillverka sina partiklar), varav den ena är kopplad till en kondensator. När urladdningsspänningen hos kondensatorn nås kommer den att ladda ur i en gnista mellan de två motriktade elektroderna, och material kommer att förångas (Figur 8.1). För att påverka tillverkningsprocessen kan man bland annat ändra gnisturladdningsfrekvensen, avståndet mellan elektroderna, gasflödet hos bärargasen, elektrodmaterialet och även typen av bärargas. I e/c metoden använder man en ugn för att värma upp en bit fast material (som man vill tillverka sina partiklar av) till den börjar förångas. För att påverka tillverkningsprocessen kan man bland annat ändra sitt material, temperaturen på ugnen och gasflödet genom ugnen.
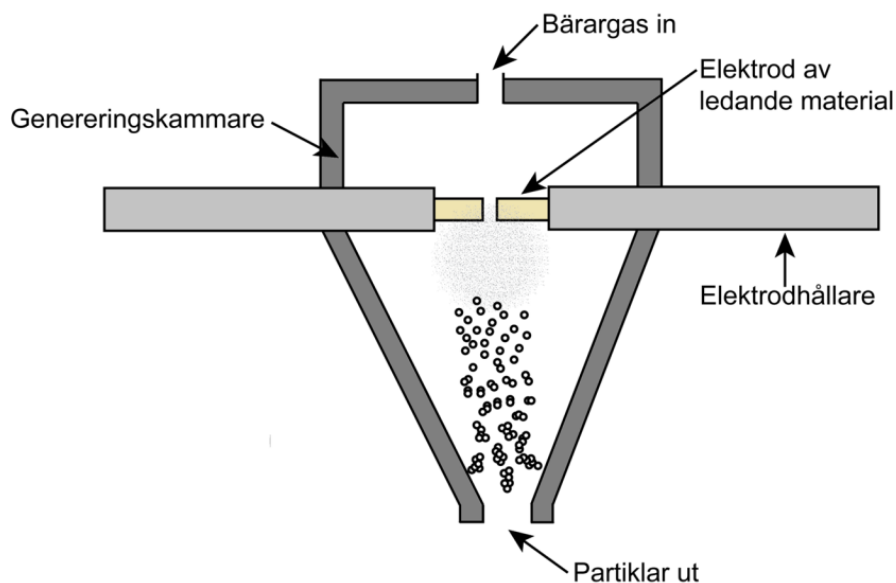
Figur 8.1 Schematisk bild av gnisturladdningsgeneratorn.

Partiklarna som bildas från de båda generatorerna är agglomeratpartiklar, dvs förgrenade kedjelika partiklar som består av hopslagna primärpartiklar (Figur 8.2a), med en relativt bred storleksfördelning. För vissa användningsområden krävs dock att man har mer kompakta partiklar med en specifik storlek. Genom att skicka partiklarna från generatorerna vidare in i ett aerosolnanopartikel-system kan man både ändra form på dem (Figur 8.2b) genom att värma upp dem i en ugn vilket gör dem mer kompakta, mäta deras storlek, samt sortera ut partiklar av en viss storlek. Med hjälp av systemet kan man även deponera ett kontrollerat antal partiklar av en viss önskad storlek ner på ett substrat som kan vara av vilken typ som helst, t ex en bit papper, en kiselskiva, eller en vätskelösning.

Det första användningsområdet för de producerade nanopartiklarna som har undersökts i den här avhandlingen är för tillverkning av nanotrådar av halvledarmaterial. Nanotrådar är stavliknande nanostrukturer med en diameter i storleksordningen tiotals nanometer och en längd mellan ett par hundra nanometer och ett par hundra mikrometer (Figur 8.3a). De har ofta en kristallin struktur vilket innebär att atomerna i nanotråden är ordnade i ett specifikt mönster (Figur 8.3b), istället för att vara slumpmässigt positionerade som i amorfa strukturer. Halvledande nanotrådar förväntas bli mycket användbara i bland annat framtida elektronik- och optoelektronik-komponenter samt för att bygga nya typer av biosensorer.
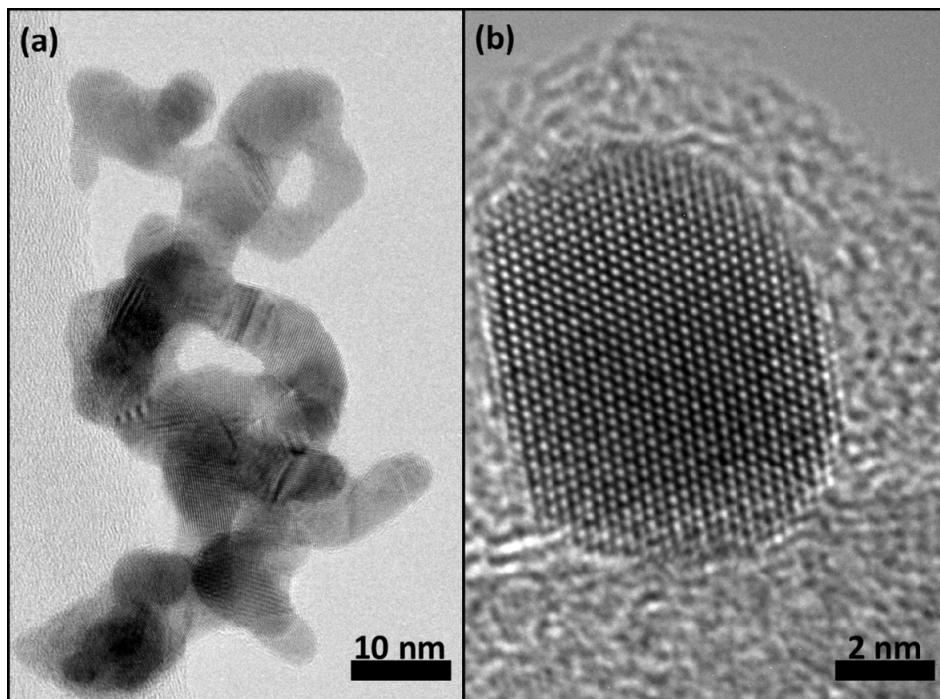
Figur 8.2 Guldnanopartiklar i formen av (a) en agglomeratpartikel och (b) en nanopartikel som blivit kompakterad efter att ha skickats genom en ugn.
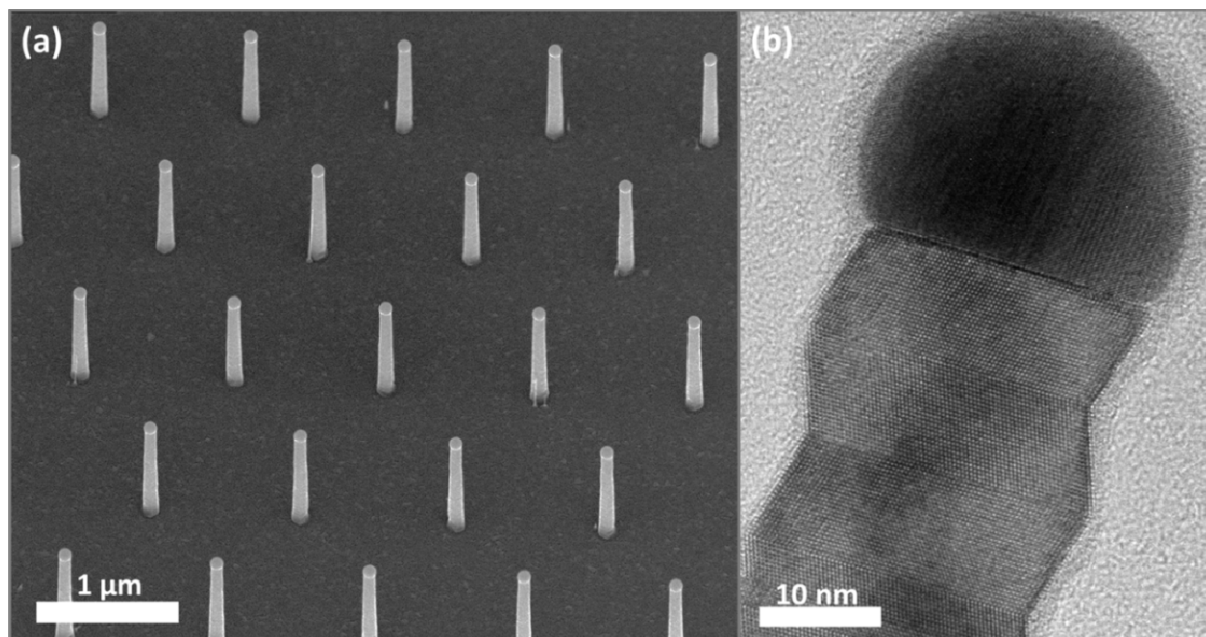
Figur 8.3 **(a)** Svepelektronmikroskopbild av nanotrådar. **(b)** Transmissionselektronmikroskopbild av en nanotråd. Notera guldpartikeln på toppen.

För att tillverka nanotrådar med perfekt struktur använder man sig av epitaxiell "växt", vilket innebär att man på ett kontrollerat sätt bygger upp nanotråden atomlager för atomlager, ofta från ett substrat (tex en kiselskiva). Det absolut vanligaste sättet att starta den epitaxiella växten är med hjälp av en nanopartikel som agerar som ett frö. För att få igång växten tillsätter man materialet man vill växa sin nanotråd av i gasform och ökar temperaturen. Nanotråden växer då på den plats där nanopartikeln är placerad och nanotrådens diameter bestäms av diametern på nanopartikeln medan nanotrådens längd bestäms av hur länge man tillför sina gaser (Figur 8.4). Genom att byta ut gaserna till andra gaser kan man växa nanotrådar med olika kemisk komposition i en och samma tråd, så kallade heterostrukturerade nanotrådar.

Guld är det absolut vanligaste materialet hos nanopartiklar som används för epitaxiell växt av nanotrådar. I den här avhandlingen diskuteras varför guld fungerar bättre än andra material för nanotrådsväxt. Vidare undersöks hur olika tillverkningsprocesser och deponeringsmetoder för nanopartiklar av guld påverkar nanotrådsväxten. Slutligen visas det att man kan använda diametern hos nanopartikeln (diametern hos nanotråden) för att styra både kristallstrukturen hos nanotråden och förmågan att växa heterostrukturerade nanotrådar.
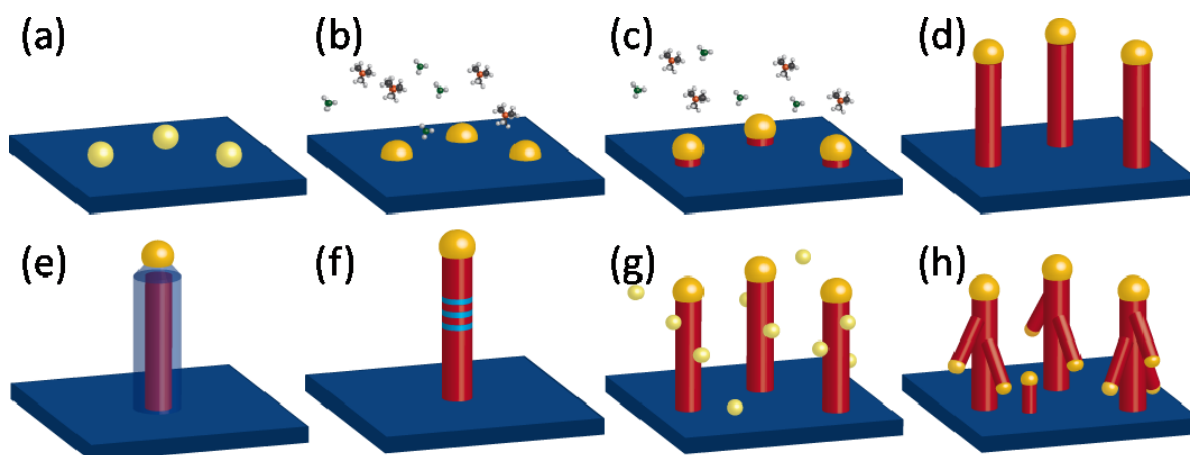
Figur 8.4 Schematisk bild som visar guldnanopartikel-assisterad nanotrådsväxt. **(a)** Nanopartiklarna deponeras/formas på substratet och **(b)** genom att värma upp substratet och tillföra växtmaterial (i gasform) bildas en legerad guld-växtmaterial partikel. **(c)** När en övermättnad av material nås i partikeln börjar växt av nanotråden ske under partikeln. **(d)** Nanotrådsväxten fortsätter under partikeln så länge man tillför växtmaterial. **(e)** Genom att ändra växtförutsättningar (t ex temperaturen) kan man växa radiella heterostrukturer och **(f)** genom att ändra växtmaterial kan man växa axiella heterostrukturer. **(g)** Om man deponerar nya nanopartiklar på de redan växta nanotrådarna och **(h)** upprepar växtproceduren kan man växa grenade nanotrådar för att tillverka nanotrådsnätverk.

De aerosoltillverkade nanopartiklarna i den här avhandlingen har också använts för forskning inom katalysområdet. En katalysator är ett material som påskyndar en viss kemisk reaktion utan att själv förbrukas. Katalysatorer används inte bara för att rena avgaser utan också i tillverkningen av över 80 % av alla kemikalier. I de flesta fall är katalysatorn i fast form och reaktanterna i gasform, vilket kallas heterogen katalys. En typisk katalysator är väldigt komplex i sin uppbyggnad och består vanligen av små katalytiskt aktiva metallpartiklar inneslutna i något isolerande oxidmaterial. På grund av komplexiteten hos katalysatorn är själva mekanismerna bakom de olika katalysreaktionerna till stora delar fortfarande okända. För att öka kunskapen om de katalytiska reaktionsvägarna har olika modellsystem utvecklats och studerats. Studierna har ofta utförts med metoder som kräver ultrahögt vacuum (UHV) tryck, medan en verklig katalysator vanligen arbetar under atmosfärstryck. Detta har lett till att man myntat begreppet material-tryck-gapet inom katalysforskningen och ett stort mål är att överbrygga det gapet genom att närma sig en situation som är så lik den verkliga situationen som möjligt när man utför sina studier.

Det typiska modellsystemet man har använt sig av för katalysforskning under många år är så kallade en-kristaller av det katalytiskt aktiva materialet. Det innebär att man har en kristall (atomer ordnade i ett visst upprepande mönster) med en stor och i stort sett slät yta, vilket är långt från den verkliga situationen där man inte har stora släta ytor, utan små nanopartiklar. I den här avhandlingen tas ett steg närmare en realistisk katalysatorsituation för att försöka överbrygga material-gapet genom att utföra katalysexperiment på små nanopartiklar deponerade på en oxidyta. Vidare har undersökningarna utförts under högre tryck än UHV för att även försöka överbrygga tryck-gapet.

De tillverkade nanopartiklarna har även använts för forskning inom området nanosäkerhet. Eftersom utvecklingen och användningen av nanopartiklar i olika produkter har gått väldigt fort, har inte forskningen vad gäller säkerhet riktigt hängt med i samma takt. Det finns klara regler för hur stora mängder (t ex reglerat i masskoncentration) av ett visst specifikt material som är tillåtet i exempelvis en viss produkt, men de reglerna kan vara oanvändbara när det gäller material på nanoskalan. Dels är nanostrukturer så små att det krävs oerhört många innan man kommer upp i en viss massa, dels kan ett material som är ofarligt på vår "familjära" storleksskala ha toxiska egenskaper när det förekommer på nanoskalan. Vidare är det okänt vilken egenskap hos nanomaterialen; antal, ytarea, massa, form, material, löslighet, ytkemi, mm, som spelar störst roll för möjliga toxiska egenskaper. Därför är det oklart om man ska sätta upp regler för exempelvis masskoncentration, antalskoncentration eller ytareakoncentration när det gäller reglering av nanomaterial.

För att kunna utföra relevanta studier inom nanotoxikologi krävs det dels att man har en deponeringssituation som är så lik den verkliga exponeringssituationen som möjligt, och dels att man vet exakt hur nanopartiklarna man deponerar ser ut. I den här avhandlingen visas hur gnistgeneratorn kan användas för att tillverka nanopartiklar som används direkt för inhalationsstudier på möss. Vidare visas att det är möjligt att tillverka och deponera välkarakteriserade partiklar av många olika material, för att deponera i proteinlösningar eller direkt på celler. Genom den här metoden kan en egenskap i taget ändras på ett kontrollerat sätt, medan alla andra hålls oförändrade, för att kunna förstå hur de olika egenskaperna hos partiklarna påverkar toxiciteten. Förhoppningsvis leder forskningen inom nanosäkerhet till att nanopartiklar kan tillverkas, hanteras och användas på ett säkert och ofarligt sätt så att vi alla kan dra nytta av nya användbara produkter baserade på nanopartiklar.

References

[1]   M. C. Roco: *Broader societal issues of nanotechnology.* J. Nanopart. Res., **2003**, 5, 181–189

[2]   G. Oberdorster, E. Oberdorster and J. Oberdorster: *Nanotoxicology: An emerging discipline evolving from studies of ultrafine particles.* Environ. Health Perspect., **2005**, 113, 823–839

[3]   V. Ramanathan, P. J. Crutzen, J. T. Kiehl and D. Rosenfeldt: *Aerosols, Climate, and the Hydrological Cycle.* Science, **2001**, 294, 2119–2124

[4]   P. H. M. Hoet, I. Brüske-Hohlfeld and O. V. Salata: *Nanoparticles – known and unknown health risks.* J. Nanobiotechn., **2004**, 2, 12

[5]   M. O. Andreae, C. D. Jones and P. M. Cox: *Strong present-day aerosol cooling implies a hot future.* Nature, **2005**, 435, 1187–1190

[6]   C. A. Pope, R. T. Burnett, M. J. Thun, E. E. Calle, D. Krewski, K. Ito and G. D. Thurston: *Lung cancer, cardiopulmonary mortality and long term exposure to fine particulate air pollution.* J. Am. Med. Assoc., **2002**, 287, 1132–1141

[7]   W. C. Hinds: *Aerosol Technology: Properties, Behaviour, and Measurements of Airborn Particles*, Wiley and Sons, New York, **1982**

[8]   F. E. Kruis, H. Fissan and A. Peled: *Synthesis of nanoparticles in the gas phase for electronic, optical and magnetic applications – a review.* J. Aerosol. Sci., **1998**, 29, 511–535

[9]   V. L. Colvin, M. C. Schlamp and A. P. Alivisatos: *Light-emitting-diodes made from cadmium selenide nanocrystals and a semiconducting polymer.* Nature, **1994**, 370, 354–357

[10]   F. A. Volkening, M. N. Naidoo, G. A. Candela, R. L. Holtz and V. Provenzano: *Characterization of nanocrystalline palladium for solid state gas sensor applications.* Nanostruct. Materials, **1995**, 5, 373–382

[11]   I. Aruna, F. E. Kruis, S. Kundu, M. Muhler, R. Theissmann and M. Spasova: *CO ppb sensors based on monodispersed SnO_x:Pd mixed nanoparticle layers: Insight into dual conductance response.* J. Appl. Phys., **2009**, 105, 064312

[12]   A. S. Barnard: *One-to-one comparison of sunscreen efficacy, aesthetics and potential nanotoxicity.* Nat. Nanotechnol., **2010**, 5, 271–274

[13]   B. Nowack and T. D. Bucheli: *Occurrence, behavior and effects of nanoparticles in the environment.* Environ. Pollut., **2007**, 150, 5–22

[14]   A. Kumar, P. K. Vemula, P. M. Ajayan and G. John: *Silver-nanoparticle-embedded antimicrobial paints based on vegetable oil.* Nat. Mater., **2008**, 7, 236–241

[15]   K. Tiedeae, A. B. A. Boxallae, S. P. Tearb, J. Lewisa, H. Davidc and Martin Hassellöv: *Detection and characterization of engineered nanoparticles in food and the environment.* Food Addit. Contam., **2008**, 25, 795–821

[16]   M. Ambrosi, L. Dei, R. Giorgi, C. Neto and P. Baglioni: *Colloidal particles of $Ca(OH)_2$: Properties and applications to restoration of frescoes.* Langmuir, **2001**, 17, 4251–4255

[17]   Q. Chaudhry, M. Scotter, J. Blackburn, B. Ross, A. Boxall, L. Castle, R. Aitken and R. Watkins: *Applications and implications of nanotechnologies for the food sector.* Food Addit. Contam., **2008**, 25, 241–258

[18]   O. V. Salata: *Applications of nanoparticles in biology and medicine.* J. Nanobiotechn., **2004**, 2, 1–6

[19]   M. A. Dobrovolskaia and S. E. McNeil: *Immunological properties of engineered nanomaterials.* Nat. Nanotechnol., **2007**, 2, 469–478

[20]   C. Helsper, W. Mölter, F. Löffler, C. Wadenpohl, S. Kaufmann and G. Wenninger: *Investigations of a new aerosol generator for the production of carbon aggregate particles.* Atmos. Environ., **1993**, 27A, 1271–1275

[21]   R. Reinmann and M. Akram: *Temporal investigations of a fast spark discharge in chemically inert gases.* J. Phys. D., **1997**, 30, 1125–1134

[22]   S. Schwyn, E. Garwin and A. Schmidt-Ott: *Aerosol generation by spark discharge.* J. Aerosol Sci., **1988**, 19, 639–642

[23]   N. S. Tabrizi, M. Ullmann, V. A. Vons, U. Lafont and A. Schmidt-Ott: *Generation of nanoparticles by spark discharge.* J. Nanopart. Res., **2009**, 11, 315–332

[24]   D. E. Evans, R. M. Harrison and J. G. Ayres: *The generation and characterization of elemental carbon aerosols for human challenge studies.* J. Aerosol Sci., **2003**, 34, 1023–1041

[25]   D. E. Evans, R. M. Harrison and J. G. Ayres: *The generation and characterization of metallic and mixed element aerosols for human challenge studies.* Aerosol Sci. Technol., **2003**, 37, 975–987

[26]   H.G. Scheibel and J. Porstendörfer: *Generation of monodisperse Ag- and NaCl-aerosols with particle diameters between 2 and 300 nm.* J. Aerosol Sci., **1983**, 14, 113–126

[27]   B. J. Ohlsson, M. T. Björk, M. H. Magnusson, K. Deppert, L. Samuelson and L. R. Wallenberg: *Size- shape- and position-controlled GaAs nano-whiskers.* App. Phys. Lett., **2001**, 79, 3335–3337

[28]   M. H. Magnusson, K. Deppert, J. –O. Malm, J. –O. Bovin and L. Samuelson: *Gold nanoparticles: Production, reshaping, and thermal charging.* J. Nanopart. Res., **1999**, 1, 243–251

[29]   A. Wiedensohler: *An approximation of the bipolar charge-distribution for particles in the sub-micron range.* J. Aerosol Sci., **1988**, 19, 387–389

[30]   E.O. Knutson and K.T. Whitby: *Aerosol classification by electron mobility: Apparatus, theory, and applications.* J. Aerosol Sci., **1975**, 6, 443–451

[31]   M. N. A. Karlsson, K. Deppert, L. S. Karlsson, M. H. Magnusson, J. – O. Malm and N. S. Srinivasan: *Compaction of agglomerates of aerosol nanoparticles: A compilation of experimental data.* J. Nanoparticle Res., **2005**, 7, 43–49

[32]   K. Deppert, F. Schmidt, T. Krinke, J. Dixkens and H. Fissan: *Electrostatic precipitator for homogeneous deposition of ultrafine particles to create quantum-dot structures.* J. Aerosol Sci., **1996**, 27, S151–S152

[33]   G. Schmid: *Large clusters and colloids. Metals in the embryonic state.* Chem. Rev., **1992**, 92, 1709–1727

[34]   M. C. Daniel and D. Astruc: *Gold nanoparticles: Assembly, supramolecular chemistry, quantum-sixe-related properties, and applications toward biology, catalysis and nanotechnology.* Chem. Rev., **2004**, 104, 293–346

[35]   A. I. Hochbaum, R. Fan, R. R. He and P. D. Yang: *Controlled growth of Si nanowire arrays for device integration.* Nano Lett., **2005**, 5, 457–460

[36]   P. H. M. Böttger, Z. Bi, D. Adolph, K. A. Dick, L. S. Karlsson, M. N. A. Karlsson, B. A. Wacaser and K. Deppert: *Electrospraying of colloidal nanoparticles for seeding of nanostructure growth.* Nanotechn., **2007**, 18, 105304

[37]   S. Kodambaka, J. B. Hannon, R. M. Tromp and F. M. Ross: *Control of Si nanowire growth by oxygen.* Nano Lett., **2006**, 6, 1292–1296

[38]   M. C. Plante, J. Garrett, S. C. Ghosh, P. Kruse, H. Schriemer, T. Hall and R. R. LaPierre: *The formation of supported monodisperse Au nanoparticles by UV/ozone oxidation process.* Appl. Surf. Sci., **2006**, 253, 2348–2354

[39]   K. Hiruma, K. Haraguchi, Y. Masamitsu, Y. Madokoro and T. Katsuyama: *Nanometre-sized GaAs wires grown by organo-metallic vapour-phase epitaxy.* Nanotechn., **2006**, 17, S369–S375

[40]   D. B. Williams and C. B. Carter: *Transmission Electron Microscopy 2ⁿᵈ edition*, Springer, New York, **2009**

[41]   M. W. Larsson: *Transmission Electron Microscopy of Semiconductor Nanowires. PhD Thesis*, Lund, **2007**

[42]   Advanced Light Source at Lawrence Berkeley National Laboratory, *The Advanced Light Source*. Available at: www.als.lbl.gov/als/, **2011**

[43]   European Synchrotron Radiation Facility, ESRF. Available at www.esrf.eu, **2011**

[44]   MAX-Lab. Available at www.maxlab.lu.se, **2011**

[45]   D. F. Ogletree, H. Bluhm, G. Lebedev, C. S. Fadley, Z. Hussain and M. Salmerond: *A differentially pumped electrostatic lens system for photoemission studies in the millibar range.* Rev. Sci. Instrum., **2002**, 73, 3872–3877

[46]   H. Bluhm, M. Hävecker, A. Knop-Gericke, E. Kleimenov, R. Schlögl, D. Teschner, V. I. Bukhtiyarov, D. F. Ogletree and M. Salmeron: *Methanol oxidation on a copper catalyst investigated using in situ X-ray photoelectron spectroscopy.* J. Phys. Chem. B, **2004**, 108, 14340–14347

[47]   P. Bernard, K. Peters, J. Alvarez and S. Ferrer: *Ultrahigh vacuum/high pressure chamber for surface x-ray diffraction experiments.* Rev, Sci. Instrum., **1999**, 70, 1478–1480

[48]   R. van Rijn, M. D. Ackermann, O. Balmes, T. Dufrane, A. Geluk, H. Gonzalez, H. Isern, E. de Kuyper, L. Petit, V. A. Sole, D. Wermeille, R. Felici and J. W. M. Frenken: *Ultrahigh vacuum/high-pressure flow reactor for surface x-ray diffraction and grazing incidence small angle x-ray scattering studies close to conditions for industrial catalysis.* Rev. Sci. Instrum., **2010**, 81, 014101

[49]   G. Attard and C. Barnes: *Surfaces*, Oxford University Press, New York, **1998**

[50]   R. Westerström: *Compound formation in model catalyst, PhD Thesis*, Lund, **2009**

[51]   D. Briggs and M. P. Seah: *Practical surface analysis: By auger and x-ray photoelectron spectroscopy*, Wiley, Chichester, **1983**

[52]   K. Ehara, C. Hagwood and K. J. Coakley: *Novel method to classify aerosol particles according to their mass-to-charge ratio – Aerosol particle mass analyzer.* J. Aerosol Sci., **1996**, 27, 217–234

[53]   J. K. Agarwal and J. S. Gilmore: *Continuous flow single particle counting condensation nucleus counter.* J. Aerosol Sci., **1980**, 11, 343–357

[54]   X. F. Duan, Y. Huang, Y. Cui, J. F. Wang and C. M. Lieber: *Indium phosphide nanowires as building blocks for nanoscale electronic and optoelectronic devices.* Nature, **2001**, 409, 66–69

[55]   J. M. Bao, M. A. Zimmler, F. Capasso, X. Wang and Z. F. Ren: *Broadband ZnO single-nanowire light-emitting diode.* Nano Lett., **2006**, 6, 1719–1722

[56]   E. D. Minot, F. Kelkensberg, M. van Kouwen, J. A. van Dam, L. P. Kouwenhoven, V. Zwiller, M. T. Borgström, O. Wunnicke, M. A. Verheijen and E. P. A. M. Bakkers: *Single quantum dot nanowire LEDs.* Nano Lett., **2007**, 7, 367–371

[57]   C. P. T. Svensson, T. Mårtensson, J. Trägårdh, C. Larsson, M. Rask, D. Hessman, L. Samuelson and J. Ohlsson: *Monolithic GaAs/InGaP nanowire light emitting diodes on silicon.* Nanotechn., **2008**, 19, 305201

[58]   S. D. Hersee, M. Fairchild, A. K. Rishinaramangalam, M. S. Ferdous, L. Zhang, P. M. Varangis, B. S. Swartzentruber and A. A. Talin: *GaN nanowire light emitting diodes based on templated and scalable nanowire growth process.* Electr. Lett., **2009**, 45, 75–76

[59]   Y. Li, F. Qian, J. Xiang and C. M. Lieber: *Nanowire electronic and optoelectronic devices.* Mater. Today, **2006**, 9, 18–27

[60]   J. Goldberger, A. I. Hochbaum, R. Fan and P. Yang: *Silicon vertically integrated nanowire field effect transistors.* Nano Lett., **2006**, 6, 973–977

[61]   S. A. Dayeh, D. P. R. Aplin, X. Zhou, P. K. L. Yu, E. T. Yu and D. Wang: *High electron mobility InAs nanowire field-effect transistors.* Small, **2007**, 3, 326–322

[62]   L. –E. Wernersson, E. Lind, L. Samuelson, T. Löwgren and J. Ohlsson: *Nanowire field-effect transistor.* Jpn. J. Appl. Phys., **2007**, 46, 2629–2631

[63]   H. A. Nilsson, P. Caroff, C. Thelander, E. Lind, O. Karlström and L. –E. Wernersson: *Temperature dependent properties of InSb and InAs nanowire field-effect transistors.* Appl. Phys. Lett., **2010**, 96, 153505

[64]   M. Law, L. E. Greene, R. Johnson, R. Saykally and P. Yang: *Nanowire dye-sensitized solar cells.* Nature Mater., **2005**, 4, 455–459

[65]   B. Tian, X. Zheng, T. J. Kempa, Y. Fang, N. Yu, G. Yu, J. Huang and C. M. Lieber: *Coaxial silicon nanowires as solar cells and nanoelectronic power sources.* Nature, **2007**, 449, 885–890

[66]   H. Goto, K. Nosaki, K. Tomioka, S. Hara, K. Hiruma, J. Motohisa and T. Fukui: *Growth of core-shell InP nanowires for photovoltaic application by selective-area metal organic vapor phase epitaxy.* Appl. Phys. Express, **2009**, 2, 035004

[67]   S. Chu, D. D. Li, P. C. Chang and J. G Lu: *Flexible dye-sensitized solar cell based on vertical ZnO nanowire arrays.* Nanoscale Res. Lett., **2011**, 6, 38

[68]   F. Zhou, J. H. Seol, A. L. Moore, L. Shi, Q. L. Ye and R. Scheffler: *One-dimensional electron transport and thermopower in an individual InSb nanowire.* J. Phys.: Condens. Matter., **2006**, 18, 9651–9657

[69]   A. I. Bouka, Y. Bunimovich, J. Tahir-Khel, J. K. Yu, W. A. Goddard III and J. R. Heath: *Silicon nanowires as efficient thermoelectric materials.* Nature, **2008**, 451, 168–171

[70]   Y. Cui, Q. Wei, H. Park and C. M. Lieber: *Nanowire nanosensors for highly sensitive and selective detection of biological and chemical species.* Science, **2001**, 293, 1289–1292

[71]   F. Patolsky, G. F. Zheng and C. M. Lieber: *Nanowire-based biosensors.* Anal. Chem., **2006**, 78, 4260–4269

[72]   K. I. Chen, B. R. Li and Y. T. Chen: *Silicon nanowire field-effect transistor-based biosensors for biomedical diagnosis and cellular recording investigation.* Nano Today, **2011**, 6, 131–154

[73]   W. Hällström, C. N. Prinz, D. Suyatin, L. Samuelson, L. Montelius and M. Kanje: *Rectifying and sorting of regenerating axons by free-standing nanowire patterns: A highway for nerve fibers.* Langmuir, **2009**, 25, 4343–4346

[74]   C.N.R. Rao, F.L. Deepak, G. Gundiah and A. Govindaraj: *Inorganic nanowires.* Prog. Solid State Ch., **2003**, 31, 5–147

[75]   K. A. Dick: *A review of nanowire growth promoted by alloys and non-alloying elements with emphasis on Au-assisted III-V nanowires.* Prog. Cryst. Growth Char. Mater., **2008**, 54, 138–173

[76]   J. Noborisaka, J. Motohisa and T. Fukui: *Catalyst-free growth of GaAs nanowires by selective-area metalorganic vapor-phase epitaxy.* Appl. Phys. Lett., **2005**, 86, 213102

[77]   B. Mandl, J. Stangl, T. Mårtensson, A. Mikkelsen, J. Eriksson, L. S. Karlsson, G. Bauer, L. Samuelson and W. Seifert: *Au-free epitaxial growth of InAs nanowires.* Nano Lett., **2006**, 6, 1817–1821

[78]   C. Colombo, D. Spirkoska, M. Frimmer, G. Abstreiter and A. Fontcuberta i Morral: *Ga-assisted catalyst-free growth mechanism of GaAs nanowires by molecular beam epitaxy.* Phys. Rev. B, **2008**, 77, 155326

[79]   B. Mandl, J. Stangl, E. Hilner, A. A. Zakharov, K. Hillerich, A. W. Dey, L. Samuelson, G. Bauer, K. Deppert and A. Mikkelsen: *Growth mechanism of self-catalyzed group III-V nanowires.* Nano Lett., **2010**, 10, 4443–4449

[80]   P. Nguyen, H. T. Ng and M. Meyyappan: *Catalyst metal selection for synthesis of inorganic nanowires.* Adv. Mater., **2005**, 17, 1773–1777

[81]   H. Y. Tuan, D. C. Lee and B. A. Korgel: *Nanocrystal-mediated crystallization of silicon and germanium nanowires in organic solvents: The role of catalysis and solid-phase seeding.* Angew. Chem. Int. Ed., **2006**, 45, 5184–5187

[82]   Y. W. Wang, V. Schmidt, S. Senz and U. Gösele: *Epitaxial growth of silicon nanowires using an aluminium catalyst.* Nature Nanotech., **2006**, 1, 186–189

[83]   I. Regolin, V. Khorenko, W. Prost, F. J. Tegude, D. Sudfeld, J. Kästner, G. Dumpich, K. Hitzbleck and H. Wiggers: *GaAs whiskers grown by metal-organic vapor-phase epitaxy using Fe nanoparticles.* J. Appl. Phys., **2007**, 101, 054318

[84]   G B Stringfellow: *Organometallic vapour-phase epitaxy: theory and practice*, Academic Press, London, **1989**

[85]   N. Sköld, L. S. Karlsson, M. W. Larsson, M. –E. Pistol, W. Seifert, J. Trägårdh and L. Samuelson: *Growth and optical properties of strained GaAs-Ga$_x$In$_{1-x}$P core-shell nanowires.* Nano Lett., **2005**, 5, 1943–1947

[86]   M. T. Björk, B. J. Ohlsson, T. Sass, A. I. Persson, C. Thelander, M. H. Magnusson, K. Deppert, L. R. Wallenberg and L. Samuelson: *One-dimensional heterostructures in semiconductor nanowhiskers.* App. Phys. Lett., **2002**, 80, 1058–1060

[87]   K. A. Dick, K. Deppert, M. W. Larsson, T. Mårtensson, W. Seifert, L. R. Wallenberg and L. Samuelson: *Synthesis of branched 'nanotrees' by controlled seeding of multiple branching events.* Nature Mater., **2004**, 3, 380–384

[88]   R. S. Wagner and W. C. Ellis: *Vapor-liquid-solid mechanism of single crystal growth.* Appl. Phys. Lett., **1964**, 4, 89–90

[89]   A. I. Persson, M. W. Larsson, S. Stenström, B. J. Ohlsson, L. Samuelson and L. R. Wallenberg: *Solid-phase diffusion mechanism for GaAs nanowire growth.* Nature Mater., **2004**, 3, 677–681

[90]   M. D. Stiles and D. R. Hamann: *Electron transmission through silicon stacking-faults.* Phys. Rev. B, **1990**, 41, 5280–5282

[91]   J. M. Bao, D. C. Bell, F. Capasso, J. B. Wagner, T. Mårtensson, J. Trägårdh and L. Samuelson: *Optical properties of rotationally twinned InP nanowire heterostructures.* Nano Lett., **2008**, 8, 836–841

[92]   M. Koguchi, H. Kakibayashi, M. Yazawa, K. Hiruma and T. Katsuyama: *Crystal-structure change of GaAs and InAs whiskers from zincblende to wurtzite type.* Jpn J. Appl. Phys., **1992**, 31, 2061–2065

[93]   H. J. Joyce, Q. Gao, H. H. Tan, C. Jagadish, Y. Kim, X. Zhang, Y. Guo and J. Zou: *Twin-free uniform epitaxial GaAs nanowires grown by a two-temperature process.* Nano Lett., **2007**, 7, 921–926

[94]   R. E. Algra, M. A. Verheijen, M. T. Borgström, L. –F. Feiner, G. Immink, W. J. P. van Enckevort, E. Vlieg and E. P. A. M. Bakkers: *Twinning superlattices in indium phosphide nanowires.* Nature, **2008**, 456, 369–372

[95]   B. A. Wacaser, K. Deppert, L. S. Karlsson, L. Samuelson and W. Seifert: *Growth and characterization of defect free GaAs nanowires.* J. Cryst. Growth, **2006**, 287, 504–508

[96]   H. Q. Wu, H. –Y. Cha, M. Chandrashekhar, M. G. Spencer and G. Koley: *High-yield GaN nanowire synthesis and field-effect transistor fabrication.* J. Electron. Mater., **2006**, 35, 670–674

[97]   P. Caroff, J. B. Wagner, K. A. Dick, H. A. Nilsson, M. Jeppsson, K. Deppert, L. Samuelsson, L. R. Wallenberg and L. –E. Wernersson: *High-quality InAs/InSb nanowire heterostructures grown by metal-organic vapor-phase epitaxy.* Small, **2008**, 4, 878–882

[98]   M. Jeppsson, K. A. Dick, J. B. Wagner, P. Caroff, K. Deppert, L. Samuelson and L. –E. Wernersson: *GaAs/GaSb nanowire heterostructures grown by MOVPE.* J. Cryst. Growth, **2008**, 310, 4115–4121

[99]   T. Akiyama, K. Sano, K. Nakamura and T. Ito: *An empirical potential approach to wurtzite-zinc-blende polytypism in group III-V semiconductor nanowires.* J. Appl. Phys., **2006**, 45, L275–L278

[100]   V. G. Dubrovskii and N. V. Sibirev: *Effect of nucleation on the crystalline structure of nanowhiskers.* Tech. Phys. Lett., **2009**, 35, 380–383

[101]   T. L. Tran, F. Hatami, W. T. Maselink, V. P. Kunets and G. J. Salamo: *Comparison of MBE Growth of InSb on Si (001) and GaAs (001).* J. Electron. Mater., **2008**, 37, 1799–1805

[102]   J. I. Chyi, D. Biswas, S. V. Iyer, N. S. Kumar, H. Morkoc, R. Bean, K. Zanio, H. Y. Lee and H. Chen: *Molecular-beam epitaxial-growth and characterization of InSb on Si.* Appl. Phys. Lett.,**1989**, 54, 1016–1018

[103]   M. Mori, K. Murata, N. Fujimoto, C. Tatsuyama, and T. Tambo: *Effect of AlSb buffer layer thickness on heteroepitaxial growth of InSb films on a Si(001) substrate.* Thin Solid Films, **2007**, 515, 7861–7865

[104]   Y. G. Guo, J. Zou, M. Paladugu, H. Wang, Q. Gao, H. H. Tan, and C. Jagadish: *Structural characteristics of GaSb/GaAs nanowire heterostructures grown by metal-organic chemical vapor deposition.* Appl. Phys. Lett., **2006**, 89, 231917

[105]   M. W. Larsson, J. B. Wagner, M. Wallin, P. Håkansson, L. E. Fröberg, L. Samuelson and L. R. Wallenberg: *Strain mapping in free-standing heterostructured wurtzite InAs/InP nanowires.* Nanotechn., **2007**, 18, 015504

[106]   K. Hiruma, H. Murakoshi, M. Yazawa and T. Katsuyama: *Self-organized growth of GaAs/InAs heterostructure nanocylinders by organometallic vapor phase epitaxy.* J. Cryst. Growth, **1996**, 163, 226–231

[107]   K. A. Dick, S. Kodambaka, M. C. Reuter, K. Deppert, L. Samuelson, W. Seifert, L. R. Wallenberg and F. M. Ross: *The morphology of axial and branched nanowire heterostructures.* Nano Lett., **2007**, 7, 1817–1822

[108]   M. Paladugu, J. Zou, Y. N. Guo, G. J. Auchterlonie, H. J. Joyce, Q. Gao, H. H. Tan, C. Jagadish and Y. Kim: *Novel growth phenomena observed in axial InAs/GaAs nanowire heterostructures.* Small, **2007**, 3, 1873–1877

[109]   H. J. Joyce, J. Wong-Leung, Q. Gao, H. H. Tan and C. Jagadish: *Phase perfection in zinc blende and wurtzite III-V nanowires using basic growth parameters.* Nano Lett., **2010**, 10, 908–915

[110]   B. A. Wacaser, K. A. Dick, J. Johansson, M. T. Borgström, K. Deppert and L. Samuelson: *Preferential interface nucleation: An expansion of the VLS growth mechanism for nanowires.* Adv. Mater., **2009**, 21, 153–165

[111]   V. A. Nebol'sin and A. A. Shchetinin: *Role of surface energy in the vapor-liquid-solid growth of silicon.* Inorg. Mater., **2003**, 39, 899–903

[112]   J. Arbiol, B. Kalache, P. Roca i Cabarrocas, J. R. Morante and A. Fontcuberta i Morral: *Influence of Cu as a catalyst on the properties of silicon nanowires synthesized by the vapour-solid-solid mechanism.* Nanotechn., **2007**, 18, 305606

[113]   J. B. Jackson, D. Kapoor, S. G. Jun and M. S. Miller: *Integrated silicon nanowire diodes and the effects of gold doping from the growth catalyst.* J. Appl. Phys., **2007**, 102, 054310

[114]   K. A. Dick, K. Deppert, T. Mårtensson, B. Mandl, L. Samuelson and W. Seifert: *Failure of the vapor-liquid-solid mechanism in Au-assisted MOVPE growth of InAs nanowires.* Nano Lett., **2005**, 5, 761–764

[115]   F. Martelli, S. Rubini, M. Piccin, G. Bais, F. Jabeen, S. De Franceschi, V. Grillo, E. Carlino, F. D'Acapito, F. Boscherini, S. Cabrini, M. Lazzarino, L. Businaro, F. Romanato and A. Franciosi: *Manganese-induced growth of GaAs nanowires.* Nano Lett., **2006**, 6, 2130–2134

[116]   M. Borgström, K. Deppert, L. Samuelson and W. Seifert: *Size- and shape-controlled GaAs nano-whiskers grown by MOVPE: A growth study.* J. Cryst. Growth, **2004**, 260, 18–22

[117]   P. Paiano, P. Prete, N. Lovergine and A. M. Mancini: *Size and shape control of GaAs nanowires grown by metalorganic vapor phase epitaxy using tertiarybutylarsine.* J. Appl. Phys., **2006**, 100, 094305

[118]   A. I. Persson, L. E. Fröberg, S. Jeppesen, M. T. Björk and L. Samuelson: *Surface diffusion effects on growth of nanowires by chemical beam epitaxy.* J. Appl. Phys., **2007**, 101, 034313

[119]   M. A. Verheijen, G. Immink, T. Desmet, M. T. Borgström and E. P. A. M. Bakkers: *Growth kinetics of heterostructured GaP-GaAs nanowires.* J. Am. Chem. Soc., **2006**, 128, 1353–1359

[120]   S. Kodambaka, J. Tersoff, M. C. Reuter and F. M. Ross: *Diameter-independent kinetics in the vapor-liquid-solid growth of Si nanowires.* Phys. Rev. Lett., **2006**, 96, 096105

[121]   B. Hvolbæk, T. V. W. Janssens, B. S. Clausen, H. Falsig, C. H. Christensen and J. K. Nørskov: *Catalytic activity of Au nanoparticles.* Nano Today, **2007**, 2, 14–18

[122]   A. I. Hochbaum, R. Fan, R. R. He and P. D. Yang: *Controlled growth of Si nanowire arrays for device integration.* Nano Lett., **2005**, 5, 457–460

[123]   T. Mårtensson, M. Borgström, W. Seifert, B. J. Ohlsson and L. Samuelson: *Fabrication of individually seeded nanowire arrays by vapour-liquid-solid growth.* Nanotechn., **2003**, 14, 1255–1258

[124]   K. Hiruma, K. Haraguchi, Y. Masamitsu, Y. Madokoro and T. Katsuyama: *Nanometre-sized GaAs wires grown by organo-metallic vapour-phase epitaxy.* Nanotechn., **2006**, 17, S369–S375

[125]   A. M. Morales and C. M. Lieber: *A laser ablation method for the synthesis of crystalline semiconductor nanowires.* Science, **1998**, 279, 208–211

[126]   T. Mårtensson, P. Carlberg, M. Borgström, L. Montelius, W. Seifert and L. Samuelson: *Nanowire arrays defined by nanoimprint lithography.* Nano Lett., **2004**, 4, 699–702

[127]   J. Johansson, L. S. Karlsson, K. A. Dick, J. Bolinsson, B. A. Wacaser, K. Deppert and L. Samuelson: *Effects of supersaturation on the crystal structure of gold seeded III-V nanowires.* Crys. Growth Des., **2009**, 9, 766–773

[128]   G. A. Somorjai: *Chemistry in two dimensions: Surfaces*, Cornell University Press, Ithaca, **1981**

[129]   J. Libuda and H. –J. Freund: *Molecular beam experiments on model catalysts.* Surf. Sci. Rep., **2005**, 57, 157–298

[130]   T. Schalow, B. Brandt, M. Laurin, S. Schauermann, S. Guilmond, H. Kuhlenbeck, J. Libuda and H. –J. Freund: *Formation of interface and surface oxides on supported Pd nanoparticles.* Surf. Sci., **2006**, 600, 2528–2542

[131]   F. Tao, M. E. Grass, Y. W. Zhang, D. R. Butcher, J. R. Renzas, Z. Liu, J. Y. Chung, B. S. Mun, M. Salmeron and G. A. Somorjai: *Reaction-driven restructuring of Rh-Pd and Pt-Pd core-shell nanoparticles.* Science, **2008**, 322, 932–934

[132]   S. Bonanni, K. Aït-Mansour, H. Brune and W. Harbich: *Overcoming the strong metal-support interaction state: CO oxidation on TiO$_2$(110)-supported Pt nanoclusters.* ACS Catalysis, **2011**, 1, 385–389

[133]   S. Bonanni, K. Aït-Mansour, M. Hugentobler, H. Brune and W. Harbich: *An experimental setup combining a highly sensitive detector for reaction products with a mass-selected cluster source and a low-temperature STM for advanced nanocatalysis measurements.* Eur. Phys. J. D, **2011**, 63, 241–249

[134]   C. Roth, G. A. Ferron, E. Karg, B. Lentner, G. Schumann, S. Takenaka and J. Heyder: *Generation of ultrafine particles by spark discharging.* Aerosol Sci. Technol., **2004**, 38, 228–235

[135]   E. Lundgren, A. Mikkelsen, J. N. Andersen, G. Kresse, M. Schmid and P. Varga: *Surface oxides on close-packed surfaces of late transition metals.* J. Phys. Condens. Matter, **2006**, 18, R481–R499

[136]   H. Over, Y. D. Kim, A. P. Seitsonen, S. Wendt, E. Lundgren, M. Schmid, P. Varga, A. Morgante and G. Ertl: *Atomic-scale structure and catalytic reactivity of the $RuO_2(110)$ surface.* Science, **2000**, 287, 1474–1476

[137]   B. L. M. Hendriksen and J. W. M. Frenken: *CO oxidation on Pt(110): Scanning tunneling microscopy inside a high-pressure flow reactor.* Phys. Rev. Lett., **2002**, 89, 046101

[138]   P. –A. Carlsson, V. P. Zhdanov and M. Skoglundh: *Self-sustained kinetic oscillations in CO oxidation over silica-supported Pt.* Phys. Chem. Chem. Phys., **2006**, 8, 2703–2706

[139]   R. Westerström, J. G. Wang, M. D. Ackermann, J. Gustafson, A. Resta, A. Mikkelsen, J. N. Andersen, E. Lundgren, O. Balmes, X. Torrelles, J. W. M. Frenken and B. Hammer: *Structure and reactivity of a model catalyst alloy under realistic conditions.* J. Phys. Condens. Mat., **2008**, 20, 184018

[140]   R. van Rijn, O. Balmes, R. Felici, J. Gustafsson, D. Wermeille, R. Westerström, E. Lundgren and J. W. M. Frenken: *Comment on "CO Oxidation on Pt-Group Metals from Ultrahigh Vacuum to Near Atmospheric Pressures. 2. Palladium and Platinum".* J. Phys. Chem. C, **2010**, 114, 6875 – 6876

[141]   J. Rogal, K. Reuter and M. Scheffler: *First-principles statistical mechanics study of the stability of a subnanometer thin surface oxide in reactive environments: CO oxidation at Pd(100).* Phys. Rev. Lett., **2007**, 98, 046101

[142]   G. Rupprechter and C. Weilach: *Mind the gap! Spectroscopy of catalytically active phases.* Nano Today, **2007**, 2, 20–29

[143]   M. S. Chen, Y. Cai, Z. Yan, K. K. Gath, S. Axnanda and D. W. Goodman: *Highly active surfaces for CO oxidation on Rh, Pd, and Pt.* Surf. Sci., **2007**, 601, 5326–5331

[144]   A. D. Maynard and E. D. Kuempel: *Airborne nanostructured particles and occupational health.* J. Nanopart. Res., **2005**, 7, 587–614

[145]   S. Pal, Y. K. Tak and J. M. Song: *Does the antibacterial activity of silver nanoparticles depend on the shape of the nanoparticle? A study of the gram-negative bacterium escherichia coli.* Appl. Environ. Microb., **2006**, 73, 1712–1720

[146]   W. Yang, J. I. Peters and R. O. Williams III: *Inhaled nanoparticles—a current review.* Int. J. Pharmaceut., **2008**, 356, 239–247

[147]   A. Tippe, U. Heinzmann and C. Roth: *Deposition of fine and ultrafine aerosol particles during exposure at the air/cell interface.* J. Aerosol Sci., **2002**, 33, 207–218

[148]   F. Blank, B. M. Rothen-Rutishauser, S. Schurch and P. Gehr: *An optimized in vitro model of the respiratory tract wall to study particle cell interactions.* J. Aerosol Med., **2006**, 19, 392–405

[149]   A. Gaschen, D. Lang, M. Kalberer, M. Savi, T. Geiser, A. Gazdhar, C. M. Lehr, M. Bur, J. Dommen, U. Baltensperger and M. Geiser: *Cellular responses after exposure of lung cell cultures to secondary organic aerosol particles.* Environ. Sci. Technol., **2010**, 44, 1424–1430

[150]   Z. X. Ji, X. Jin, S. George, T. A. Xia, H. A. Meng, X. A. Wang, E. Suarez, H. Y. Zhang, E. M. V. Hoek, H. Godwin, A. E. Nel and J. I. Zink: *Dispersion and stability optimization of TiO₂ nanoparticles in cell culture media.* Environ. Sci. Technol., **2010**, 44, 7309–7314

[151]   M. Savi, M. Kalberer, D. Lang, M. Ryser, M. Fierz, A. Gaschen, J. Ricka and M. Geiser: *A novel exposure system for the efficient and controlled deposition of aerosol particles onto cell cultures.* Environ. Sci. Technol., **2008**, 42, 5667–5674

[152]   R. N. Grass, L. K. Limbach, E. K. Athanassiou and W. J. Stark: *Exposure of aerosols and nanoparticle dispersions to in vitro cell cultures: A review on the dose relevance of size, mass, surface and concentration.* J. Aerosol. Sci., **2010**, 41, 1123–1142

[153]   U. Heinrich, R. Fuhst, S. Rittinghausen, O. Creutzenberg, B. Bellmann, W. Koch and K. Levsen: *Chronic inhalation exposure of wistar rats and two different strains of mice to diesel engine exhaust, carbon black, and titanium dioxide.* Inhal Toxicol., **2005**, 7, 533–556

[154]   P. J. Borm, R. P. Schins and C. Albrecht: *Inhaled particles and lung cancer, part B: Paradigms and risk assessment.* Int. J. Cancer, **2004**, 110, 3–14

[155]   D. Dankovic, E. Kuempel and M. Wheeler: *An approach to risk assessment for TiO₂.* Inhal. Toxicol., **2007**, 19, 205–212

[156]   J. P. Fryzek, B. Chadda, D. Marano, K. White, S. Schweitzer, J. K. McLaughlin and W. J. Blot: *A cohort mortality study among titanium dioxide manufacturing workers in the United States.* J. Occup. Environ. Med., **2003**, 45, 400–409

[157]   P. Boffetta, A. Soutar, J. W. Cherrie, F. Granath, A. Andersen, A. Anttila, M. Blettner, V. Gaborieau, S. J. Klug, S. Langard, D. Luce, F. Merletti, B. Miller, D. Mirabelli, E. Pukkala, H. O. Adami and E. Weiderpass: *Mortality among workers employed in the titanium dioxide production industry in Europe.* Cancer Causes Control, **2004**, 15, 697–706

[158] J. Lekki, Z. Stachura, W. Dabros, J. Stachura, F. Menzel, T. Reinert, T. Butz, J. Pallon, E. Gontier, M. D. Ynsa, P. Moretto, Z. Kertesz, Z. Szikszai and A. Z. Kiss: *On the follicular pathway of percutaneous uptake of nanoparticles: ion microscopy and autoradiography studies.* Nucl. Instrum. Methods Phys. Res. B, **2007**, 260, 174–177

[159] L. Ma-Hock, A. O. Gamer, R. Landsiedel, E. Leibold, T. Frechen, B. Sens, M. Linsenbuehler and B. van Ravenzwaay: *Generation and characterization of test atmospheres with nanomaterials.* Inhal. Toxicol., **2007**, 19, 833–848

[160] A. G. Konstandopoulos and M. Kostoglou: *Reciprocating flow regeneration of soot filters.* Combust. Flame, **2000**, 121, 488–500

[161] D. S. Su, J. O. Müller, R. E. Jentoft, D. Rothe, E. Jacob and R. Schlögl: *Fullerene-like soot from Euro IV diesel engine: consequences for catalytic automotive pollution control.* Top. Catal., **2004**, 30, 241–245

[162] L. Rantanen, R. Linnaila, P. Aakko and T. Harju: *NExBTL-biodiesel fuel of the second generation.* SAE technical paper series 2005-01-3771, **2005**

[163] M. Kuronen, S. Mikkonen, P. T. Aakko and T. Murtonen: *Hydrotreated vegetable oil as a fuel for heavy duty diesel engines.* SAE technical paper series 2007-01-4031, **2007**

[164] H. Aatola, M. Larmi, T. Sarjovaara and S. Mikkonen: *Hydrotreated vegetable oil (HVO) as a renewable diesel fuel: trade-off between NOx, particulate emission, and fuel consumption of a heavy duty engine.* SAE technical paper series 2008-01-2500, **2009**

[165] J. O. Müller, D. S. Su, R. E. Jentoft, J. Kröhnert, F. C. Jentoft and R. Schlögl: *Morphology controlled reactivity of carbonaceous materials towards oxidation.* Catal. Today, **2005**, 102, 259–65

[166] G. Oberdorster, V. Stone and K. Donaldson: *Toxicology of nanoparticles: A historical perspective.* Nanotoxicology, **2007**, 1, 2–25

[167]   S. Brunauer, P. H. Emmet and E. Teller: *Adsorption of gases in multimolecular layers.* J. Am. Chem. Soc., **1938**, 60, 309–319

[168]   A. A. Lall, W. Rong, L. Mädler and S. K. Friedlander: *Nanoparticle aggregate volume determination by electrical mobility analysis: Test of idealized aggregate theory using particle mass analyzer measurements.* J. Aerosol Sci., **2008**, 39, 403–417

[169]   J. Rissler, J. Löndahl, A. Bengtsson, C. Boman, J. Pagels, E. Swietlicki, A. Blomberg and T. Sandström: *Experimental determination of the respiratory tract deposition of diesel combustion particles.* Manuscript intentded for submission to Part. Fibre Tox., **2011**

[170]   K. Donaldson, P. J. A. Borm, G. Oberdörster, K. E. Pinkerton, V. Stone and C. L. Tran: *Concordance between in vitro and in vivo dosimetry in the proinflammatory effects of low toxicity low soluble particles: The key role of the proximal alveolar region.* Inhal. Toxicol., **2008**, 20, 53–62